

ADDITIVE MANUFACTURING OF HYDROGELS
FOR VASCULAR TISSUE ENGINEERING

ADDITIVE MANUFACTURING OF HYDROGELS FOR VASCULAR TISSUE ENGINEERING

By RANA ATTALLA, B.Eng.

A Thesis

Submitted to the School of Graduate Studies

in Partial Fulfilment of the Requirements for the Degree of

Doctor of Philosophy in Biomedical Engineering

McMaster University © Copyright by Rana Attalla, January 2018

McMaster University DOCTOR OF PHILOSOPHY (2018)
Hamilton, Ontario, Canada

TITLE: Additive Manufacturing of Hydrogels for Vascular
Tissue Engineering

AUTHOR: Rana Attalla
B. Eng (Ryerson University)

SUPERVISOR: Dr. P. Ravi Selvaganapathy

PAGES: xix, 143

LAY ABSTRACT

Additive manufacturing (AM) involves any three-dimensional (3D) fabrication technologies that is used to produce a solid model of a predetermined design. AM techniques have recently been used in tissue engineering applications for fabrication of 3D artificial tissues that resemble architectures and material properties similar to that of the native tissue. Utilizing AM for this purpose presents the advantage of increased control in feature patterning, which leads to the realization of more complex geometries. However, there still remains a lack of simple and effective methods to integrate vascular networks within these 3D artificially engineered scaffolds and tissue constructs. Without these vascular-like networks, the cells embedded within the constructs would quickly die due to a lack of nutrient delivery and waste transport. This remains one of the biggest challenges in true 3D tissue engineering. This thesis presents a number of fast, effective and low-cost AM biofabrication techniques to address this challenge.

ABSTRACT

One of the major technical challenges with creating 3D artificial tissue constructs is the lack of simple and effective methods to integrate vascular networks within them. Without these vascular-like networks, the cells embedded within the constructs quickly become necrotic.

This thesis details the use of a commercially available, low-cost, 3D printer modified with a microfluidic printhead in order to generate instantly perfusable vascular-like networks integrated within gel scaffolds seeded with cells. The printhead featured a coaxial nozzle that allowed the fabrication of hollow, gel tubes (500 μ m–2mm) that can be easily patterned to create single or multi-layered constructs. Media perfusion of the channels caused a significant increase in cell viability.

This microfluidic nozzle design was further modified to allow for multi-axial extrusion in order to 3D print and pattern bi- and tri-layered hollow channel structures. Most available methodologies lack the ability to create multi-layered concentric conduits inside natural extracellular matrices, which would more accurately replicate the hierarchal architecture of biological blood vessels. The nozzle used in this work allowed, for the first time, for these hierarchal structures to be embedded within layers of gels in a fast, simple and low cost manner. This scalable design allowed for versatility in material incorporation, thereby creating heterogeneous structures that contained distinct concentric layers of different cell types and biomaterials.

This thesis also demonstrates the use of non-extrusion based 3D biofabrication involving planar processing by means of hydrogel adhesion. There remains a lack of effective adhesives capable of composite layer fusion without affecting the integrity of patterned features. Here, silicon carbide was found for the first time to be an effective and cytocompatible adhesive to achieve strong bonding (0.39 \pm 0.03kPa) between hybrid hydrogel films. Multi-layered, heterogeneous constructs with embedded high-resolution microchannels (150 μ m-1mm) were fabricated in this way.

With the new 3D fabrication technology developed in this thesis, gel constructs with embedded arrays of hollow channels can be created and used as potential substitutes for blood vessel networks as well as in applications such as drug discovery models and biological studies.

ACKNOWLEDGEMENT

First and foremost, I would like to thank my supervisor and mentor Dr. Ravi Selvaganapathy for his endless support and guidance throughout the course of my Ph.D. His continuous encouragement and unceasing patience inspired confidence and helped me to persevere through the many challenges I faced during my work.

I would also like to thank my committee members, Dr. Raja Ghosh and Dr. Kim Jones, for their insightful feedback and vast technical knowledge that allowed me to broaden my research perspectives.

A big thank you to all the technicians and scientific staff that provided me with valuable help along the way. Mark Mackenzie, Joe Verhaeghe, Ron Lodewyks, Michael Lee, John Colenbrander, and Dan Wright in the Department of Mechanical Engineering. Marcia Reid and Marnie Timleck in the Electron Microscopy Facility. Marta Princz and Dawn White in the Biointerfaces Institute. I couldn't have done it without all of you.

I am very thankful to have been part of the CAMEF lab, a group of the most hard-working, friendly, and helpful people I have ever come to know. I am so grateful to have spent these past years with you, learning and laughing together. A special thank you to Leo, Reza, Jun, and Russel who were there the first day I started in the lab and continued to support me even after they had left the lab. To Nidhi, not only for your biology help, but also for your company and the fun we had in the lab. And most of all, to Celine – summer student turned colleague turned inseparable friend. Thank you for being there with me through it all. I couldn't have done it without you.

I was also lucky enough to meet some very special people outside my lab as well. My oldest friends, Maryam and Rabia, thank you for the unforgettable memories and the type of laughter that makes you stop breathing. And to my new friends, Jess, Nadine, and Sharita, thank you for the endless hilarious talks that made school enjoyable.

Above all, I'd like to thank my family. My dad who always motivated me to pursue this career path, and to my mom for all the sacrifices she made to support me emotionally, mentally and physically. To my grandparents who raised me, and my brothers who empowered me. To my extended in-law family - parents, brothers, sister, niece, nephew - who were constantly rooting for me throughout this entire journey. I love you all.

And finally, I want to thank my husband, Shariff. For supporting me when I did my transfer exam 3 days before our wedding and everyday since. For picking me up after the lows and celebrating with me during the highs. Without your unconditional support and love, none of this would have been possible. You are my best friend. Thank you.

CONTENTS

ABSTRACT.....	iv
ACKNOWLEDGEMENT.....	v
TABLE OF CONTENTS.....	vi
LIST OF FIGURES.....	x
NOMENCLATURE.....	xix
Chapter 1: INTRODUCTION.....	1
1. Introduction to 3D Tissue Engineering.....	1
1.1 Motivation for 3D tissue development.....	1
1.2 Conventional approaches for tissue engineering.....	1
1.2.1 Artificial scaffolding.....	2
1.2.2 Decellularization.....	2
1.2.3 Organ-on-a-chip systems.....	3
1.2.4 Limitations.....	3
1.3 Implementing additive manufacturing for 3D tissue engineering.....	4
2. Additive Manufacturing Techniques for 3D Tissue Engineering.....	6
2.1 Extrusion-based AM.....	7
2.1.1 Inkjet printing.....	7
2.1.2 Fused deposition modelling.....	7
2.1.3 3D Biplotting.....	8
2.1.4 Limitations of extrusion-based AM.....	10
2.2 Non-extrusion based AM.....	10
2.2.1 Selective laser sintering.....	10
2.2.2 Stereolithography.....	11
2.2.3 Planar processing.....	11
2.2.4 Limitations of non-extrusion based AM.....	13
2.3 Hybrid techniques.....	13
2.3.1 Multiple printheads.....	13
2.3.2 Sacrificial molding.....	13

2.3.3	Limitations of hybrid techniques.....	15
3.	Vascularization as a Major Challenge in 3D Tissue Engineering.....	15
3.1	Vessel formation and architecture.....	16
3.2	Conventional techniques.....	17
3.2.1	Artificial vascular grafting.....	17
3.2.2	Prevascularization.....	18
3.2.3	Limitations of conventional vascularization techniques.....	19
3.3	Unconventional 3D fabrication techniques.....	20
3.3.1	Extrusion-based techniques.....	20
3.3.2	Non-extrusion-based techniques.....	21
3.3.3	Hybrid techniques.....	23
3.3.4	Limitations of current AM used for vascularization.....	24
4.	Parameters Impacting AM Fabrication of Vascular-like Networks.....	25
4.1	Materials and cytocompatibility.....	26
4.2	Mechanical properties.....	27
4.3	Resolution.....	28
4.4	Speed.....	29
4.5	Cost.....	30
4.6	Summary.....	31
5.	Research Objectives and Aims.....	32
6.	Thesis Organization.....	32
7.	Contributions.....	35
8.	A Note to the Reader.....	37
	References.....	38
Chapter 2: FABRICATION AND CHARACTERIZATION OF GELS WITH INTEGRATED CHANNELS USING 3D PRINTING WITH MICROFLUIDIC NOZZLE FOR TISSUE ENGINEERING APPLICATIONS.....		46
1.	Introduction.....	47
2.	Methods and Materials.....	50
2.1	Printing apparatus and setup.....	50
2.2	Material extrusion.....	51

2.3 Cell culture and preparation.....	51
2.4 Cell-laden gel printing and maintenance.....	52
2.5 Cell-laden gel imaging.....	52
3. Results and Discussion.....	52
3.1 Material extrusion.....	52
3.2 Contiguous gel layer formation and perfusion.....	54
3.3 Characterization of flow rate and printhead speed.....	56
3.4 Printing with cell media-based solutions.....	60
3.5 Characterization of channel diameters.....	61
3.6 Demonstrations of dynamic channel size changes.....	63
3.7 Effect of material concentrations.....	64
3.8 Effect of change in directions during printing.....	65
3.9 Printing cell-laden structures.....	67
References.....	70
Chapter 3: 3D BIOPRINTING OF HETEROGENEOUS BI- AND TRI-LAYERED HOLLOW CHANNELS WITHIN GEL SCAFFOLDS USING SCALABLE MULTI- AXIAL EXTRUSION NOZZLE.....	74
1. Introduction.....	75
2. Methods and Materials.....	77
2.1 Extrusion device and setup.....	77
2.2 Extrusion mechanism.....	78
2.3 Cell culture.....	79
2.4 Cell-laden gel printing and imaging.....	80
3. Results and Discussion.....	81
3.1 Fabrication of 3D structures.....	81
3.2 Characterization of tri-axial printing.....	83
3.3 Effect of alginate and calcium concentration on printing.....	88
3.4 Effect of flow rate and print speed on printed channel dimension.....	90
3.5 Multi-cellular printing.....	92
3.6 Multi-material printing.....	95
References.....	98

Chapter 4: SILICON CARBIDE NANOPARTICLES AS AN EFFECTIVE BIOADHESIVE TO BOND COLLAGEN CONTAINING COMPOSITE GEL LAYERS FOR TISSUE ENGINEERING APPLICATIONS.....	101
1. Introduction.....	102
2. Methods and Materials.....	103
2.1 Preparation of gel solutions.....	103
2.2 Fabrication of microchannel structures.....	104
2.3 Mechanical testing.....	104
2.4 Cell culture and preparation.....	105
3. Results and Discussion.....	106
3.1 Hollow channel network fabrication and perfusion.....	106
3.2 Adhesion strength of various composite gels.....	109
3.3 Effect of adhesive concentration and time on bond strength.....	112
3.4 Cytotoxicity testing of adhesives.....	114
3.5 Adhesion of hydrogels to hard substrates.....	116
Supplementary Section.....	119
References.....	130
Chapter 5: CONCLUSIONS AND RECOMMENDATIONS.....	133
1. Conclusions.....	133
2. Research Contributions.....	135
2.1 Low-cost 3D bioprinting.....	135
2.2 Multi-biomaterial printing.....	136
2.3 Nanoparticle-based hydrogel adhesion.....	137
3. Recommendations for Future Work.....	138
3.1 “All-in-one” bioprinter for multi-biomaterial extrusion.....	138
3.2 Inducing angiogenesis.....	139
3.3 Drug discovery models.....	139
3.4 Alternative tissue engineering applications.....	140
APPENDIX.....	141

LIST OF FIGURES

FIG. 1.1: A) (i) Tissue engineered human bladder scaffold is seeded with cells. (ii) The bladder scaffold is anastomosed to native tissue and implanted. B) Decellularization of cadaveric rat heart. C) Silicon membranes patterned with uniformly spaced arrays of ultrathin slit pores used for blood filtration.4

FIG. 1.2: Schematic illustrating the various components required to fabricate an artificial 3D tissue or organ.6

FIG. 1.3: Schematic illustration describing the different types of 3D AM technologies available for bioapplications.6

FIG. 1.4: Extrusion-based AM techniques. A) (i)Schematic illustrating inkjet printing process, where precise bioink deposition is achieved using heat, piezoelectricity, or pressure. (ii) Piezoelectric inkjet printhead used to deposit cell-culture media dot containing 1-4 endothelial cells. B) (i)Schematic illustrating 3D bioplotting technique, where viscous hydrogel material is crosslinked upon deposition in order to create 3D constructs. (ii) Agar gel cube fabricated using 3D bioplotting.....9

FIG. 1.5: Non-extrusion based AM techniques. A) (i)Schematic illustrating SL process, where precise pattern definition is achieved using light induced polymerization. (ii)SL is used to fabricate 3D PEGDA/gelatin methacrylate structures with encapsulated fibroblast cells. B) (i)Schematic illustrating planar processing technique, where soft lithography micromolding followed by stacking of individually patterned polymer sheets is used to create 3D structures. (ii) Perfusable microchannel networks fabricated by casting and photocrosslinking of GelMA.....12

FIG. 1.6: Hybrid AM techniques. A) (i)Schematic illustration demonstrating the combined use of inkjet printing and electrospinning. (ii) Hybrid technique is used to create tissue engineered cartilage tissue by fabricating alternating layers of PCL and chondrocytes. B) (i)Schematic illustration showing sacrificial molding processes by mechanical removal of spacers or by liquefaction. (ii)Carbohydrate glass is 3D printed using FDM, followed by embedding into a hydrogel matrix and then dissolving with water in order to leave behind a hollow interconnected channel network.....14

FIG. 1.7: Anatomical depiction of the 3 layers that compose a vessel wall.17

FIG. 1.8: Schematic representation of the conventional method for fabrication of a tissue-engineered vascular graft. i) Example of a tissue engineered vascular grafts composed of fibrous co-polymers, fabricated using ring-opening polymerization.....19

FIG. 1.9: Some of the unconventional tissue engineering strategies currently being used to 3D construct vascular networks include A) 3D bioplotting, B) planar processing, and C) sacrificial molding.....22

FIG. 1.10: Schematic representation of the various factors affecting 3D fabrication techniques for bioapplications.25

FIG. 1.11: Table summarizing the various governing parameters that impact each specific AM technique and its suitability for vascular tissue engineering applications.31

FIG. 2.1: (A) Modified 3D RepRap printer. (B) Coaxial extrusion nozzle schematic: 700µm needle, 2mm L-shaped channel.....50

FIG. 2.2: (A-C) Hollow tubes extruded into CaCl₂ bath. Inner flow is constant at 10mL/min, while outer flow is (A) 20, (B) 10, and (C) 5mL/min respectively. Tubes extruded into a bath cannot be precisely positioned on a substrate. Extrusion into a bath solidifies the outer layer of the gel instantaneously and does not allow merging of adjacent tubes. Scale bars, 1mm.....53

FIG. 2.3: Formation of a continuous gel layer with embedded hollow channels due to extrusion onto a dry substrate. (A) Extrusion of hollow gel tube onto substrate. (B) Later spreading of the outer uncrosslinked alginate layer of the tube. (C) The delay in the gelation of the outer alginate layer causes fusion of adjacent tubes during patterned deposition. (D) The final result is a solid gel construct with embedded, connected hollow channels. (E) Single and (F) dual layer patterns used for extrusion-based printing. (G) Cross-section of continuous gel layer formed. Hollow tube can be seen embedded in gel layer. (H) Parallel tubes printed continuously using the pattern in (E) show good alignment. (I) Bent connections between adjacent tubes when continuously printed. (J) Multi layer printing using pattern in (F). (K-M) FITC- nanoparticle flow through tubes shown in H-J respectively. Scale bars, 1mm.....55

FIG. 2.4: Dynamic range of printing process using water-based alginate and calcium solutions when outer flow is (A) variable or (B) constant at 10mL/min. (A) shows points at which experiments were performed. (A-i) Illustration of gel displacement during operation above maximum speed. Because extrusion speed is significantly lower than that of the printhead, the tube is not given sufficient time to gel and settle on the substrate. This causes a displacement between intended patterning position and actual position. (A-ii) Flow instabilities occurring from operation below minimum speed. (A-iii) Parallel printed tubes resulting from printer operation in the optimal working range show good alignment.....59

FIG. 2.5: Dynamic range of printing process using DMEM or EBM-based alginate and calcium solutions with 2% or 10% FBS when outer flow is (a) variable or (b) constant at 7mL/min. (Red) >15% displacement. (Orange) 5-15% displacement. (Green) <5% displacement – working range. (Blue) Flow instabilities.....61

FIG. 2.6: (A) Inner tube diameter changes with respect to printhead speed and CaCl₂ flow rate. (Blue) 5mL/min. (Red) 10mL/min. (Green) 15mL/min.

(Purple) 20mL/min. Outer flow constant at 10mL/min. Tube diameters are found to decrease at lower flow rates and higher printhead speed. (B) Experimental and theoretical values of channel diameter at minimum printing speed. Minimum printing speeds were 5, 6, 7, and 9m/min for 5, 10, 15, and 20mL/min respectively. (B-i) Coaxial nozzle illustration showing core (d) to nozzle (D) diameter ratio for calculating tube diameters.....62

FIG. 2.7: (A-C) Schematic images illustrating single gel structures with varying changes in tube diameters: (A) stepwise, (B) alternating and (C) continuous increase or decrease in embedded channel dimensions. Dynamic change of tube diameters in a single gel structure is accomplished by varying CaCl₂ flow rates: (D) flow rate is increased stepwise (ramping) (E) flow rate is changed back and forth (pulsatile) (F) flow rate is changed continuously. X, Y, Z represent tubes generated by 15, 10, and 5mL/min flow respectively. Outer flow constant at 10mL/min. Scale bars, 1mm.....64

FIG. 2.8: Printing using variable concentrations of water-based alginate and calcium chloride solution. Similar results were observed using cell media-based solutions. (A) Unsuccessful printing using 0.5% alginate solutions. Uncrosslinked liquid droplets were dispensed. Similar results were observed using 1% solutions. (B) Unsuccessful printing using 25mM calcium solution. Amorphous, crosslinked gel droplets were produced. Similar results were seen using 50mM solutions. (C) Successful printing using 100mM calcium solution and 2% alginate results in channel fabrication. Similar results were observed using 75mM and 1.5% calcium and alginate solutions respectively. (D) Close-up of parallel channels in (C)65

FIG. 2.9: Effect of printhead speed on a 90° change of orientation. Tubes are printed using a flow rate of 10mL/min at a speed of (A) 5 m/min, (B) 5.5 m/min (minimum speed), and (C) 20 m/min. Printing even slightly below the minimum speed (A), causes an overshoot to occur. At minimum speed (B), the tube forms a right angle when printing orientation is changed, while printing at higher speeds produces a curved tube (C). Dashed arrows indicate printhead motion path for intended filament extrusion. Scale bars, 2mm.....66

FIG. 2.10: (A) Gel layer with embedded hollow tubes, seeded with GFP Escherichia Coli-K12. Scale bar, 2mm. (B) Cross-section of hollow channel embedded within HUVEC-laden gel. Scale, 500µm. (C) Cross-section of HUVEC embedded within gel. Cell organelles are visible. (D-G) Z-stack montages taken at intervals of 20µm, showing live/dead stain of gel constructs. Calcein indicates intracellular esterase activity by emitting green fluorescence, while ethidiumhomodimer is the red fluorophore indicative of plasma membrane

integrity loss. (D, E) HUVEC-laden 3D printed gel constructs with embedded hollow channels, imaged on (D) Day 1 and (E) Day 3 post-printing. Constructs are printed at flow rates of 7mL/min at a printhead speed of 5m/min, and are re-perfused with media daily. (F, G) HUVEC-laden 1mm thick alginate gel layer on (F) Day 1 and (G) Day 3 post cell seeding. Scale bars, 1mm.68

FIG. 2.11: Cell viability analysis over a 72hour time period. Fabricated hollow channel samples were compared to non-hollow alginate films cast at a 1mm thickness. Single asterisks (*) represent p-level<0.05 and double asterisks (**) p-level<0.01, indicating a significant difference between groups.....69

FIG. 3.1: A) A low-cost, open source 3D printer (RepRap Ormerod) that has been modified by removing the original nozzle and replacing it with a custom, microfluidic nozzle. B) Scalable design allows incorporation of multi-axial extrusion. A 3D printed bracket was used to stabilize the embedded needles during printing in order to maintain proper alignment. C) Custom-made tri-axial PDMS nozzle. Patterned channel is 2mm in diameter. Patterned needle tracks are used to guide the needles to the center of the channel, as shown in (i).....78

FIG. 3.2: A) Triaxial extrusion of calcium and alginate flows. Dyed solutions allow visual differentiation between the hierarchal layers. The inner alginate flow (blue) and outer alginate flow (yellow) can be seen, while the calcium flow is left un-coloured. B) A hollow gel tube is produced upon extrusion, and the separate concentric layers can be clearly distinguished from one another.....79

FIG. 3.3: 3D fabrication of hydrogel scaffolds. A) Triaxial extrusion of a bilayered conduit that has been deposited onto a dry substrate. When the conduits are patterned in close proximity to one another, the outer uncrosslinked gel layers of adjacent, parallel tubes fuse together and result in a solid B)single-layer (~1.6mm thickness) or C)multi-layered gel film (~3.2mm thickness) being formed with embedded hollow channels. D) Modification of the scalable microfluidic nozzle design allows multi-axial extrusion that can be used to create conduits with multiple distinct gel layers and a hollow core. Up to three concentric gel layers surrounding the hollow core can be seen in (D). E) Versatility of the device allows it to be successfully used for creating and patterning solid fibers with several concentric gel layers.....83

FIG. 3.4: Representative images for each condition within the printing range. A) Printing within the operational range at the optimal printspeed produces viable, well-aligned tubes with distinct concentric gel layers and a hollow core. B) When the extrusion velocity of the hollow tube increase beyond the maximum speed of the printer (black) flow instabilities occur. C) Increased alginate flow rates relative to calcium flow results in insufficient crosslinking of outer-most layers (yellow) and leads to blotting or mixing of solutions during printing. D) (i)An inner alginate flow that is

significantly greater than the outer alginate flow does not produce distinct gel layers due to the outer flow being overtaken by the inner flow. (ii) At higher calcium flow rates, an inner alginate flow that is significantly lower than the calcium flow rate results in flow instabilities and is not suitable for producing a hollow core.....86

FIG. 3.5: Mapping of the dynamic printing range of the tri-axial extrusion device. All flow rates are varied between 1-6mL/min. Each graph represents a different calcium flow rate – graphs A) to F) represent calcium flow rates of 1 to 6mL/min respectively. Printing within the operational range (green) at the optimal required printspeed (indicated in m/min on each point in the operational range) produces viable, well aligned tubes with distinct concentric gel layers. All other mapped regions are non-operational due to clogging, insufficient crosslinking, non-triaxial extrusion, or surpassing the printspeed threshold. Low alginate flow rates cause consistent clogging of the microfluidic nozzle (red). Insufficient crosslinking (yellow) occurs due to high alginate to calcium volume ratios. Non-triaxial extrusion (orange) is a result of an inner alginate flow that is significantly less than the calcium flow, or an inner alginate flow that is significantly greater than the outer alginate flow. If gel extrusion velocity is greater than the maximum printspeed threshold (16m/min), flow instabilities occur.....87

FIG. 3.6: (A-B) Effect of varying calcium concentration on viable printing range, with 2% alginate concentration and calcium flow rates held constant at 3mL/min: (A) – 25mM and B) – 175mM). (C-D) Effect of varying alginate concentration on viable printing range, with 100mM calcium concentration and calcium flow rates are held constant at 3mL/min: (C) – 1.5% and D) – 2.5%).....89

FIG. 3.7: (A-C) Effect of varying flow rates on conduit dimensions. Under each condition, two flow rates are held constant while one is varied. Calcium, inner, and outer alginate flow rates are varied in A), B), and C) respectively. D) Effect of printspeed on conduit dimensions, while flow rates are held constant.....92

FIG. 3.8: Multi-cellular printing. A) Hollow gel tube is printed with two distinct, hierarchal layers. The inner layer contains HUVECs while the outer layer contains 3T3s, as would normally be found in a typical blood vessel architecture. Structure is imaged on Day 1. B) Merging of two parallel printed tubes results in the formation of cell-laden (HUVECs) conduits embedded in a surrounding bulk ECM that contains secondary cells (3T3s). Structure is imaged on Day 1. Central, cross-sectional slices are seen in (A-i) and (B-i), while the (A-ii) and (B-ii) show top slices of the constructs. These confirm that the hierarchal architecture is maintained in the X, Y, and Z planes. C) HUVECs and 3T3s behave differently when encapsulated in the hollow alginate structures. (C-i) HUVECs do not migrate or line the channel, but rather remain encapsulated in the alginate and quickly decrease in viability. Image is taken on day 7,

after which point very few live cells remain. (C-ii) 3T3s migrate into the lumen and form a hollow monolayer of cells that line the inner side of the channel. Image is taken on day 21.....94

FIG. 3.9: Multi-material printing is feasible using triaxial extrusion, which allows weaker matrices that are more cell-friendly to be printed with the support of stronger, structurally sound materials. Hollow gel structures printed using an inner supporting layer of alginate and an outer HUVEC-laden layer of A) alginate-collagen or B) alginate fibrin. Images show that cells are encapsulated within the outer-most layer. C) Dissolving the alginate using citrate allows the cells to adhere to the fibrin layer, showing good morphology, and form an endothelial wall. D) Printing of these cell-laden hybrid materials results in increased live cell counts over a 5-day period in comparison to structures printed using only alginate. Single asterisk (*) represents p-level<0.01.....97

FIG. 4.1: Schematic of the Casting, Peeling, Stacking (CPS) strategy used for fabrication of 3D structures with embedded hollow channels. 1. Uncrosslinked liquid polymer is deposited onto the 3D printed patterned molds. The solution spreads evenly 2. Upon gelation, a solid layer is formed and the firm gels are easily peeled and removed from the molds. 3. Adhesive is deposited in between patterned gel layers, and films are stacked upon one another thereby creating embedded hollow features within the bulk of the construct.....106

FIG. 4.2: A) i) Large hollow channel fabrication by adhesion of molded Alg-Col-EBM hydrogel onto flat film. Scale bar, 1mm. ii)Hollow channels maintain their structural integrity (iii) These channels are easily perfusable as seen by the injected air bubbles. B) i)Branched hollow channel network embedded in media-based hybrid gel via planar processing. Channel dimensions are 200µm width by 400µm height. ii)When the branched network is perfused without any adhesive used to bind the layers, injected media leaks out of the channel and in between the two layers. iii)When the branched network is perfused post adhesion using 0.01% SiC, media flows easily from one end of the construct to the other. There is no observed flow obstructions or leakages. C) i)Perfusion of high-resolution channel network patterns adhered with SiC. Channel cross-sections are 150x200µm and are spaced 500µm apart. Scale bar, 1cm. ii)Confocal microscopy used to image microchannels in (i). iii)Z-stack projection showing live stain of cells seeded in the hydrogel matrix surrounding the patterned microchannels seen in ii), thereby demonstrating maintenance of cell viability in bulk regions.....108

FIG. 4.3: A) Cross-section of embedded hollow microchannels following SiC adhesion of two hydrogel layers. Fabricated hollow channel dimensions varied over a wide range (250µm-1mm). B) SEM image of cross-section seen in (A). C) Cross-sectional image

thick, multilayered hydrogel (8mm) containing embedded channels of varying sizes. This demonstrates the ability to perfuse large, thick constructs such that nutrients can be transported to bulk regions of the construct that are otherwise unreachable.....109

FIG. 4.4: Lap shear tests were performed on hydrogel samples of varying material compositions, adhered using nanosilica solution or SiC. Control values indicate samples tested without any interfacial adhesive applied. Both adhesives were found to be ineffective with water-based alginate alone, while nanosilica and SiC demonstrated some effect upon the incorporation of collagen. Both adhesives achieved successful bonding to varying degrees when used with media-based alginate or hybrid hydrogels. Single asterisks (*) represent p-level<0.05 and double asterisks (**) p-level<0.01, indicating a significant difference between groups.....112

FIG. 4.5: Lap shear tests performed on media-based composite gel samples with varying concentrations of each adhesive. A) Maximum stress values for hydrogel samples with 0.001-1% SiC. Maximum bond strength was found to occur at 0.01% concentration. B) Maximum stress values for hydrogel samples with 10-50% nanosilica solution. Bond strengths were maximized at concentrations of $\geq 30\%$113

FIG. 4.6: Lap shear tests performed on media-based composite gels to determine the time duration required for bonding to reach completion. Bonding strengths of SiC and nanosilica compared over a 48hour time period. It was found that nanosilica required >3hours to reach maximum bond strength, while SiC required >12hours.....114

FIG. 4.7: Cytotoxic evaluation of various adhesives when administered onto cell seeded media-based hybrid gels. Comparison of live cell counts (acquired with ImageJ) within samples exposed to each adhesive over a 7-day period. Culture media was renewed every 48hrs. Live cell count maintained in SiC samples, while a significant reduction in cell count was observed in nanosilica samples.116

FIG. 4.8: Ultimate stress values for bonding of media-based hybrid gels to No.1 coverglass. Control values represents lap junction where no adhesive was administered. Double asterisks (**) represent p-level<0.01, indicating a significant difference between groups.117

FIG. 4.9: A) i)Cross-sectional image of 2mm embedded hollow channel in media-based composite hydrogel, post adhesion using nanosilica solution. ii)PVC tube (2mm diameter) was inserted 5mm into the hollow channel. The junction was sealed using 100 μ L of nanosilica. iii)Air bubble was injected into the tube, demonstrating the continuity between the tube and hollow channel. B) Mechanical tests were performed to determine the effectiveness of the bond between the tube and channel. Double asterisks (**) represent p-level<0.01, indicating a significant difference between groups.....118

FIG. S4.1: Ultimate tensile stress for various materials121

FIG. S4.2: Several 3D printed acrylic molds used for casting of hydrogel layers with embedded hollow channels networks of varying dimensions.....121

FIG. S4.3: Mechanical testing apparatus and setup using stained gel. A) Instron machine used for mechanical testing of adhered hydrogel specimens. B) Custom-made grippers used for stabilization of delicate samples.....122

FIG. S4.4: Using a pressure transducer (Edwards Lifesciences LLC, Irvine, CA, USA) and patient monitor (SpaceLabs 90369 Patient Monitor, SpaceLabs Medical Inc.), pressure testing performed by perfusing of a single 200x400µm hollow channel that was fabricated with silicon carbide as an adhesive. Perfusion flow rates were varied in a step-wise manner, and the corresponding pressures were recorded. The channel was found to successfully withstand high pressures, upwards of 300mmHg.....122

FIG. S4.5: Z-stack montages obtained using confocal microscopy, showing live and dead stain of cells embedded within media-based composite hydrogels post exposure to various adhesives. Samples were imaged on day 1, day 3, and day 7 for analysis and compared to a control with no adhesive exposure. Culture media for all samples was renewed every 48hrs. Silicon carbide samples showed good maintenance of cell viability, similarly to the control samples. Nanosilica samples experienced diminished live cell counts by day 3 despite showing promising results within the first 24hours.....123

FIG. S4.6: Confocal microscopy used to obtain fluorescent images of cell-laden patterned hydrogel constructs adhered using silicon carbide. Images show live and dead stain of 3T3 cells embedded in gel surrounding a 400µm patterned hollow channel over a 7-day period.124

FIG. S4.7: A) Lap shear test of media-based composite gel and No.1 coverglass overlap junction. No adhesive was used, and failure occurred due to peeling at surfaces. B) Lap shear test of media-based composite gel adhered to No.1 coverglass using nanosilica solution. Sample undergoes failure due fracture of the gel outside of the lap junction (failure at by tearing).125

FIG. S4.8: Mechanical tests performed polyurethane/composite gel connection to determine the efficacy of the nanosilica in creating a strong bond at the overlapping junction.....125

FIG. S4.9: Qualitative observation of alginate-collagen hybrid gel samples upon administration of various adhesives. Similar observations were seen for alginate samples in the absence of collagen. Images seen in A,B were fabricated using media-based solutions, while images in C,D were water-based. A) Administration of silicon carbide solution did not cause any observable physical change. The sample remained similar in appearance to a control sample with no adhesive administration. B) Sample with nanosilica solution deposition became opaque in appearance as the nanosilica

solidified C) Similarly to media-samples, silicon carbide did not cause any observed physical change to the water-based sample seen here. Control samples also remained similar in appearance. D) Nanosilica administration to the water-based hybrid gel caused the sample to become opaque and cloudy.....126

FIG. S4.10: Imaging of silicon carbide and silica nanoparticles. A) SEM of silicon carbide. Nanoparticles were found to form micron sized agglomerates. B) TEM of primary silicon carbide nanoparticles. C) TEM of nanosilica solution forms a solid layer, but nanoparticles could be observed in between cracks that formed within the layer.....126

FIG. S4.11: A) Characterization of the type of bond failure occurring with each adhesive using various biomaterials: water-based alginate (Alg), water-based alginate/collagen composite (Alg-Col), media-based alginate (Alg-EBM), and media-nased alginate/collagen composite (Alg-Col-EBM). Bond strengths of nanosilica solution and silicon carbide on Alg-Col-EBM samples exceeded the strength of the gel itself, causing fracture by tearing. All other samples failed due to interfacial peeling (failure at joint). B) Tensile tests of Alg-Col-EBM samples coated with various concentrations of nanosilica solution. Coating appeared to reinforce the hydrogel samples. Peak strength occurred at 30% concentration, after which point increased brittleness and reduced elasticity caused samples to fracture at lower stresses. C) Sample force-displacement curve for Alg-EBM gel using nanosilica as an adhesive. All samples that underwent interfacial failure at the joint resulted in similar graphs. D) Sample force-displacement curve for Alg-Col-EBM gel using nanosilica solution as an adhesive. All samples that underwent fracture by tearing resulted in similar graphs. Effect of E) time and F) concentration on the type of failure occurring using nanosilica on Alg-Col-EBM. Frequency of fracture failure increased with time and concentration (80-100% tearing failure rate when >1hrs and $\geq 40\%$). Effect of G) time and H) concentration on the type of failure occurring using silicon carbide on Alg-Col-EBM. Frequency of fracture failure increased slightly when ≥ 24 hrs (10-20% tearing failure rate) and at concentrations of 0.01% and 0.1% (10-20% tearing failure rate)127

FIG. S4.12: Lap shear test of water-based composite gel adhered using silica. Sample undergoes failure due to interfacial peeling between the two surfaces (failure at joint).....128

FIG. S4.13: Lap shear test of media-based composite gel adhered using nanosilica solution. Sample undergoes failure due fracture of the gel outside of the lap junction (failure at by tearing)129

FIG. S4.14: Tensile tests performed on of media-based composite gels with and without outer coating of nanosilica solution.....129

NOMENCLATURE

2D	Two dimensional
3D	Three dimensional
3T3s	3-day transfer, inoculum 3×10^5 cells (mouse embryonic fibroblasts)
ALG	Alginate
AM	Additive manufacturing
CAD	Computer aided design
CAP	Cell adhesive protein
COL	Collagen
DI	Deionized water
DMEM	Dulbecco's Modified Eagle's Medium
DNA	Deoxyribonucleic acid
DPBS	Dulbecco's Phosphate-Buffered Saline
EBM	Endothelial basal medium
ECM	Extra cellular matrix
FBS	Fetal bovine serum
FDM	Fused deposition modelling
GelMA	Gelatin methacrylate
GFP	Green fluorescent protein
HUVECs	Human umbilical vein endothelial cells
LIFT	Laser induced forward transfer
MEMS	Microelectromechanical systems
PCL	Polycaprolactone
PDGF	Platelet-derived growth factor
PDMS	Polydimethylsiloxane
PEG	Poly(ethylene glycol)
PEGDA	Poly(ethylene glycol) diacrylate
PEGMA	Poly(ethylene glycol) methacrylate
PEO	Polyethylene oxide
PGA	Polyglycolic acid
PLA	Poly(lactic acid)
PVA	Poly vinyl alcohol
RFP	Red fluorescent protein
SiC	Silicon carbide
SL	Stereolithography
SLS	Selective laser sintering
TGF-b	Transforming growth factor b
UV	Ultraviolet
VEGF	Vascular endothelial growth factor

Chapter 1

INTRODUCTION

1. Introduction to 3D Tissue Engineering

1.1 Motivation for 3D tissue development:

The investigation of methods for organ and tissue replacement has become a growing research area that has continued to evolve over recent years. The ultimate goal of this cutting edge field of biotechnology is to develop 3D artificial tissues-like constructs that maintain biological function and morphology in order to serve as a replacement for defective human tissue. Although transplantation remains the primary treatment modality for end-stage organ failure, it is not sustainable due to the high demand from a growing patient base and lack of supply due to a shortage of organ donors. In the United States, the number of patients awaiting transplantation has risen from ~23,000 to ~120,000 in the past 15 years, while the number of transplantations has merely doubled from ~15,000 to ~30,000 in that time period [1]. Similarly, in Canada, only 34% percent of end-stage patients are able to receive transplants [2], indicating a large gap between the number of available donors and patients requiring treatment. Additionally, the transplantation surgeries are highly invasive, costly, and the necessary infrastructure is often unavailable in many countries. Therefore, new accessible therapies are needed to treat the millions of patients with organ failure worldwide.

1.2 Conventional approaches for tissue engineering:

Due to the need for organ or tissue replacement at terminal stages, conventional tissue engineering approaches have therefore been investigated as a substitute for transplantation. These methods involve the fabrication of artificial tissues that resemble architectures similar to that of the original tissue, and are composed biocompatible

materials that demonstrate the appropriate mechanical properties. They also allow for cellular penetration and proliferation. This ability to position biological cells, and extracellular matrices (ECM) in 3D is also of significant potential to be used in applications other than organ replacement, such as drug discovery models and biological studies. Some of the various available conventional tissue-engineering approaches include scaffolding techniques, decellularization, and “organ-on-a-chip” systems.

1.2.1 Artificial scaffolding

Scaffold based tissue engineering strategies have generally involved the fabrication of supporting matrices, followed by seeding of cells onto these constructs. Fabricated scaffolds can have a variety of structures including porous, fibrous, and bulk hydrogels and are created using methods such as electrospinning, emulsion, or casting [3–5]. FIG. 1.2a-i shows an example of a tissue engineered artificial bladder composed of fibrous polymer sheets to be used for bladder augmentation in patients needing cytoplasty [6]. The polymer sheets were composed of collagen and polyglycolic acid (PGA), seeded with urethral and muscle cells obtained from the patient, and sutured into the shape of a bladder. The scaffold was anastomosed to native tissue and implanted into the patient, as seen in FIG. 1.1a-ii, and renal function was found to be normal after implantation. Tissue engineering scaffolding techniques have also been commonly used for bone replacement [7] as well as wound healing for damaged skin [8]. However, conventional scaffolding techniques such as the one described are generally suitable for tissues or organs with simple structures since there is limited control in creating more complex shapes and architectures.

1.2.2 Decellularization

Decellularization of tissues is another approach that is taken to create scaffolds with intact geometry, vasculature, and extracellular matrix (ECM), which are then recellularized with native cells and maintained in a bioreactor [9–11]. This involves stripping of the native cells from the organ using detergents such as Triton-X100, and preserving only the underlying matrix and geometry. FIG. 1.1b shows an example of a decellularized organ – a cadaveric rat heart [11]. The decellularized construct was

composed of collagen, laminin and fibronectin. After being recellularized with rat neonatal cardiocytes, maintenance of oxygenation and electrical stimulation allowed the heart to display pumping capacity within 8 day. This technique allows the true organ architecture to be preserved. However, this process is tedious and involves the use of harsh detergents that may have harmful effects such as denaturing of the proteins within the natural ECM of the decellularized organ. There is also a lack of control over precise cell seeding and positioning with this strategy.

1.2.3 Organ-on-a-chip systems

Current “organ-on-a-chip” systems involve culturing cells within microfluidic channel devices composed of a silicon rubber known as polydimethylsiloxane (PDMS) [12]. For example, FIG. 1.2c shows custom designed polyglycerol sebacate (PGS) membranes fabricated using softlithography that were stacked in various orientations to create multi-layered 3D elastomeric scaffolds that promoted cellular alignment for muscle fiber growth [13]. Murine skeletal myoblasts were found to align in muscle-like bundles. Technology to miniaturize and automate dialysis for kidney replacement is also currently being developed using microelectromechanical systems (MEMS) [14,15]. In general terms, MEMS is the fabrication of microcomponents or features on a single chip, thereby creating a “microsystem” that can have sensing and control capabilities. Researchers are currently working toward the design and development of biologically-based biohybrid devices by combining culture of renal cells and silicon membrane-based filtration systems, in hopes of one day creating a functional and implantable artificial kidney. Although these types of systems allow high feature resolution on the micro- or even nano-scale, these devices generally consist of only a single cell type and therefore cannot be considered true models of organs.

1.2.4 Limitations of conventional tissue engineering

Conventional tissue engineering techniques are often limited in the degree of cell seeding, positioning, and penetration that can be accomplished. Incorporation of several different cell types with proper alignment and positioning required for the tissue structure is very difficult. It is necessary to be able to observe the cell-cell interactions occurring in

a 3D environment, which is critical in mimicking organ-level physiology, function or diseases. Therefore, there exists a need for automated 3D fabrication process that are capable of this high degree of precision and versatility in multi-material incorporation. For this reason, researchers began to explore the possibility of using additive manufacturing (AM) for tissue engineering applications, as is discussed in the next section.

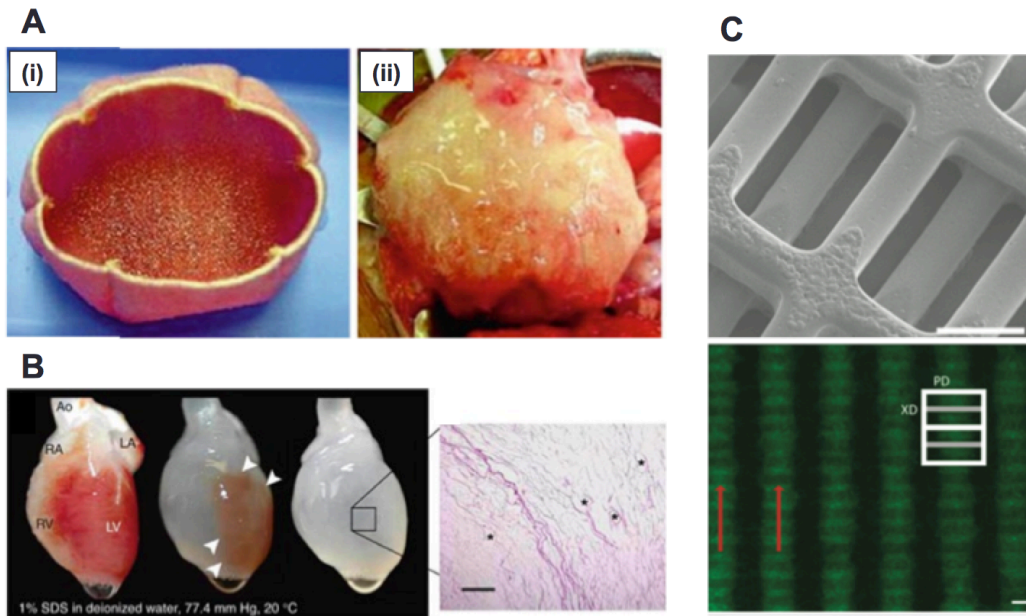


FIG. 1.1: A) (i) Tissue engineered human bladder scaffold is seeded with cells. (ii) The bladder scaffold is anastomosed to native tissue and implanted [6]. B) Decellularization of cadaveric rat heart [11]. C) Stacking of patterned membranes followed by cell seeding leads to controlled muscle-like bundle formation [13].

1.3 Implementing additive manufacturing for 3D tissue engineering

Additive manufacturing (AM) encompasses any 3D fabrication technologies that are based on the use of computer-aided design (CAD) information, which is then converted into a series of cross-sectional layers in order to produce a solid model of that CAD design [16]. AM is often used synonymously with three-dimensional (3D) printing.

In 1981, the first 3D printing strategy was published [17], which outlined the use of photo-hardening materials under ultraviolet (UV) light exposure to automatically fabricate 3D models. It wasn't until 1984 that this type of technology was patented when Charles Hull first introduced the concept of stereolithography (SL), which still remains

one of the most popular printing techniques used to date [18]. He also designed and developed the associated 3D printing file format (.stl), which is now widely used and accepted. Only three weeks prior, two French inventors had made a similar attempt to patent the stereolithography process, but were unsuccessful in receiving support as their technology was viewed as lacking business perspective [17].

At the end of the decade and throughout the 1990's, significant progress was made in this field when two other widely used 3D printing techniques were also developed [19]. In 1989, fused deposition modelling (FDM) was patented and trademarked. This process involved heating thermoplastic materials such that filaments could be deposited and fused together layer by layer to build 3D structures. By the mid-1990's, metal printing techniques were also developed, including selective laser sintering (SLS). Powdered metals were fused together under a laser beam for scaffold assembly, thereby allowing complex geometries to be realized.

In 1999, there was increased interest in using 3D printing for tissue engineering applications. This occurred following emerging reports of an artificial bladder fabricated using conventional scaffold-based tissue engineering techniques (as described in the previous section). This was the first account of an artificially tissue engineered organ [20] that was successfully transplanted into several different patients [6]. It was at this turning point that researchers began to explore the idea of implementing 3D printing technologies for medical purposes in order to create more complex organ or tissue architectures. When used in the context of tissue engineering, 3D printing processes are now referred to as bioprinting. A simple way to envision a bioprinter is to compare it to a conventional desktop printer. The conventional printing process requires three components in order to operate – ink, paper, and a printer. In the case of bioprinting, biological materials such as cells are used instead of ink, and biocompatible scaffolding matrices serve as a replacement for paper (FIG. 1.2). The bioprinter itself possesses unique characteristics in comparison to a conventional 3D printer, such as sterile incubated environments that allow it to successfully print these biomaterials. The use of high temperatures, UV, and post-processing solvents that are often used with conventional 3D printers are avoided, as they can be harmful to cells.

The past two decades have brought an influx of research and development in 3D printing technologies for use in tissue engineering applications, which have now come to encompass a variety of techniques including both extrusion printing and non-extrusion based 3D fabrication strategies. These methods are discussed in detail in the next section.



FIG. 1.2: Schematic illustrating the various components required for additive manufacturing of an artificial 3D tissue or organ.

2. Additive Manufacturing Techniques for 3D Tissue Engineering

There are a variety of AM techniques currently being utilized for tissue engineering applications. Unconventional tissue engineering techniques involving AM are advantageous over conventional approaches due to the increased control and versatility in material patterning. Majority of these techniques can be categorized as either extrusion-based, non-extrusion based, or hybrid processes (FIG 1.3).

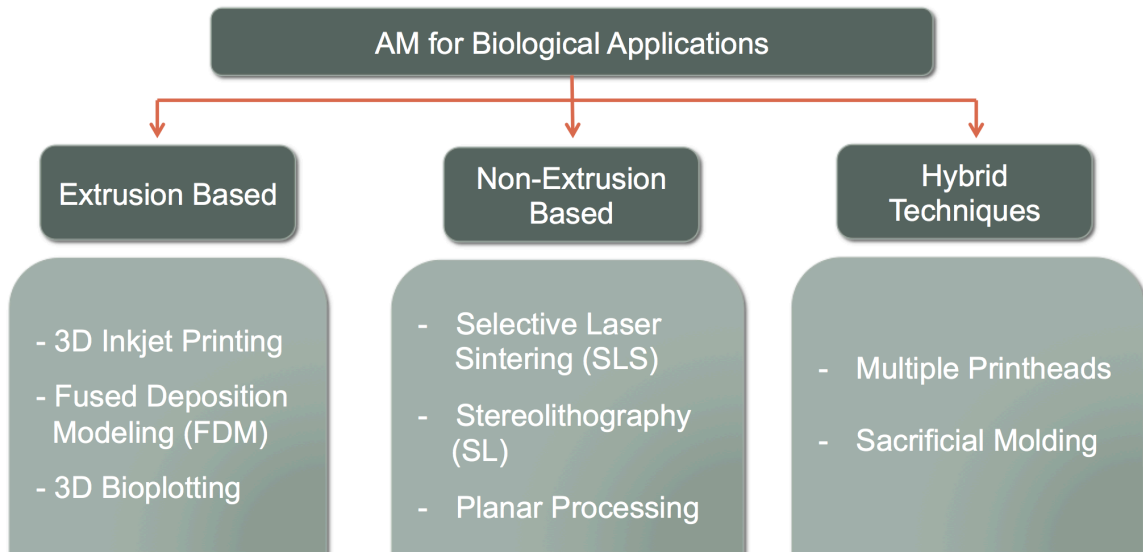


FIG. 1.3: Schematic illustration describing the different types of AM technologies available for bioapplications.

2.1 Extrusion-based AM:

Extrusion-based AM techniques involve droplet or filament deposition by means of an extruder or nozzle onto a substrate, and 3D constructs are built up layer by layer in this way. This section discusses some of the various types of extrusion-based AM.

2.1.1 Inkjet printing

One of the most popular extrusion-based strategies is high-resolution inkjet printing, which operates by ejecting minute ink droplets using electrostatic or pressure-driven methods as shown in FIG. 1.4a,i. Heat is often avoided in order to avoid damage to living cells. This system has already been used for years to print “bioinks” consisting of cells, deoxyribonucleic acid (DNA), ECM, antibodies, enzymes, or soft materials such collagen and fibrin at low concentrations [21,22]. FIG. 1.4a,ii shows microseeding of living endothelial cells with high-resolution spacing. This work demonstrates advanced control of the ejected dot size and the number of cells in each dot, without negatively affecting cell viability. When used in combination with ECMs, inkjet printing can be used to fabricate 3D structures, For example, this technique has been used to create multi-layered cell-laden gels wound healing and skin tissue engineering following an extensive burn [23]. Several layers of stem cells mixed with collagen and fibrin are inkjet printed onto the wound site. Researchers found that successful skin regeneration and vascularization occurred using this technique. Inkjet printing is useful when high resolutions and precise single-cell positioning is required. However, a major shortcoming of these systems is the decreased structural integrity and mechanical strength of the materials used for printing.

2.1.2 Fused deposition modelling

Fused deposition modeling (FDM), on the other hand, has been used to create 3D multi-material scaffolds using hard, high strength materials. Various thermoplastic polymers are generally used for this, such as poly(ϵ -caprolactone) (PCL) or poly(lactic-co-glycolic acid) (PLGA) [24,25]. Polymers are extruded in a semiliquid state and precisely patterned in ultrathin layers. As the extruded material solidifies, it adheres to the preceding layer. FDM-based scaffolds have been predominantly used for hard-tissue

replacements in bone tissue engineering [26,27] as well as cartilage repair [28] using polymer-ceramic composites. For example, FDM has been used to print PLGA scaffolds for cartilage tissue engineering by depositing criss-crossing filaments layer by layer in order to create a 3D lattice structure [29]. These constructs were then seeded with mixture of collagen and chondrocytes, which were found to successfully grow and proliferate over a 28-day period. FDM is an ideal method for hard-tissue engineering purposes. However, it cannot be used for soft material or hydrogel fabrication. Therefore, it is not an effective technique for applications that require cell encapsulation due to the high temperatures necessary for extruding molten materials. Another drawback is the low feature resolution, which is caused my limitations in achievable extrusion nozzle orifice size as well as spreading of the dispensed material during deposition. This technique also requires that cell seeding be done post-printing, which means that cell placement is not controlled and precise position is not possible. Therefore, structured layers with multiple cell types cannot be created.

2.1.3 3D Bioplotting

Due to the limitations of FDM, 3D bioplotting has been specifically used to fabricate 3D cell-laden hydrogel scaffolds [30–32]. Viscous plotting material is dispensed either onto a dry substrate or into a liquid medium with a matching density as shown in FIG. 1.4b,i. In this way, complex architectures can be fabricated without any temporary support structures. Cells may be encapsulated within semi-gelled materials such as collagen or alginate, and then dispensed using this technique. For example, FIG. 1.4b,ii shows an example of one of the first 3D bioplotting structures [31]. Agar gel filaments were printed layer by layer into a liquid medium, thereby creating a simple cubic gel structure. Researchers later proceeded to fabricate more complex soft material architectures, such as an ear auricle scaffold [32]. This was done by printing low-viscosity alginate pre-seeded with viable chondrocytes and cross-linking with calcium sulphate prior to deposition. The matrix was printed along with silver nanoparticles (AgNPs) to serve as the conducting electrodes, and the artificial ear auricle was found to be capable of auditory sensing for radio frequency reception. 3D bioplotting allows controlled positioning of various cell types within a single construct, while maintaining

structural integrity and creating complex geometries. However, similarly to FDM, 3D bioplotting also has low feature resolution due to limitation in nozzle orifice size and the gelation/solidification rate of the dispensed material.

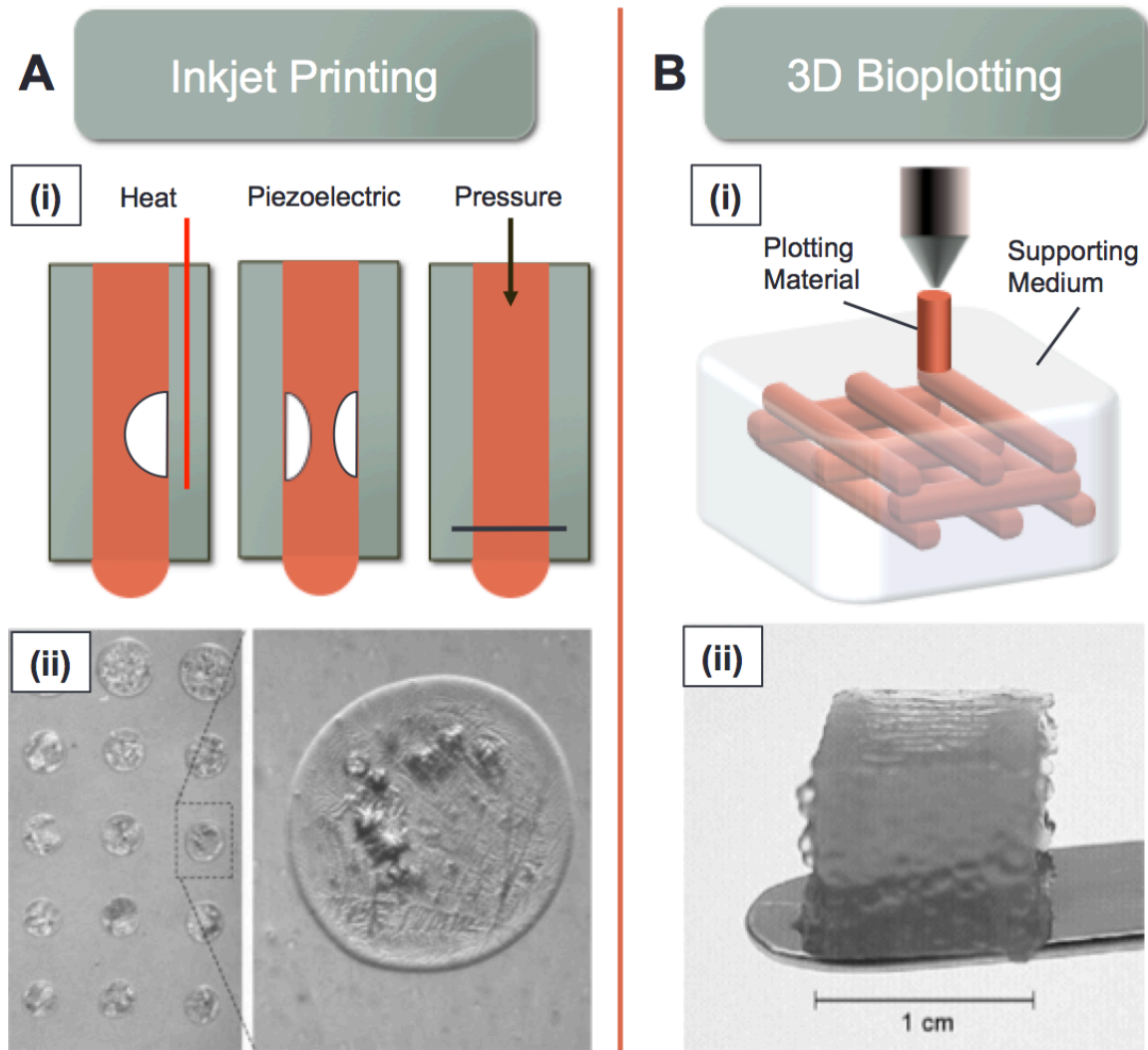


FIG. 1.4: Extrusion-based AM techniques. A) (i) Schematic illustrating inkjet printing process, where precise bioink deposition is achieved using heat, piezoelectricity, or pressure. (ii) Piezoelectric inkjet printhead used to deposit cell-culture media dot containing 1-4 endothelial cells [21]. B) (i) Schematic illustrating 3D bioplotting technique, where viscous hydrogel material is crosslinked upon deposition in order to create 3D constructs. (ii) Agar gel cube fabricated using 3D bioplotting [31].

2.1.4 Limitations for extrusion-based AM

While there may exist some variation in material or resolution capabilities of the extrusion-based AM systems discussed above, these processes generally have the common advantage of performing fast 3D fabrication. They can also be found to be relatively low cost. However, these techniques can often also be associated with difficulties in controlling flow rates, clogging complications, and transient fluid behaviour. For these reasons, non-extrusion based methods are sometimes used for tissue engineering applications, as is discussed in the next section.

2.2 Non-extrusion based AM:

Non-extrusion based strategies involve build volumes filled with uncrosslinked material that is subsequently solidified in a pre-specified pattern using light or laser exposure. Such systems include selective laser sintering (SLS), stereolithography (SL), and planar processing techniques, which can be used as viable options.

2.2.1 Selective laser sintering

In selective laser sintering (SLS), a carbon dioxide laser beam sinters material particles together by heating them above the glass transition temperature. During sintering, molecular diffusion along the outermost surface of the particle leads to neck formation between neighbouring particles. Any powdered biomaterial that will fuse but not decompose under a laser beam can be used for scaffold assembly by SLS (e.g. PCL, polylactic acid – PLA, or metals such as titanium) [33–35]. These types of materials mean that SLS is used exclusively for hard-tissue engineering. For example, SLS was used to create 3D titanium structures with porous surfaces for bone tissue engineering [36]. These constructs were used as artificial bone and were implanted in rats as a replacement for the scapula. Researchers found that 2 months post-implantation, the implants were well integrated and demonstrated native bone tissue ingrowth with no adverse effects. SLS has the advantage of being able to create high-resolution features, which is determined by the powder particle size. However, like FDM, it is not suitable for hydrogel fabrication or cell encapsulation, meaning that multiple cell types cannot be precisely positioned within the structures.

2.2.2 Stereolithography

During fabrication by SL, photo-curable polymers are loaded into the build area and irradiated with ultraviolet (UV) light in a precise pattern, which is defined by CAD files (FIG. 1.5a,i). Excitation of photoinitiator molecules by the UV light causes polymerization of the photosensitive resin and formation of a solid phase of the material. Similar to FDM, SL has been widely used for development of biomimetic bone substitutes using materials such as PCL [26,37–40]. Recent work involving SL of cell-encapsulated hydrogels for soft tissue applications has become much more prevalent. Poly(ethylene glycol) diacrylate or methacrylate (PEGDA or PEGMA) are most often used and have been integrated with various types of cells, including fibroblasts, ovarian cells, hepatocytes, as well as several mammalian cells [41–46]. However, these techniques often demonstrate poor cell viability due to photo-toxicity [44,45]. One group utilized visible light instead of UV radiation in order to 3D fabricate fibroblast-laden PEGDA/gelatin structures [46], as seen in FIG. 1.5a,ii. However, the increased photoinitiator concentrations required to achieve sufficient crosslinking can have adverse effects on the cells over long-term periods. Similarly to SLS, stereolithography can achieve high-resolution features, but has limitations in cell viability due to toxic reagents.

2.2.3 Planar processing

This problem can be overcome by using planar processing. Planar processing is a simple method by which multi-layered 3D structures may be created by means of soft lithography micromolding (FIG. 1.5b,i). A mold is fabricated generally using SL technology or photolithography due in order to create fine, high-resolution features. The polymer of choice is patterned by casting, crosslinking, and then removing the solidified polymer film from the mold. These individual scaffolding layers are stacked and cured onto one another, thereby creating a thick, multi-layered 3D constructs [47]. This technique allows the creation of highly viable cell-laden soft material scaffolds with intricate embedded features that can serve as guiding tracks for controlled cell alignment and adhesion [48], or as perfusable networks for nutrient delivery [49,50]. For example, one group created perfusable microchannel networks by casting gelatin methacrylate

(GelMA) into PDMS molds and removing the structure once it had solidified via photocrosslinking [48,51]. These channels, seen in FIG. 1.5b,ii, were perfused with endothelial cells that were able to self-organize into 100 μ m fiber-like bundles, thereby demonstrating microscale control of cellular alignment. The advantage of planar strategies is that they allow for the fabrication of viable cell-laden scaffolds without compromising the high resolution and precision of patterned features. However, longer processing times are required as well the identification of appropriate lamination techniques that will not hinder the embedded features.

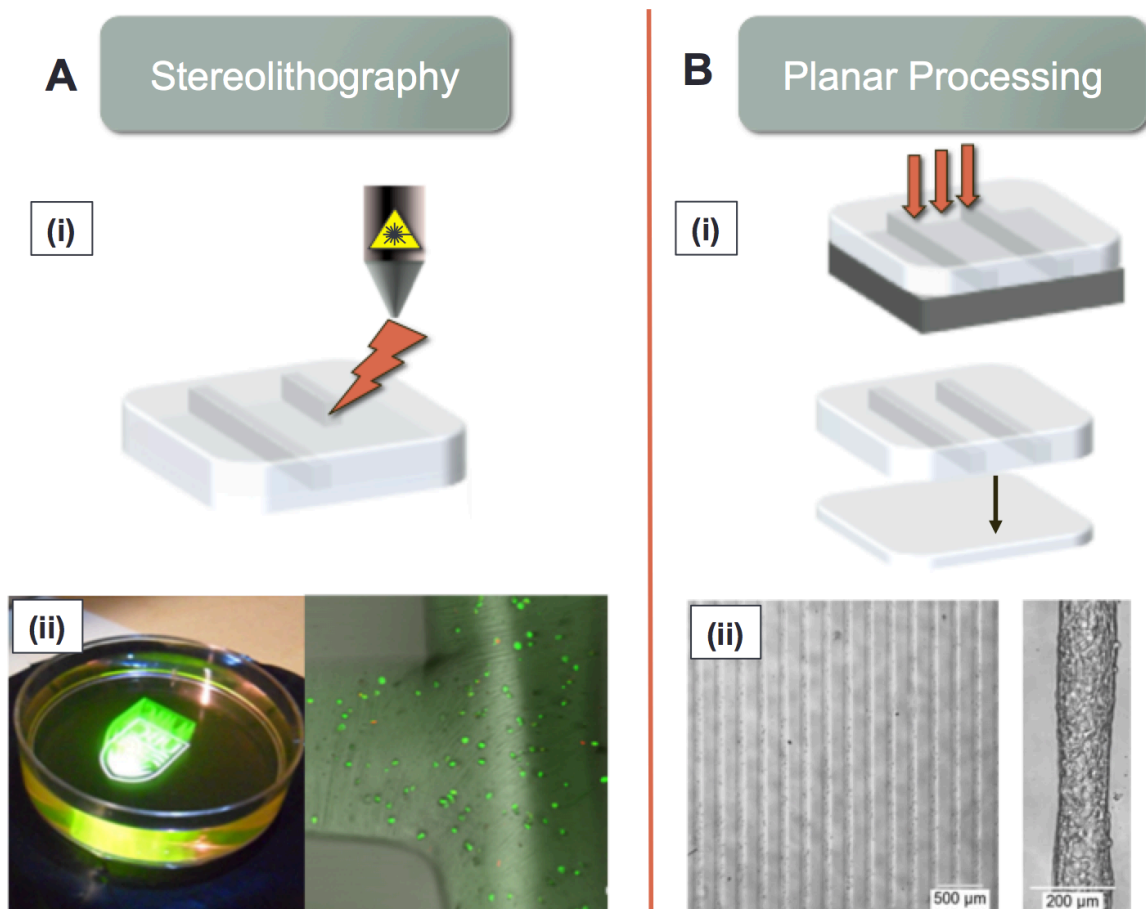


FIG. 1.5: Non-extrusion based AM techniques. A) (i)Schematic illustrating SL process, where precise pattern definition is achieved using light induced polymerization. (ii)SL is used to fabricate 3D PEGDA/gelatin methacrylate structures with encapsulated fibroblast cells [46]. B) (i)Schematic illustrating planar processing technique, where soft lithography micromolding followed by stacking of individually patterned polymer sheets is used to create 3D structures. (ii) Perfusable microchannel networks fabricated by casting and photocrosslinking of GelMA [48].

2.2.3 Limitations of non-extrusion based AM:

Non-extrusion based techniques are ideal for achieving high-resolution features as they are only limited by material particle size and the focal spot size of the light/laser beam. However, these methods also require several post-processing steps (e.g. extra sintering in the oven for SLS and lamination for planar processing), are expensive, and involve long, time-consuming operational times. Therefore, in additive there seems to be a trade-off between achievable feature resolution vs. time and cost.

2.3 Hybrid techniques:

Some AM strategies involve a combination of various techniques in order to achieve 3D fabrication –these methods are referred to as hybrid techniques.

2.3.1 Multiple printheads

Some research groups have demonstrated the use of multiple AM strategies in order to create 3D constructs with multi-material properties and increased structural complexity. One group reported a hybrid inkjet strategy involving dual extrusion heads for both droplet formation and electrospinning has also been developed (FIG. 1.6a,i) [52]. This system creates 3D constructs by alternating between layer deposition of electrospun polymer and cell-laden hydrogel. FIG. 1.6a,ii shows 3D constructs for cartilage tissue engineering that have been 3D fabricated in this way [52]. The structural integrity and mechanical strength of the construct is increased in this way, which is often a shortcoming of conventional inkjet printing. However, these types of hybrid techniques can often become tedious in controlling the individual printheads and the required material extrusion properties.

2.3.2 Sacrificial molding

Another hybrid concept, called sacrificial molding, combines extrusion printing with bulk immersion. A temporary material is printed in the required pattern and then embedded within an external matrix. The material is removed (or “sacrificed”) by means of thermoreversible properties, mechanical force, or dissolution, leaving behind the

embedded pattern (FIG. 1.6bi) [53–56]. This technique has proven to be particularly useful in vascular tissue engineering applications. For example, FIG 1.6b-ii shows a carbohydrate glass lattice that is printed using FDM and then encapsulated within an ECM [56]. The matrix is submerged in an aqueous solution, which dissolves the filaments and leaves behind a network of hollow channels. Sacrificial molding techniques are particularly useful for vascular tissue engineering applications due to their ability to create hollow channel features embedded within bulk ECMs. However, the removal processes that exploit specific physical properties can compromise the hydrogel scaffold stability. Additionally, the fabrication and removal processes associated with sacrificial techniques involve multi-step processes that can become lengthy and time consuming.

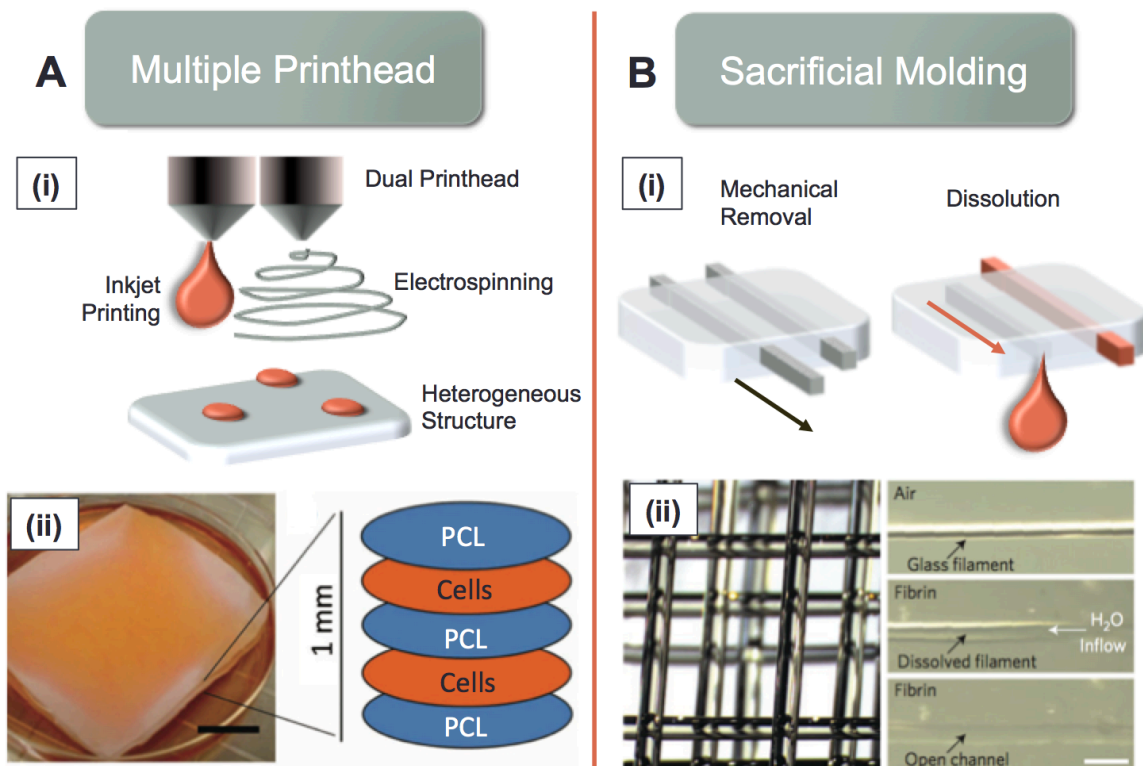


FIG. 1.6: Hybrid AM techniques. A) (i) Schematic illustration demonstrating the combined use of inkjet printing and electrospinning. (ii) Hybrid technique is used to create tissue engineered cartilage tissue by fabricating alternating layers of PCL and chondrocytes [52]. B) (i) Schematic illustration showing sacrificial molding processes by mechanical removal of spacers or by liquefaction. (ii) Carbohydrate glass is 3D printed using FDM, followed by embedding into a hydrogel matrix and then dissolving with water in order to leave behind a hollow interconnected channel network [56].

2.3.3 Limitations of hybrid techniques

Hybrid techniques allow the users to create architectures that are increasingly complex both functionally and structurally by combining the advantages of different systems in order to achieve a particular goal. However, because they require a combination of different systems, the process becomes time consuming, tedious, and in some cases more costly.

3. Vascularization as a Major Challenge in 3D Tissue Engineering

In recent years, AM technology has begun to be used clinically for some tissue engineering applications – specifically for bone and skin tissue replacement. The appropriate AM technique is selected in each case based on the required material and structural properties of the specific bioapplication. For example, 3D printing is currently being used clinically for bone and dental implant fabrication [35,57]. Because the majority of these implants are manufactured using titanium and titanium alloy (due to its high biocompatibility), SLS is most commonly used for this application, as it is the only technique capable of printing metal. 3D skin printing is another AM application that is quickly approaching clinical trials [23]. Researchers are using inkjet printing following an extensive burn in order to induce wound healing. Because skin is one of the less complex tissues found in the body and has weaker mechanical properties, inkjet printing is an ideal strategy for recreating its simple architecture. It is therefore important to consider the advantages as well as limitations of each AM technique when fabricating 3D artificial tissues.

While bone and skin 3D tissue engineering have reached clinical trials, 3D biofabrication of more complex soft tissues and organs still remains far from realization. This is because one of the major current technical challenges with 3D artificial tissue fabrication is the integration of vascular networks within tissues [58]. Without the incorporation of functional vascular networks into 3D engineered tissues, the cells cannot survive. Mammalian cells require a constant oxygen supply and waste disposal mechanisms in order to survive. Conventional techniques for vascular tissue engineering

involve grafting of a singular tubular structure formed by rolling polymer sheets and seeding them cells isolated from the patient [59]. However, this strategy does not allow for the fabrication of larger, multi-scale hollow channel networks embedded within thick 3D tissue-like constructs, which can serve as vascular networks. It also does not allow for the spatial resolution and architectural complexity that can be achieved using AM technology.

This section discusses recent research work that has focussed on establishing AM methods for creating vessel-like structures and perfusable hollow channel networks. It is important to have an understanding of the basic vascular architecture as well as the drawbacks associated with conventional vascular engineering techniques used in the past, so that new alternative methods can be developed. Unlike conventional techniques, unconventional AM techniques allow precise patterning of biomaterials and cells to create hierarchal structures, as well as fabrication of embedded high-resolution hollow channels for perfusion.

3.1 Vessel formation and architecture:

There are two stages of vascular network development: vasculogenesis and angiogenesis. The first involves formation of a primary capillary network, while the latter refers to the formation of new capillary vessels from pre-existing microvessels [60]. Growth factors such as vascular endothelial growth factor (VEGF) and basic fibroblast growth factor (bFGF) can increase formation of new vessels [61]. Newly formed vessels are stabilized by recruitment of smooth muscle cells or pericytes to the vessels and the subsequent production of an extracellular matrix. Although there are various types of blood vessels, the 3 main ones include arteries, veins, and capillaries. The architecture of these vessels varies slightly due to their function and size, the largest and smallest of which are arteries and capillaries respectively. All of these vessels have a common, inner endothelial cell layer that forms the lumen, which is called the tunica intima [62]. Arteries and veins also include a surrounding smooth muscle layer called the tunica media, as well as a third external layer consisting of fibroelastic tissue (the tunica adventitia) to aid in pumping and dispersing the blood. FIG. 1.7 shows a schematic representation of the various concentric layers that compose a biological vessel.

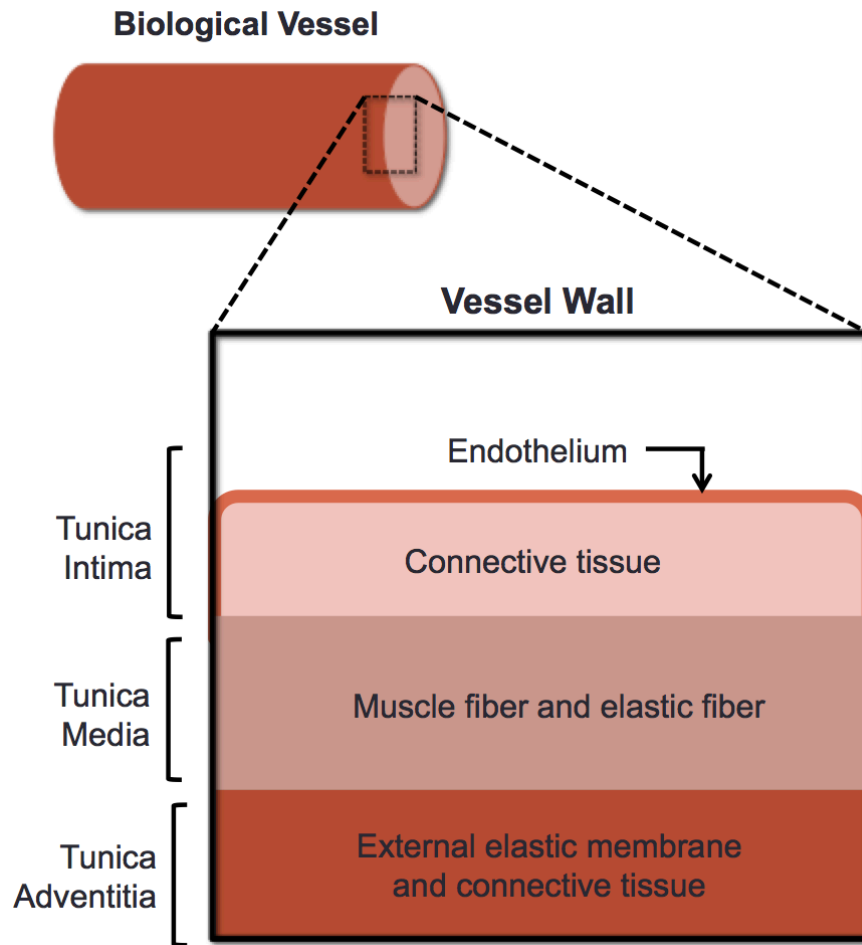


FIG. 1.7: Anatomical depiction of the 3 layers that compose a vessel wall.

3.2 Conventional techniques:

Traditional solutions to the issue of vascular tissue replacement involved grafting of autologous vessels [63], which means vessels are obtained from the same patient. However, there is often a limitation in the availability of autologous vessels suitable for grafting. Therefore, in such cases conventional tissue engineering approaches such as artificial vascular graft fabrication and prevascularization are used.

3.2.1 Artificial vascular grafting

The first account of human application of a tissue engineered vascular graft was in 1999 [63]. This involved implantation of a biodegradable polymer scaffold (composed of PCL and PGA) that was seeded with cells isolated from a peripheral vein explanted

from the patient (FIG. 1.8). Following implantation in the pulmonary artery, the patient was found to be doing well with no signs of complication. However, this process has often been associated with significant morbidity, surgical costs and restenosis. This is due to tissue trauma that can occur during the invasive surgery, as well as immune rejection of the foreign material. There has been some success found with classical tissue engineering using tubular scaffolds composed of fibrous co-polymers (PGA and poly-L-lactic acid – PLLA) [4,59]. For instance, one group seeded these scaffolds with autologous bone marrow-derived cells as an alternative to vascular cells. This is because venous explantation requires invasive surgical procedure, which has associated risks that are inherent to any operation. Therefore, another more accessible cell source was used in this case. These scaffolds were first successfully implanted inferior vena cava of dogs [4], then subsequently used as cavopulmonary connections in several patients [59]. Following implantation, no signs of thrombosis, stenosis or obstructions observed.

3.2.2 Prevascularization

Another interesting method involves prevascularization of the tissue prior to or upon implantation. This involves multi-cellular based strategies using fibroblasts and stromal progenitor cells, as well as deliverance of angiogenic growth factor in order to cause branching of microvessles from host vasculature [61,64–67]. Controlled growth factor dosage allows new vessels to form. However, excess amounts of VEGF were found to cause severe vascular leakage [68]. Platelet-derived growth factor (PDGF) is used for the recruitment of smooth muscle cells and pericytes to stabilize the newly formed vessels, while transforming growth factor b (TGF-b) has been shown to be important for the production of extracellular matrix [69]. Along with VEGF, these factors have been found to form a high number of mature vessels in implanted scaffolds [70]. Prevascularization has been successful both *in vitro* [66] and *in vivo* models [71]. For instance, A multicellular culture containing mouse myoblasts, human embryonic stem cells, and human umbilical vein endothelial cells (HUVECs) were seeded onto a porous biodegradable scaffold composed of PLLA and PLGA [66,71]. Following the growth factor delivery described above, an artificial muscle tissue was created with integrated functional vascular networks. After implantation into rat quadriceps and abdominal

muscles, the prevascularized artificial tissue was able anastomose spontaneously to the ingrowing vasculature of the host and supply the construct with nutrients.

3.2.3 Limitations of conventional vascularization techniques

These conventional methods are limited in their versatility and their functionality. They are only suitable for the replacement of small areas of damaged issue – there is a lack of architectural complexity on a larger scale. Conventional grafting techniques only allow replacement of a single vessel as oppose to an entire tissue, while prevascularization does not allow for the precision in feature or cellular patterning that would be necessary to create a functional tissue microenvironment. These limitations are a powerful impetus for exploring new alternatives.

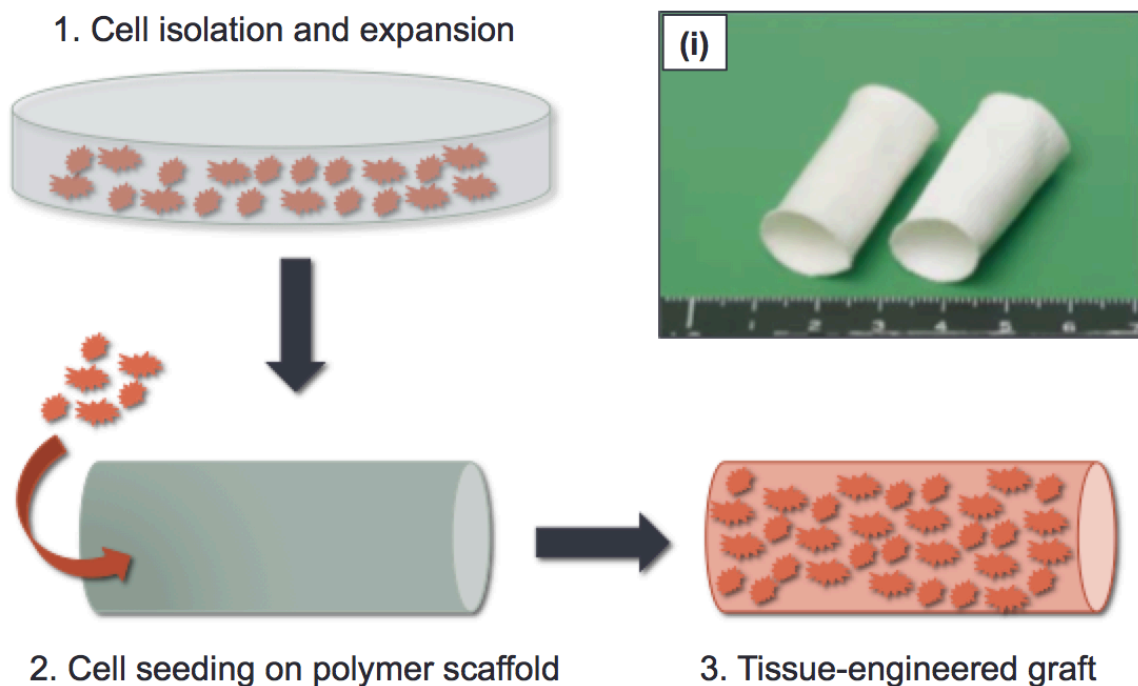


FIG. 1.8: Schematic representation of the conventional method for fabrication of a tissue-engineered vascular graft. i) Example of a tissue engineered vascular grafts composed of fibrous co-polymers, fabricated using ring-opening polymerization [59].

3.3 Unconventional 3D fabrication techniques:

The advantage of using AM techniques for vascular tissue engineering is the ability to create 3D perfusable vessel-like networks within large, bulk artificial tissue constructs. AM strategies allow control in network patterning, dimensions and cellular incorporation. This can be achieved using extrusion-based, non-extrusion based, or hybrid AM methods.

3.3.1 Extrusion-based techniques

There has been particularly significant progress made in this field using extrusion based printing. These techniques can be broadly categorized as inkjet-based printing that involve scaffold-free processes, or as 3D-bioplotting methods such as flow focusing techniques (for fiber/filament printing) and droplet-based printing.

A novel biology-inspired paradigm involving a scaffold-free approach based on printing of cell aggregates known as tissue spheroid extrusion has been used [72–75]. Uniluminal vascular tissue aggregates composed of bovine aortal endothelial cells were printed in close proximity, causing them to fuse to one another within a single layer as well as between successive layers. This would result in the fabrication of branched vascular segments with a single, interconnected hollow center ($\sim 400\mu\text{m}$). Human smooth muscle cells were also printed in this way, thereby allowing them to assemble into ring-like vascular constructs. However, in order to implement tissue spheroid-based bioprinting, it is essential to consider techniques for fabrication of uniformly sized spheroids. These techniques are considerably long and tedious, requiring at least 48 hours of preparation time prior to printing [76].

Other work involves the fabrication of hollow gel tubes using flow focusing extrusion-based methods [77,78], thereby creating cell-laden hollow scaffolds for vascular tissue engineering. Generally this involves the use of concentrically embedded needles that produce a coaxial flow of uncrosslinked polymer and crosslinker agent. One group utilized this technique to print hollow gel fibers ($\geq 500\mu\text{m}$) composed of an alginate/gelatin methacrylate (GelMA) mixture [79–81]. Calcium chloride is used to crosslink the alginate upon extrusion, thereby providing structural stability to the construct. Unlike GelMA, alginate does not provide an ideal environment for cell

adhesion. Therefore, the alginate is removed using chelating agents once the GelMA is solidified via photocrosslinking. This allowed HUVECs to be successfully perfused and seeded within the hollow structures, where their viability was maintained over a period of 14 days. However, the current available co-flow techniques lack scalability in the number of concentric hierarchical gel layers that can be formed surrounding the hollow channels, thereby limiting the degree of architectural and material complexity that can be achieved since only one cell type is generally used.

Branched hollow scaffold fabrication was also achieved using a droplet-based printing technique. Agarose was dispensed into a supporting liquid composed of high buoyant density perfluorocarbons, which prevented the collapse of the structure due to gravity force compensation [82]. FIG. 1.9a shows a branched hollow vessel-like structure that was fabricated using this process. Osteoblastic cells were encapsulated within the gels during printing and were found to grow and form colonies over 7 days. The minimum droplet size achieved was 600 μ m, and hollow structures with a tube diameter of 3.5mm were formed. A similar technique was used to print alginate into calcium (which caused immediate gelation of the droplet upon dispensing) in order to form hollow tubes as well [83]. Once again, the fabricated hollow tube dimensions were in the millimeter scale (~2mm). While these droplet-based printing techniques demonstrate the potential for creating branched hollow structures, they also present severe limitations in achievable feature resolutions due to droplet dispersion during extrusion.

3.3.2 Non-extrusion based techniques

There are several non-extrusion based strategies currently being used for creating perfusable vessel-like channel networks. These techniques broadly fall under laser patterning strategies or planar processing methods.

Laser patterning has been used to create cellularized stackable sheets in order to create 3D constructs [84,85]. One such technique involves using laser induced forward transfer (LIFT) [84]. LIFT is a direct-writing technique in which a laser beam is focused through a transparent support plate onto a precursor thin film of the material to be transferred. A laser pulse promotes the transfer of the thin film material onto a substrate closely placed in parallel. In this work, LIFT is used to print alternating layers of grid-

patterned HUVECs (to resemble a network), followed by stromal cells patterned in between the grids. Layer thickness of $65\mu\text{m}$ was achieved. These tissue-engineered structures were found to form perfusable vascularized tissue constructs, which were implanted into a rat myocardium and found to successfully integrate. Although this process is able to achieve high resolutions and precise cellular patterning, the process is slow and highly time consuming as well as costly. This limits the size and number of layers that can be achieved within the construct.

As previously mentioned, non-extrusion based techniques involving planar processing have also been successfully used for the purpose of microvascular tissue engineering [40,86–88]. For example, one group showed the bonding of alginate and collagen composite layers with another liquid layer of alginate composite precursors using temperature controlled fibrillogenesis, which is the formation of insoluble fibrils due to the assembly of collagen molecules [86]. Hollow channels ($\sim 200\mu\text{m}$) were formed in this way, as seen in FIG. 1.9b, and successfully perfused and seeded with HUVECs over 7 days. This process potentially eliminates the need for cell-harmful conditions, such as high temperatures [87] and chaotropic agents [88] that have sometimes been used for bonding, but it is also very arduous to fabricate multilayer 3D hydrogels in this way. In order for bonding via fibrillogenesis to occur, the gelled hydrogel layer must be precisely placed on the liquid surface, without disrupting it. This can cause potential microstructure blockage and limitations in channel resolution and depth.

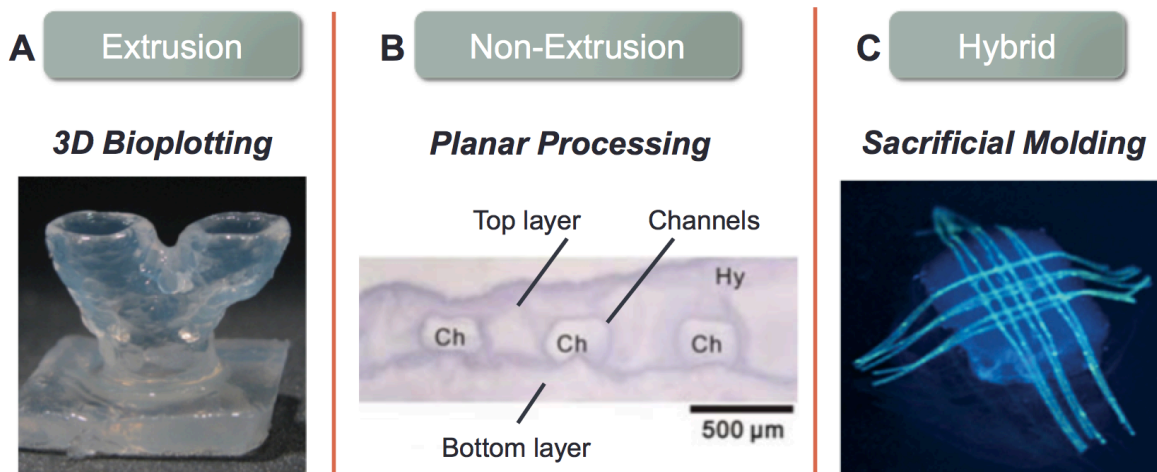


FIG. 1.9: Some of the unconventional tissue engineering strategies currently being used to 3D construct vascular networks include A) 3D bioplotting [82], B) planar processing [86], and C) sacrificial molding [89].

3.3.3 Hybrid techniques

Some groups have developed hybrid techniques involving both printing as well as sacrificial moulding of carbohydrate glasses, agarose gels, or gelatin, as well as bulk hydrogel immersion in a variety of extracellular matrices such as Matrigel, collagen, and fibrin [56,89–93]. Removable spacers have been particularly useful in applications requiring vascular network fabrication. Sacrificial materials were removed by mechanical force, chemical dilution, or thermal response, resulting in hollow channels available for perfusion. For example, solid agarose gel fibers were extrusion printed into a mold and then submerged into a cell-laden hydrogel precursor solution composed of GelMA [89,94], as seen in FIG. 1.9c. Once the surrounding matrix is solidified via photocrosslinking, the agarose fibers are removed under vacuum in order to obtain perfusable hollow channels ($\geq 250\mu\text{m}$). HUVECs are later perfused and successfully seeded into the channels. However, this mechanical removal can sometimes compromise the integrity of the channels [95]. Alternatively, sacrificial materials may be removed by liquification to avoid this problem. For example, gelatin is a thermoresponsive material that is known to solidify at lower temperatures and liquefy at 37°C . One work utilized this phenomenon to print branched gelatin patterns within a collagen matrix [96]. Once the gelatin was liquefied, a hollow channel network ($\sim 1\text{mm}$) was formed. Endothelial cells could easily be seeded on the inner lumen of the channels as collagen provided good cell adhesion properties. However, the weak mechanical properties of these materials caused some deformation of the channels and printed features. The bulk materials used in such cases demonstrate high biocompatibility, but can have the disadvantage of being structurally unstable, making certain printing techniques difficult.

Other researchers have demonstrated the use of multiple AM strategies in order to incorporate vasculature into other types of living tissue, specifically bone [97,98]. In this case, FDM is used in combination with SL in order to create hard material scaffolds embedded cell-laden soft materials. FDM is used to deposit hard PLA fibers to fabricate a bone-like scaffold, while SL is used to pattern cell-laden GelMA hydrogel. The soft and hard materials are deposited in alternating layers, such that the GelMA is embedded throughout the PLA structure, thereby forming interconnected vascular channels. This allows the creation of a highly complex tissue-like construct with architecture similar to

that of native bone. While the use of hybrid systems can allow for versatility in material incorporation required for creating heterogeneous constructs, the use of multiple AM techniques for a single bio-application can become very time consuming and costly.

3.3.4 Limitations of current AM used for vascularization

Each of the various types of AM strategies used for vascular tissue engineering have their respective advantages and disadvantages. Extrusion-based techniques allow for precise placement of cells and materials in a fast, time effective manner. However, many of the current available techniques focus only on creating isolated vessel-like structures, as oppose to fabricating thick 3D constructs with the embedded channel networks integrated into them. Additionally, the achievable feature resolution is significantly lower than that of non-extrusion systems. Although non-extrusion techniques are capable of higher resolutions, the processes require multiple steps that become time consuming. There is also high risk of channel obstruction due to limited lamination or bonding options. Hybrid techniques, while they allow the creation of complex multi-material scaffolds, also have similar drawbacks to non-extrusion systems in that they often require long, tedious and potential disruption of channel structures. Additionally, their feature resolution can be found to be similar to that of extrusion-based systems.

One of the major limitations for existing extrusion, non-extrusion, and hybrid AM vascularization techniques is the inability to create hierarchal concentric layers of various cell types, similar to that found in biological vessel architecture. Some research groups have managed to incorporate both the endothelial and smooth muscle layers within their tissue engineered vessels [59,63,99]. However, the difficulty associated with creating hierarchal structures with concentric layers of varying tissue types has lead the majority of work in the field to focus mainly on the endothelialisation process. With the current available additive manufacturing and printing technologies, this is generally accomplished with cell seeding of inner channel walls. This limits the degree of control over specific and precise cellular placement within various layers.

4. Parameters Impacting AM Fabrication of Vascular-like Networks

When addressing a specific tissue engineering application, an AM technique is selected based on the material and architectural requirements of the tissue to be fabricated. The decision to use a specific AM strategy depends entirely on the bio-application it is intended for. There are only a few of the previously discussed AM techniques that can be considered suitable for use in vascular engineering applications. In order to achieve 3D vascularization using AM, there are a number of factors that need to be considered during the fabrication process. Specifically, material cytocompatibility, mechanical properties, feature resolution, speed, and cost are the main elements to be addressed (FIG. 1.10). These are universal factors that impact all biofabrication applications, and must be considered on a case-by-case basis. However, in this section, these characteristics are discussed in the context of creating perfusable vessel-like structures and integrating them into 3D tissues for vascular tissue engineering.

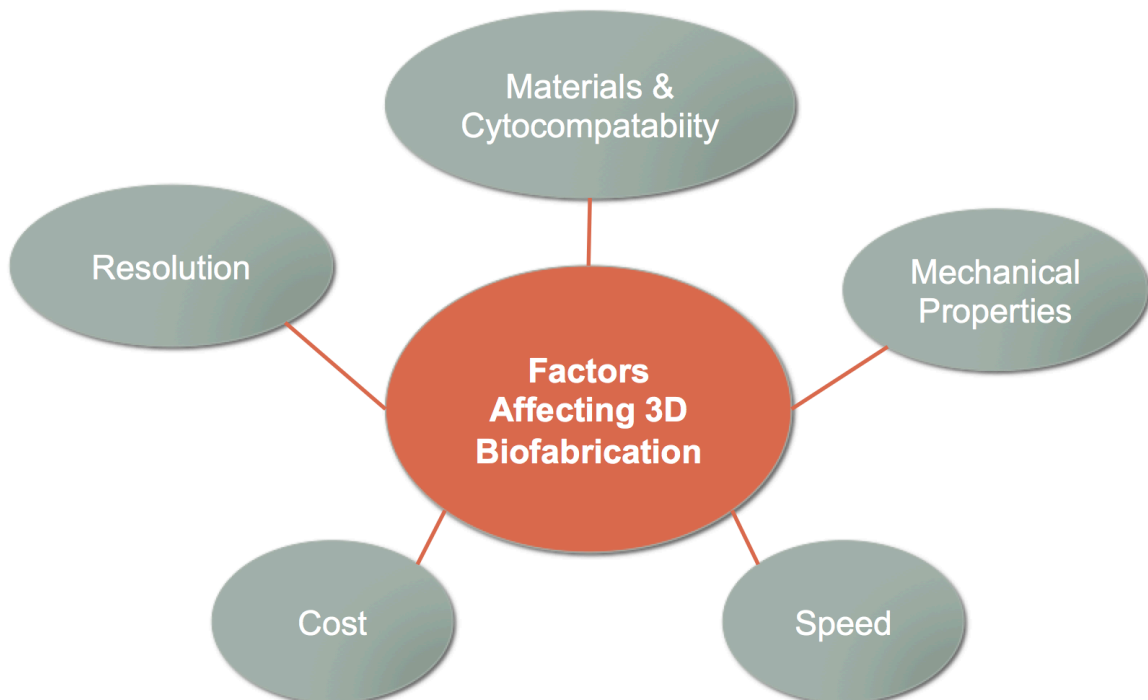


FIG. 1.10: Schematic representation of the various factors affecting 3D fabrication techniques for bioapplications.

4.1 Materials and cytocompatibility:

Although there are a wide variety of hard biomaterials that are readily available for 3D biofabrication techniques, these materials are not suitable for engineering perfusable vessel-like structures and networks. Biological blood vessels are composed of soft ECM and therefore require the use of soft materials, namely hydrogels. This means that only fabrication techniques that can utilize soft materials (e.g. inkjet printing, 3D bioplotting, planar processing, and sacrificial molding) may be used.

Hydrogels are composed of water-swollen polymer networks that can be formed by ionic or covalently crosslinked hydrophilic polymers that do not dissolve in aqueous environments. Hydrogels possess a 3D structure that has been crosslinked either physically or chemically. For example, the ECM of blood vessels is primarily composed of collagen [100], which is soluble in acetic acid but crosslinks and solidifies via pH sensitivity when it is neutralized with sodium hydroxide. These insoluble structures generally exhibit good biocompatibility and high permeability for oxygen and nutrients, making them effective for cell encapsulation or controlled release strategies of active agents and biomolecules. The ability of these gels to swell under biological conditions makes them ideal materials for tissue engineering applications, as they resemble natural soft tissue more than any other polymeric biomaterial [101–104].

Cytocompatibility is a critical parameter in assessing hydrogels. A material that elicits an inflammatory response or otherwise damages cells and leads to significant scarring would be especially problematic. Cell attachment to the ECM is an obvious prerequisite for adequate cell proliferation and migration. Popular natural materials such as collagen, fibrin, and Matrigel provide optimal biological environments for soft tissue engineering. These materials have been widely used for vascularization applications and the study of angiogenesis [107–111]. Endothelial cells readily adhere to the matrix, thereby providing a platform that promotes capillary formation. Developing sprouts anastomose to one another, resulting in a mature network of branching microvessels with patent lumina.

Native ECM provides cell-adhesive sites for binding cell surface receptors, such as integrins and selectins, making them attractive materials for tissue engineering applications. However, hydrogels that do not contain these cell-binding peptides can be

modified with a variety of ECM cell adhesive proteins (CAPs) in order to mimic these required cell-matrix interactions [112,113].

4.2 Mechanical properties:

Vascular tissue engineering requires the formation of hollow channels constructs, so it is important to consider the mechanical strength of the materials used so that the structural integrity of the hollow channels is not compromised. This means that inkjet printing would not be a suitable AM technique to use, since it often requires weak and low viscosity materials. Sacrificial molding by means of mechanical spacer removal can also destroy or contort the structure and embedded features, making it unsuitable for mimicking the complex branched structures.

Mechanical performance of different hydrogels is highly dependant on properties such as elasticity, compressibility, tensile strength, strain, and viscoelastic behaviour. These properties are affected by polymer characteristics, swelling, degradation, and gelling conditions such as temperature and pH levels [114]. For example, the mechanical strength can be increased by increasing the density or concentration of crosslinker agents, or decreased by increasing swelling of the hydrogels. There is an optimal degree of crosslinking, above which the gel will become more brittle and less elastic. High mechanical strength is necessary to maintain structural support and stability, particularly in the case of hollow constructs that are used for vascular tissue engineering.

It is also important to establish a balance between mechanical strength and cellular compatibility. Although low mechanical stiffness results in reduced structural integrity of the construct, it also enables increased migration and proliferation of cells [115]. As previously discussed, collagen and fibrin have been commonly used for vascular tissue engineering. These natural substrates are favourable for cell adhesion and growth. However they demonstrate very weak mechanical properties making handling or printing of these materials increasingly difficult or not possible [116]. They demonstrate a plastic-like response, as is evident by their inability to recover from strain application and therefore lack the strength and elasticity present in native blood vessels [117]. They also have slow gelation rates and fast degradation rates, which can result in rapid loss of supporting matrix during fabrication.

Alternatively, alginate is a hydrogel that is well known for its structural integrity, increased elasticity, and fast gelation rates [118]. However, it requires protein modification for increased cell adhesion. A common approach to design a highly specific adhesive surface is to covalently couple an entire ECM protein or peptide sequences capable of binding to cellular receptors [119,120] to the polymer. Other work has demonstrated the use of synthetic hydrogels such as polyethylene oxide (PEO), poly vinyl alcohol (PVA), and polyethylene glycol (PEG) as a supporting matrix for various tissues due to its highly tunable moduli and reduced inflammatory response [121,122]. However, these materials have low protein affinity is not beneficial for cell adhesion [123]. These materials also generally require photocrosslinking in order to solidify, which can be harmful to integrated cells. Therefore, it appears there exists some level of trade-off between cellular adhesion and compatibility versus mechanical characteristics and the associated structural stability.

4.3 Resolution:

The major advantage of using unconventional 3D fabrication techniques is the ability to achieve precise geometries and high-resolution spacing of features. This is particularly important creating 3D tissues with integrated vascular channels. Vessels must be located within 100–200 μm of blood vessels, which is the diffusion limit for oxygen [124]. The resolution of an AM technique is a consequence several non-machine specific parameters such as material properties and product geometry. Generally, the actual resolution of the fabricated construct is lower than the specified theoretical resolution of the 3D printer.

In general, non-extrusion based AM techniques such as SLS and SL are able to achieve higher resolutions than extrusion based strategies due to their localized small reaction volume. SLS is capable of resolutions of about 60 – 80 μm [125]. The sintering reaction is limited only by the material particle size. SL is also able to achieve high resolutions of about 1-50 μm [124,126]. However, as previously mentioned, UV radiation may be problematic in the case of exposed cells encapsulated within the material. Therefore, these techniques may be used in conjunction with planar processing strategies

(i.e. to create the molds in which cell-laden materials are poured and cast) in order to achieve the necessary resolutions without compromising cell viabilities.

Extrusion-based techniques such as FDM and 3D bioplotting have lower resolutions of around 200-1000 μm [127,128]. However, the actual resolution of features in the end product may decrease further, particularly when printing hydrogels due to material spreading upon deposition onto the substrate. Resolution variation will depend on material gelation rates, crosslinking density, nozzle diameter, and substrate hydrophobicity [129]. Inkjet printing techniques are capable of higher resolutions (100 μm) [21] due to increased control of droplet size, but are subject to limitations in material viscosity as nozzles are more susceptible to clogging.

4.4 Speed:

Non-extrusion based techniques generally require longer fabrication times in comparison to extrusion based methods. This is because the photopolymerization requires slow rastering of the laser, particularly for larger parts [130]. SL and SLS equipment typically operate at writing speed of 200mm/s [131] and 7-48mm/h respectively [125]. Increased feature resolution will also cause scanning speeds to decrease. Additional curing time is often required after fabrication is completed [125]. In the case of planar processing strategies, the manual aspect of removing and stacking the cast polymer layers will also slow down the process further.

In comparison, extrusion-based techniques can operate at much faster speeds. This would be dependant on the speed of the motors controlling printhead movement and material feed rate (e.g. 150mm/s and 300mm/s for EnvisionTec and RepRap 3D printers respectively). The fast and simple, one-step automated deposition process allows for quick and easy fabrication. However, operating at high speeds can cause feature deformation. It is also important to take into account material gelation times. Materials that are pH-sensitive or thermoresponsive (e.g. collagen and Matrigel respectively) require longer periods of time (~30min) in order to completely solidify [116]. However, polymers that are capable of physical crosslinking (such as sodium alginate with calcium chloride) can be gelled almost instantaneously. Fast gelation can also be achieved with photo-curable polymers, but this would require higher concentrations of photoinitiator,

which is toxic to cells. Structure size, feature resolution, and material properties are therefore all critical factors that must be considered when anticipating 3D fabrication speeds.

4.5 Cost:

3D fabrication systems can vary widely in cost (e.g. RepRap ~\$500, Inkredible >\$5000, uPrint SE Plus >\$20,000) and this can be due to a large variety of factors, including resolution, speed, material, and print volume. For example, the uPrint is able to achieve a resolution of <100 μ m, while the RepRap is only capable of a 300 μ m resolution and a significantly smaller build volume. The Inkredible also contains a small build volume, but is capable of printing cells in a sterile and incubated environment with 98% viability on a bench top. Aside from the upfront cost of the system, it is also important to consider the recurring cost of materials to be used. Hydrogels that are composed of native materials are generally the most expensive, with prices ranging from \$5 to \$100/mg (collagen, Matrigel, and fibrinogen cost approximately \$20/mg, \$5-\$10/mg, and \$50-\$100/mg respectively). Non-native matrices such alginate can be purchased at much lower costs (\$0.08/g). It is useful to use low cost materials in combination with extrusion printing techniques, as these methods can be associated with a large amount of material waste due to dead volume. There is also increased amount of material consumption in comparison to non-extrusion techniques as a result of lower feature resolutions. However, these low cost materials lack the biological environment required for cell adhesion, which can only be provided by the proteins present in native ECM. Therefore, there exists a trade-off in cost versus cellular compatibility. Planar processing techniques can be used in such cases to conserve valuable materials by minimizing waste, and thereby maintaining superior cell biocompatibility.

4.6 Summary

Currently, the most significant challenge in the realization of 3D artificial tissue constructs is the lack of an ability to create multi-scale perfusion channels in natural ECMs and gels. Although several research groups have made various attempts to tackle this issue, many of these techniques are either expensive, tedious and time consuming, or cannot achieve precise control over cell and material placement in order to create hierarchal concentric structures. In this section, it has been determined that there are trade-offs that exist between speed and cost vs. resolution, as well as mechanical properties vs. cytocompatibility. Therefore, it is important to take into consideration the governing parameters (as are summarized in FIG. 1.11) discussed above in order to address these limitations when designing an appropriate 3D fabrication technique for vascular tissue engineering.

	Inkjet Printing	FDM	3D Bioplotting	SLS	SL	Planar Processing	Sacrificial Molding
Material	Cells and ECMs (e.g. collagen, fibrin, gelatin)	Biodegradeable thermoplastics (e.g. PCL, PLA, PGA)	Hydrogels (e.g. gelatin, alginate, agarose, collagen, PEG)	Thermoplastics (e.g. PCL, PLA) Metals (e.g. stainless steel, titanium)	Hard materials (e.g. PCL, PLA) Soft Materials (e.g. PEGDA)	Hydrogels (e.g. gelatin, alginate, agarose, collagen, PEG)	Thermo-responsive hydrogels (e.g. gelatin, agarose) Stiffer hydrogels (e.g. PEG, alginate)
Mechanical Strength	Low	High	Moderate	High	Moderate to high	Moderate	Moderate
Resolution	100µm	200µm – 1mm	200µm – 1mm	60 – 80µm	1 – 50µm	100µm	200µm – 1mm
Speed	Moderate: depends on material gelation times	Fast: 150 – 300mm/s	Moderate: depends on material gelation times	Slow: 7 – 48mm/hr	Slow: 200mm/s plus additional curing time	Slow: multistep processes	Slow: multistep processes
Cost	Moderate	Low	Moderate	High	Low	Moderate	Moderate
Suitability for Vascular Engineering	Yes	No: can be used as removable spacers in sacrificial molding	Yes	No: can be used for mold fabrication in planar processing	No: can be used for mold fabrication in planar processing	Yes	Yes

FIG. 1.11: Table summarizing the various governing parameters that impact each specific AM technique and its suitability for vascular tissue engineering applications.

5. Research Objectives and Aims

The principal aim of this thesis is to utilize AM technology in order to achieve 3D fabrication of soft material scaffolding structures for vascular tissue engineering applications in a fast, simple, and cost-effective manner. The objectives of this work can be classified into two parts: A) extrusion-based and B) non-extrusion based 3D hollow channel network fabrication. As such, the goals of part A and B are as follows:

Part A:

- i. Fabrication of a custom microfluidic nozzle for simple, fast coaxial extrusion and 3D printing of cell-laden hollow alginate tubes that are easily perfusable, using a low-cost, open source 3D printer.
- ii. Multi-axial extrusion and 3D patterning of cell-laden bi- and tri-layered heterogeneous hollow gel structures using scalable microfluidic nozzle in order to maintain structural integrity and improve cell adhesion and viability.

Part B:

- i. 3D fabrication of high-resolution hollow channel networks embedded in thick, multi-layered hydrogel structures using nanoparticle lamination-based planar processing techniques.

6. Thesis Organization

This thesis is comprised of 5 chapters in a “sandwich” thesis format. Chapter 1 and Chapter 5 encompass relevant introductory and concluding information respectively. Part A of the objectives is addressed in Chapter 2 and 3, which discuss extrusion-based 3D printing methodologies used to create hollow hydrogel scaffolding for vascular bioapplications. Part B of the objectives is addressed in Chapter 4, which focuses on non-extrusion based planar processing strategies. Chapters 2,3 and 4 consist entirely of journal articles that are either published or in preparation for submission.

Chapter 1 – This chapter reviews relevant introductory and background information with respect to additive manufacturing and tissue engineering of vascular networks. The motivation behind this type of work is thoroughly discussed and current conventional tissue engineering approaches are presented. Various AM technologies used for bioapplications, both extrusion and non-extrusion based, are described and assessed in terms of pros and cons. Challenges relating to the use of these techniques for vascular engineering are examined, including material cytocompatibility, mechanical properties, resolution, cost, and speed. The current conventional and unconventional approaches used for 3D fabrication of artificial vasculature are also investigated.

Chapter 2 – This chapter describes a method for fabrication of gel layers with interspaced hollow tubes directly on dry substrates in precise geometries using a custom built 3D printer with a microfluidic nozzle. This system is able to construct multi-layered structures with precise control of tube position, spacing, and diameter. These factors can be simultaneously manipulated during printing in order to create a single gel structure with variable architecture. The hollow tubes are immediately perfusable and could serve as vascular networks for tissue engineering applications. The interiors of scaffold-engineered tissue grafts are usually associated with poor nutrient diffusion. Perfusion of these embedded channels allows the required nutrients to reach cells in the bulk region of the construct, thus increasing cell viability.

Chapter 3 – This chapter expands on the work done in Chapter 2. The custom-made microfluidic nozzle is modified in order to allow for scalability in extruding multiple concentric flows. The method described in the previous chapter was capable only of creating homogeneous hollow gel structures, and presented issues with longterm endothelialisation. However, the modified nozzle in this chapter can produce multi-axial flows in order to 3D print and pattern bi- and tri-layered hollow channel structures. This allows for versatility in material incorporation in order to create heterogeneous structures. Different cell types and various cell-friendly materials can be printed in distinct concentric layers, thereby increasing cell adhesion and viability.

Chapter 4 - This chapter describes the use of nanoparticles as adhesives to bond composite collagen containing hydrogel films. For the first time, silicon carbide (SiC) is used as an adhesive and is found to establish strong bonding, as well as creating embedded hollow channels. It was found to enable strong, successful bonding of alginate-collagen media-based gels in comparison to control samples without any adhesive deposited between layers. Similarly, nanosilica was also found to achieve successful bonding with these samples. However, while SiC maintained good cytocompatibility, nanosilica on the other hand was found to reduce cell viability significantly. Therefore, SiC was used to create high-resolution channels embedded within thick, multilayered structures that were easily perfusable. Nanosilica was found to effectively bond plastic PVC tubing to hydrogels and therefore used in creation of interconnects for straight-forward perfusion of the entire construct. This allowed for the creation large, thick structures with integrated, high-resolution networks that would provide a means of nutrient and waste transport for embedded cells.

Chapter 5 – This chapter summarizes the work achieved in this thesis and the relevance to current challenges in the vascular tissue engineering field. The presented work demonstrates the use of 3D fabrication methods in order to engineer tissue constructs with embedded vascular networks. This work is able to overcome many of the challenges previously experienced using available techniques. The co-flow extrusion-based methods allowed for the use a low-cost, easily accessible system that provided precise positioning and patterning at high speeds. The hollow gel constructs were able to maintain their structural integrity due to the strong mechanical properties of the material used. The non-extrusion based lamination strategy allowed for creation of much higher feature resolution, while minimizing material waste. All approaches were versatile and scalable, and allow for the incorporation of various soft materials with good cytocompatibility for a well-maintained multi-cellular system. This chapter also includes recommendations for future work and alternative applications.

7. Contributions

Contributions of this thesis involve novel and innovative methods for hollow channel 3D scaffold fabrication. New methods were designed to do this using both extrusion-based and non-extrusion techniques.

In the case of the extrusion based printing system, a new microfluidic printhead capable of co-flow extrusion in order to create hydrogel structures with embedded perfusable hollow channels was designed and developed. The printing system was characterized in order to identify the operational range. This operational range was characterized in terms of two factors: flow rates, printhead speeds, and material properties. This process was optimized in order to determine the ideal printing range for achieving precise patterning of conduits. Flow rates and printhead speeds were also varied in order to assess the range of possible hollow channel and gel layer dimensions that could be achieved within the structure. The easy and straightforward perfusability of the hollow channel networks was demonstrated, thereby allowing us to achieve higher cell viabilities in comparison to bulk, “non-vascularized” constructs.

Additionally, the scalable custom nozzle was further modified in order to allow for multiple concentric flows, thereby allowing us to incorporate multiple materials simultaneously during printing. Different cell types were successfully seeded in distinct, hierarchal layers thereby demonstrating increased control over spatial and structural complexity. It also allowed hollow channel structures to be created with increased cell adhesion properties, without compromising the structural integrity or stability of the constructs. This custom microfluidic printhead allows for a 3D printing process that is fast, automated, and scalable, unlike the other currently available techniques. This method also allows versatility in material incorporation, such that more cell-friendly materials can be used without compromising the construct’s mechanical properties.

For our non-extrusion planar AM strategy, a new inorganic adhesive suitable was identified for bonding of collagen-based hydrogel layers in order to create 3D constructs with perfusable, high resolution channel networks. Mechanical tests were performed in order to determine optimum bond strengths in terms of adhesive concentration, time, and material type. Flow pressure tests were also performed and type of bond failure was

assessed for each of these conditions. These characterizations established the optimum parameters required to proceed with the biological applications. With this planar processing method, strong, sustainable bonding was achieved with high-resolution spacing and fine channel dimensions simply by using nanoparticle lamination. In this way, large thick multi-layered structures were created with embedded perfusable vascular-like networks. The nanoparticles are shown to achieve high bond strengths similar to those achieved with other tissue glues, but without obstructing any of the channel pathways. This is a novel use for SiC nanoparticles and has promising potential for engineering of several tissue types. This work shows that these nanoparticles do not impede flow in any of the channel networks and do not demonstrate any negative or toxic effects on the embedded cells. There exists a wide range of bioapplications that may benefit from utilizing the systems and strategies developed in this thesis, including tissue replacement, drug discovery platforms, and 3D physiological studies.

The following is a list of publications that have contributed to Chapters 2-4. They consist of one published journal article, one journal article that has been accepted to *Advanced Healthcare Materials*, and one that is in preparation for submission. These papers are listed below.

1. Rana Attalla, Celine Ling and Ponnambalam R Selvaganapathy. ***“Fabrication and characterization of gels with integrated channels using 3D printing with microfluidic nozzle for tissue engineering applications.”*** *Biomedical Microdevices* 18.1 (2016): p.17.
2. Rana Attalla, Erin Puersten and Ponnambalam R Selvaganapathy. ***“3D Bioprinting of Heterogeneous Bi- and Tri-layered Hollow Structures inside Gel Layers using Multi-Axial Microfluidic Extrusion Nozzle.”*** This paper is in preparation for submission.
3. Rana Attalla, Celine Ling and Ponnambalam R Selvaganapathy. ***“Silicon carbide nanoparticles as an effective bioadhesive to bond collagen containing composite gel layers for tissue engineering applications.”*** *Advanced Healthcare Materials* 7.5 (2018)

8. Note to the Reader

There is some overlap that exists in the material preparation and methodology sections of Chapters 2 to 4, as this thesis is written in sandwich format.

Images in Chapter 1 that are reused from other works have been adapted with permission. Chapter 2 is published with permission from Biomedical Microdevices, 2016.

References

- [1] “Organ Donation Statistics: Why be an Organ Donor?,” *U.S. Government Information on Organ Donation and Transplantation*, 2017. [Online]. Available: <https://www.organdonor.gov/statistics-stories/statistics.html>.
- [2] “Organ Donations Fall Short of Meeting Demand.,” *Canadian Institute for Health Information*, 2016. .
- [3] L. Pan, Y. Ren, F. Cui, and Q. Xu, “Viability and differentiation of neural precursors on hyaluronic acid hydrogel scaffold,” *J. Neurosci. Res.*, vol. 87, no. 14, pp. 3207–3220, 2009.
- [4] G. Matsumura, S. Miyagawa-Tomita, T. Shin’Oka, Y. Ikada, and H. Kurosawa, “First evidence that bone marrow cells contribute to the construction of tissue-engineered vascular autografts in vivo,” *Circulation*, vol. 108, no. 14, pp. 1729–1734, 2003.
- [5] B. Subramanian, D. Rudym, C. Cannizzaro, R. Perrone, J. Zhou, and D. L. Kaplan, “Tissue-engineered three-dimensional in vitro models for normal and diseased kidney.,” *Tissue Eng. Part A*, vol. 16, no. 9, pp. 2821–2831, 2010.
- [6] A. Atala, S. B. Bauer, S. Soker, J. J. Yoo, and A. B. Retik, “Tissue-engineered autologous bladders for patients needing cystoplasty,” *Lancet*, vol. 367, no. 9518, pp. 1241–1246, 2006.
- [7] W. Bonfield, “Composites for bone replacement,” *J. Biomed. Eng.*, vol. 10, no. 6, pp. 522–526, 1988.
- [8] J. Mansbridge, “Skin tissue engineering,” *Biomater. Sci.*, vol. 19, no. 8, pp. 955–968, 2008.
- [9] S. Baiguera *et al.*, “Tissue engineered human tracheas for in vivo implantation,” *Biomaterials*, vol. 31, no. 34, pp. 8931–8938, 2010.
- [10] M. J. Elliott *et al.*, “Stem-cell-based, tissue engineered tracheal replacement in a child: A 2-year follow-up study,” *Lancet*, vol. 380, no. 9846, pp. 994–1000, 2012.
- [11] H. C. Ott *et al.*, “Perfusion-decellularized matrix: Using nature’s platform to engineer a bioartificial heart,” *Nat. Med.*, vol. 14, no. 2, pp. 213–221, 2008.
- [12] S. N. Bhatia and D. E. Ingber, “Microfluidic organs-on-chips,” *Nat. Biotechnol.*, vol. 32, no. 8, pp. 760–772, 2014.
- [13] M. E. Kolewe, H. Park, C. Gray, X. Ye, R. Langer, and L. E. Freed, “3D structural patterns in scalable, elastomeric scaffolds guide engineered tissue architecture,” *Adv. Mater.*, vol. 25, no. 32, pp. 4459–4465, 2013.
- [14] W. H. Fissell and S. Roy, “The implantable artificial kidney,” *Semin. Dial.*, vol. 22, no. 6, pp. 665–670, 2009.
- [15] W. H. Fissell, A. Dubnisheva, A. N. Eldridge, A. J. Fleischman, A. L. Zydney, and S. Roy, “High-performance silicon nanopore hemofiltration membranes,” *J. Memb. Sci.*, vol. 326, no. 1, pp. 58–63, 2009.
- [16] D. W. Hutmacher, M. Sittinger, and M. V. Risbud, “Scaffold-based tissue engineering: Rationale for computer-aided design and solid free-form fabrication systems,” *Trends Biotechnol.*, vol. 22, no. 7, pp. 354–362, 2004.
- [17] D. L. D. Bourell, J. J. Beaman, M. C. Leu, and D. W. Rosen, “A brief history of additive manufacturing and the 2009 roadmap for additive manufacturing: looking back and looking ahead,” *US-Turkey Work.*, no. 2, pp. 2005–2005, 2009.

- [18] A. van Wijk and I. van Wijk, *3D Printing with biomaterials, Towards a sustainable and circular economy*. 2015.
- [19] T. Wohlers and T. Gornet, “History of additive manufacturing Introduction of non-SL systems Introduction of low-cost 3D printers,” *Wohlers Rep. 2012*, pp. 1–23, 2012.
- [20] F. Oberpenning, J. Meng, J. J. Yoo, and A. Atala, “De novo reconstitution of a functional mamilian urinary bladder by tissue engineering,” *Nat. Biotechnol.*, pp. 144–155, 1999.
- [21] M. Nakamura *et al.*, “Biocompatible Inkjet Printing Technique for Designed Seeding of Individual Living Cells,” *Tissue Eng.*, vol. 11, no. 11–12, pp. 1658–1666, 2005.
- [22] T. Boland, T. Xu, B. Damon, and X. Cui, “Application of inkjet printing to tissue engineering,” *Biotechnol. J.*, vol. 1, no. 9, pp. 910–917, 2006.
- [23] A. Skardal *et al.*, “Bioprinted amniotic fluid-derived stem cells accelerate healing of large skin wounds,” *Stem Cells Transl. Med.*, vol. 1, no. 11, pp. 792–802, 2012.
- [24] T. Cao, K.-H. Ho, and S.-H. Teoh, “Scaffold Design and in Vitro Study of Osteochondral Coculture in a Three-Dimensional Porous Polycaprolactone Scaffold Fabricated by Fused Deposition Modeling,” *Tissue Eng.*, vol. 9, no. 1, pp. 103–112, 2004.
- [25] I. Zein, W. Hutmacher, K. Tan, and S. Teoh, “Fused Deposition Modeling of Novel Scaffold Architectures for Tissue Engineering Applications,” *Biomaterials*, vol. 23, pp. 1169–1185, 2002.
- [26] S. Bose, S. J. Kalita, H. L. Hosick, and A. Bandyopadhyay, “Development of controlled porosity polymer-ceramic composite scaffolds via fused deposition modeling,” *Mater. Sci. Eng. C*, vol. 23, no. 5, p. 611, 2003.
- [27] X. Liu and P. X. Ma, “Polymeric scaffolds for bone tissue engineering,” *Ann. Biomed. Eng.*, vol. 32, no. 3, pp. 477–486, 2004.
- [28] B. C. Tellis, J. A. Szivek, C. L. Bliss, D. S. Margolis, R. K. Vaidyanathan, and P. Calvert, “Trabecular scaffolds created using micro CT guided fused deposition modeling,” *Mater. Sci. Eng. C*, vol. 28, no. 1, pp. 171–178, 2009.
- [29] H. J. Yen, C. S. Tseng, S. H. Hsu, and C. L. Tsai, “Evaluation of chondrocyte growth in the highly porous scaffolds made by fused deposition manufacturing (FDM) filled with type II collagen,” *Biomed. Microdevices*, vol. 11, no. 3, pp. 615–624, 2009.
- [30] a Pfister, R. Landers, a Laib, and R. Schmelzeisen, “Biofunctional rapid prototyping for tissue engineering applications: 3D biplotting versus 3D printing,” *J. Polym. Sci. Part A Polym. Chem.*, vol. 42, no. 3, pp. 624–638, 2003.
- [31] R. Landers, U. Hübner, R. Schmelzeisen, and R. Mülhaupt, “Rapid prototyping of scaffolds derived from thermoreversible hydrogels and tailored for applications in tissue engineering,” *Biomaterials*, vol. 23, no. 23, pp. 4437–4447, 2002.
- [32] M. S. Mannoor *et al.*, “3D printed bionic ears,” *Nano Lett.*, vol. 13, no. 6, pp. 2634–2639, 2013.
- [33] J. M. Williams *et al.*, “Bone tissue engineering using polycaprolactone scaffolds fabricated via selective laser sintering,” *Biomaterials*, vol. 26, no. 23, pp. 4817–4827, 2005.
- [34] B. Partee, S. J. Hollister, and S. Das, “Selective Laser Sintering Process

- Optimization for Layered Manufacturing of CAPA[®] 6501 Polycaprolactone Bone Tissue Engineering Scaffolds,” *J. Manuf. Sci. Eng.*, vol. 128, no. 2, p. 531, 2006.
- [35] T. Traini, C. Mangano, R. L. Sammons, F. Mangano, A. Macchi, and A. Piattelli, “Direct laser metal sintering as a new approach to fabrication of an isoelastic functionally graded material for manufacture of porous titanium dental implants,” *Dent. Mater.*, vol. 24, no. 11, pp. 1525–1533, 2008.
- [36] I. V. Shishkovsky, L. T. Volova, M. V. Kuznetsov, Y. G. Morozov, and I. P. Parkin, “Porous biocompatible implants and tissue scaffolds synthesized by selective laser sintering from Ti and NiTi,” *J. Mater. Chem.*, vol. 18, no. 12, p. 1309, 2008.
- [37] K. W. Lee, S. Wang, B. C. Fox, E. L. Ritman, M. J. Yaszemski, and L. Lu, “Poly(propylene fumarate) bone tissue engineering scaffold fabrication using stereolithography: Effects of resin formulations and laser parameters,” *Biomacromolecules*, vol. 8, no. 4, pp. 1077–1084, 2007.
- [38] S. . Hollister, “Porous Scaffold Design for Tissue Engineering,” *Nat. Mater.*, vol. 4, no. July, pp. 518–524, 2005.
- [39] E. Saiz, L. Gremillard, G. Menendez, P. Miranda, K. Gryn, and A. P. Tomsia, “Preparation of porous hydroxyapatite scaffolds,” *Mater. Sci. Eng. C*, vol. 27, no. 3, pp. 546–550, 2007.
- [40] F. P. W. Melchels, M. Villagomez, D. Lacroix, J. A. Planell, D. W. Grijpma, and J. Feijen, “Designed tissue engineering scaffolds prepared by stereolithography,” *21st Eur. Soc. Biomater. Conf.*, 2007.
- [41] V. A. Liu and S. N. Bhatia, “Hybrid Bio / Artificial Microdevices : Three-Dimensional Photopatterning of Hydrogels Containing Living Cells,” *Biomed. Microdevices*, vol. 4, pp. 257–266, 2002.
- [42] V. L. Tsang *et al.*, “Fabrication of 3D hepatic tissues by additive photopatterning of cellular hydrogels,” *FASEB J.*, vol. 21, no. 3, pp. 790–801, 2007.
- [43] K. Arcaute, B. K. Mann, and R. B. Wicker, “Stereolithography of three-dimensional bioactive poly(ethylene glycol) constructs with encapsulated cells,” *Ann. Biomed. Eng.*, vol. 34, no. 9, pp. 1429–1441, 2006.
- [44] B. Dhariwala, E. Hunt, T. Boland, and D. Ph, “Rapid Prototyping of Tissue-Engineering Constructs , Using Photopolymerizable Hydrogels and Stereolithography,” *Tissue Eng.*, vol. 10, no. 9, pp. 1316–1322, 2004.
- [45] W. Koh, A. Der Revzin, and V. P, “Poly(ethylene glycol) Hydrogel Microstructures Encapsulating Living Cells,” *Langmuir*, vol. 18, no. 22, pp. 2459–2462, 2002.
- [46] Z. Wang, R. Abdulla, B. Parker, R. Samanipour, S. Ghosh, and K. Kim, “A simple and high-resolution stereolithography-based 3D bioprinting system using visible light crosslinkable bioinks,” *Biofabrication*, vol. 7, no. 4, p. 45009, 2015.
- [47] M. Radisic, A. Marsano, R. Maidhof, Y. Wang, and G. Vunjak-Novakovic, “Cardiac Tissue Engineering using perfusion bioreactor systems,” *Nat. Protoc.*, vol. 3, no. 4, pp. 719–738, 2008.
- [48] H. Aubin *et al.*, “Directed 3D cell alignment and elongation in microengineered hydrogels,” *Biomaterials*, vol. 31, no. 27, pp. 6941–6951, 2010.
- [49] Y. Zheng *et al.*, “In vitro microvessels for the study of angiogenesis and

- thrombosis,” *Proc. Natl. Acad. Sci.*, vol. 109, no. 24, pp. 9342–9347, 2012.
- [50] S. Raghavan, C. M. Nelson, J. D. Baranski, E. Lim, and C. S. Chen, “Geometrically Controlled Endothelial Tubulogenesis in Micropatterned Gels,” *Tissue Eng. Part A*, vol. 16, no. 7, pp. 2255–2263, 2010.
- [51] J. W. Nichol, S. T. Koshy, H. Bae, C. M. Hwang, S. Yamanlar, and A. Khademhosseini, “Cell-laden microengineered gelatin methacrylate hydrogels,” *Biomaterials*, vol. 31, no. 21, pp. 5536–5544, 2010.
- [52] T. Xu *et al.*, “Hybrid printing of mechanically and biologically improved constructs for cartilage tissue engineering applications,” *Biofabrication*, vol. 5, no. 1, p. 15001, 2013.
- [53] G. Huang, S. Wang, X. He, X. Zhang, T. J. Lu, and F. Xu, “Helical spring template fabrication of cell-laden microfluidic hydrogels for tissue engineering,” *Biotechnol. Bioeng.*, vol. 110, no. 3, pp. 980–989, 2013.
- [54] P. O. Bagnaninchi, Y. Yang, N. Zghoul, N. Maffulli, R. K. Wang, and A. J. El Haj, “Chitosan Microchannel Scaffolds for Tendon Tissue Engineering Characterized Using Optical Coherence Tomography,” *Tissue Eng.*, vol. 13, no. 2, pp. 323–331, 2007.
- [55] M. J. Moore *et al.*, “Multiple-channel scaffolds to promote spinal cord axon regeneration,” *Biomaterials*, vol. 27, no. 3, pp. 419–429, 2006.
- [56] J. S. Miller *et al.*, “Rapid casting of patterned vascular networks for perfusable engineered three-dimensional tissues,” *Nat. Mater.*, vol. 11, no. 9, pp. 768–774, 2012.
- [57] M. Salmi *et al.*, “Patient-specific reconstruction with 3D modeling and DMLS additive manufacturing,” *Rapid Prototyp. J.*, vol. 18, no. 3, pp. 209–214, 2012.
- [58] H. Bae *et al.*, “Building vascular networks,” *Sci. Transl. Med.*, vol. 4, no. 160, p. 160ps23, 2012.
- [59] T. Shin’oka *et al.*, “Midterm clinical result of tissue-engineered vascular autografts seeded with autologous bone marrow cells,” *J. Thorac. Cardiovasc. Surg.*, vol. 129, no. 6, 2005.
- [60] T. J. Poole and J. D. Coffin, “Vasculogenesis and angiogenesis: two distinct morphogenetic mechanisms establish embryonic vascular pattern,” *Journal Exp. Zool. Part A Ecol. Genet. Physiol.*, vol. 251, no. 2, pp. 224–231, 1989.
- [61] K. K. Hirschi, T. C. Skalak, S. M. Peirce, and C. . Little, “Vascular assembly in natural and engineered tissues,” *Ann. N. Y. Acad. Sci.*, vol. 961, no. 1, pp. 223–242, 2002.
- [62] Y. Gao, “Architecture of the Blood Vessels,” in *Biology of Vascular Smooth Muscle: Vasoconstriction and Dilatation*, Singapore: Springer, 2017, pp. 3–12.
- [63] T. Shin’oka, Y. Imai, and Y. Ikada, “Transplantation of a tissue-engineered pulmonary artery,” *N. Engl. J. Med.*, vol. 344, no. 7, pp. 532–533, 2001.
- [64] T. P. Richardson, M. C. Peters, A. B. Ennett, and D. J. Mooney, “Polymeric system for dual growth factor delivery,” *Nat. Biotechnol.*, vol. 19, no. November, pp. 1029–1034, 2001.
- [65] M. Using *et al.*, “Engineering of Vascularized Transplantable Bone Tissues : Induction of Axial Vascularization in an Osteoconductive Matrix using an Arteriovenous Loop,” *Tissue Eng.*, vol. 12, no. 7, pp. 1721–1731, 2006.
- [66] O. Caspi *et al.*, “Tissue engineering of vascularized cardiac muscle from human

- embryonic stem cells,” *Circ. Res.*, vol. 100, no. 2, pp. 263–272, 2007.
- [67] J. M. Kelm *et al.*, “Tissue-transplant fusion and vascularization of myocardial microtissues and macrotissues implanted into chicken embryos and rats,” *Tissue Eng.*, vol. 12, no. 9, pp. 2541–2553, 2006.
- [68] A. H. Zisch, M. P. Lutolf, and J. A. Hubbell, “Biopolymeric delivery matrices for angiogenic growth factors,” *Cardiovasc. Pathol.*, vol. 12, no. 6, pp. 295–310, 2003.
- [69] P. Carmeliet, “Mechanisms of angiogenesis and arteriogenesis,” *Nat. Med.*, vol. 6, no. 4, pp. 389–395, 2000.
- [70] R. R. Chen, E. A. Silva, W. W. Yuen, and D. J. Mooney, “Spatio-temporal VEGF and PDGF delivery patterns blood vessel formation and maturation,” *Pharm. Res.*, vol. 24, no. 2, pp. 258–264, 2007.
- [71] S. Levenberg *et al.*, “Engineering vascularized skeletal muscle tissue,” *Nat. Biotechnol.*, vol. 23, no. 7, pp. 879–884, 2005.
- [72] V. Mironov, R. P. Visconti, V. Kasyanov, G. Forgacs, C. J. Drake, and R. R. Markwald, “Organ printing: Tissue spheroids as building blocks,” *Biomaterials*, vol. 30, no. 12, pp. 2164–2174, 2009.
- [73] K. Jakab *et al.*, “Tissue engineering by self-assembly of cells printed into topologically defined structures,” *Tissue Eng. Part A*, vol. 14, no. 3, pp. 413–421, 2008.
- [74] T. Boland, V. Mironov, A. Gutowska, E. a Roth, and R. R. Markwald, “Cell and organ printing 2: fusion of cell aggregates in three-dimensional gels,” *Anat. Rec. A. Discov. Mol. Cell. Evol. Biol.*, vol. 272, no. 2, pp. 497–502, 2003.
- [75] K. Jakab, B. Damon, A. Neagu, A. Kachurin, and G. Forgacs, “Three-dimensional tissue constructs built by bioprinting,” *Biorheology*, vol. 43, no. 3–4, pp. 509–513, 2006.
- [76] A. N. Mehesz *et al.*, “Scalable robotic biofabrication of tissue spheroids,” *Biofabrication*, vol. 3, no. 2, 2011.
- [77] K. H. Lee, S. J. Shin, Y. Park, and S. Lee, “Synthesis of Cell-Laden Alginate Hollow Fibers Using Microfluidic Chips and Microvascularized Tissue-Engineering Applications **,” *Small*, vol. 5, no. 11, pp. 1264–1268, 2009.
- [78] L. Leng, A. McAllister, B. Zhang, M. Radisic, and A. Günther, “Mosaic hydrogels: One-step formation of multiscale soft materials,” *Adv. Mater.*, vol. 24, no. 27, pp. 3650–3658, 2012.
- [79] W. Liu *et al.*, “Coaxial extrusion bioprinting of 3D microfibrinous constructs with cell-favorable gelatin methacryloyl microenvironments,” *Biofabrication*, 2017.
- [80] W. Jia *et al.*, “Direct 3D bioprinting of perfusable vascular constructs using a blend bioink,” *Biomaterials*, vol. 106, pp. 58–68, 2016.
- [81] Y. S. Zhang *et al.*, “Bioprinting 3D microfibrinous scaffolds for engineering endothelialized myocardium and heart-on-a-chip,” *Biomaterials*, vol. 110, pp. 45–59, 2016.
- [82] A. Blaeser *et al.*, “Biofabrication Under Fluorocarbon: A Novel Freeform Fabrication Technique to Generate High Aspect Ratio Tissue-Engineered Constructs,” *Biores. Open Access*, vol. 2, no. 5, pp. 374–384, 2013.
- [83] C. Xu, K. Christensen, Z. Zhang, Y. Huang, J. Fu, and R. R. Markwald, “Predictive compensation-enabled horizontal inkjet printing of alginate tubular

- constructs,” *Manuf. Lett.*, vol. 1, no. 1, pp. 28–32, 2013.
- [84] R. Gaebel *et al.*, “Patterning human stem cells and endothelial cells with laser printing for cardiac regeneration,” *Biomaterials*, vol. 32, no. 35, pp. 9218–9230, 2011.
- [85] A. Ovsianikov *et al.*, “Laser printing of cells into 3D scaffolds,” *Biofabrication*, vol. 2, no. 1, 2010.
- [86] X. Mu, W. Zheng, L. Xiao, W. Zhang, and X. Jiang, “Engineering a 3D vascular network in hydrogel for mimicking a nephron,” *Lab Chip*, vol. 13, no. 8, pp. 1612–1618, 2013.
- [87] Y. Ling *et al.*, “A cell-laden microfluidic hydrogel,” *Lab Chip*, vol. 7, no. 6, pp. 756–762, 2007.
- [88] J. P. Gleghorn, C. S. D. Lee, M. Cabodi, A. D. Stroock, and L. J. Bonassar, “Adhesive properties of laminated alginate gels for tissue engineering of layered structures,” *J. Biomed. Mater. Res. - Part A*, vol. 85, no. 3, pp. 611–618, 2008.
- [89] L. E. Bertassoni *et al.*, “Hydrogel bioprinted microchannel networks for vascularization of tissue engineering constructs,” *Lab Chip*, vol. 14, no. 13, pp. 2202–11, 2014.
- [90] W. Lee *et al.*, “On-demand three-dimensional freeform fabrication of multi-layered hydrogel scaffold with fluidic channels,” *Biotechnol. Bioeng.*, vol. 105, no. 6, pp. 1178–1186, 2010.
- [91] L. E. Bertassoni *et al.*, “Direct-write bioprinting of cell-laden methacrylated gelatin hydrogels,” *Biofabrication*, vol. 6, no. 2, 2014.
- [92] G. Villar, A. D. Graham, and H. Bayley, “A Tissue-Like Printed Material,” *Science (80-.)*, vol. 340, no. 6128, pp. 48–52, 2013.
- [93] C. J. Hansen *et al.*, “High-throughput printing via microvascular multinozzle arrays,” *Adv. Mater.*, vol. 25, no. 1, pp. 96–102, 2013.
- [94] S. Massa *et al.*, “Bioprinted 3D vascularized tissue model for drug toxicity analysis,” *Biomicrofluidics*, vol. 11, no. 4, 2017.
- [95] Y. S. Zhang *et al.*, “3D Bioprinting for Tissue and Organ Fabrication,” *Ann. Biomed. Eng.*, vol. 45, no. 1, pp. 148–163, 2017.
- [96] V. K. Lee *et al.*, “Creating perfused functional vascular channels using 3D bioprinting technology,” *Biomaterials*, vol. 35, no. 28, pp. 8092–8102, 2014.
- [97] B. Byambaa *et al.*, “Bioprinted Osteogenic and Vasculogenic Patterns for Engineering 3D Bone Tissue,” *Adv. Healthc. Mater.*, 2017.
- [98] H. Cui, W. Zhu, M. Nowicki, X. Zhou, A. Khademhosseini, and L. G. Zhang, “Hierarchical Fabrication of Engineered Vascularized Bone Biphasic Constructs via Dual 3D Bioprinting: Integrating Regional Bioactive Factors into Architectural Design,” *Adv. Healthc. Mater.*, vol. 4, no. 1, pp. 139–148, 2014.
- [99] Y. Gafni *et al.*, “Design of a filamentous polymeric scaffold for in vivo guided angiogenesis,” *Tissue Eng.*, vol. 12, no. 11, pp. 3021–3034, 2006.
- [100] J. A. Eble and S. Niland, “The extracellular matrix of blood vessels,” *Curr Pharm Des*, vol. 15, no. 12, pp. 1385–1400, 2009.
- [101] J. Kopeček, “Hydrogel biomaterials: A smart future?,” *Biomaterials*, vol. 28, no. 34, pp. 5185–5192, 2007.
- [102] M. P. Lutolf, “Biomaterials: Spotlight on hydrogels,” *Nat. Mater.*, vol. 8, no. 6, pp. 61–86, 2007.

- [103] Rein V. Ulijn *et al.*, “Bioresponsive hydrogels,” *Mater. Today*, vol. 10, no. 4, pp. 40–48, 2007.
- [104] J. Lee, M. J. Cuddihy, and N. A. Kotov, “Three-Dimensional Cell Culture Matrices: State of the Art,” *Tissue Eng. Part B Rev.*, vol. 14, no. 1, pp. 61–86, 2008.
- [105] J. Babensee *et al.*, “Host response to tissue engineered devices, Adv,” *Drug Del. Rev.*, vol. 33, pp. 111–139, 1998.
- [106] B. Rihova, “Immunocompatibility and biocompatibility of cell delivery systems,” *Adv. Drug Deliv. Rev.*, vol. 42, pp. 65–80, 2000.
- [107] R. F. Nicosia and A. Ottinetti, “Modulation of microvascular growth and morphogenesis by reconstituted basement membrane gel in three-dimensional cultures of rat aorta: a comparative study of angiogenesis in matrigel, collagen, fibrin, and plasma clot,” *Vitr. Cell. Dev. Biol.*, vol. 26, no. 2, pp. 119–128, 1990.
- [108] M. L. Ponce, “Tube formation: an in vitro matrigel angiogenesis assay,” in *Angiogenesis Protocols*, 2nd ed., New York: Springer Science & Business Media, 2005, pp. 183–188.
- [109] V. L. Cross *et al.*, “Dense type I collagen matrices that support cellular remodeling and microfabrication for studies of tumor angiogenesis and vasculogenesis in vitro,” *Biomaterials*, vol. 31, no. 33, pp. 8596–8607, 2010.
- [110] S. Roy *et al.*, “Platelet-rich fibrin matrix improves wound angiogenesis via inducing endothelial cell proliferation,” *Wound Repair Regen.*, vol. 19, no. 6, pp. 753–766, 2011.
- [111] R. R. Rao, A. W. Peterson, J. Ceccarelli, A. J. Putnam, and J. P. Stegemann, “Matrix composition regulates three-dimensional network formation by endothelial cells and mesenchymal stem cells in collagen/fibrin materials,” *Angiogenesis*, vol. 15, no. 2, pp. 253–264, 2012.
- [112] J. E. Scott, “Extracellular matrix, supramolecular organisation and shape,” *J. Anat.*, vol. 187 (Pt 2, pp. 259–69, 1995.
- [113] J. M. Rhodes and M. Simons, “The extracellular matrix and blood vessel formation: not just a scaffold,” *J. Cell. Mol. Med.*, vol. 11, no. 2, pp. 176–205, 2007.
- [114] K. S. Anseth, C. N. Bowman, and L. Brannon-Peppas, “Mechanical properties of hydrogels and their experimental determination,” *Biomaterials*, vol. 17, pp. 1647–1657, 1996.
- [115] G. P. Dillon, X. Yu, A. Sridharan, J. P. Ranieri, and Ravi V. Bellamkonda, “The influence of physical structure and charge on neurite extension in a 3D hydrogel scaffold,” *Biomater. Sci.*, vol. 9, no. 10, pp. 1049–1069, 1998.
- [116] Z. Li and J. Guan, “Hydrogels for cardiac tissue engineering,” *Polymers (Basel)*, vol. 3, no. 2, pp. 740–761, 2011.
- [117] A. Atala and D. J. Mooney, *Synthetic biodegradable polymer scaffolds*. pringer Science & Business Media, 1997.
- [118] C. K. Kuo and P. X. Ma, “Ionically crosslinked alginate hydrogels as scaffolds for tissue engineering: Part 1. Structure, gelation rate and mechanical properties,” *Biomaterials*, vol. 22, no. 6, pp. 511–521, 2001.
- [119] B. K. Mann, A. S. Gobin, A. T. Tsai, R. H. Schmedlen, and J. L. West, “Smooth muscle cell growth in photopolymerized hydrogels with cell adhesive and

- proteolytically degradable domains: Synthetic ECM analogs for tissue engineering,” *Biomaterials*, vol. 22, no. 22, pp. 3045–3051, 2001.
- [120] J. A. Rowley, G. Madlambayan, and D. J. Mooney, “Alginate hydrogels as synthetic extracellular matrix materials,” *Biomaterials*, vol. 20, no. 1, pp. 45–53, 1999.
- [121] J. L. Drury and D. J. Mooney, “Hydrogels for tissue engineering: Scaffold design variables and applications,” *Biomaterials*, vol. 24, no. 24, pp. 4337–4351, 2003.
- [122] B. Bhana *et al.*, “Influence of substrate stiffness on the phenotype of heart cells,” *Biotechnol. Bioeng.*, vol. 105, no. 6, pp. 1148–1160, 2010.
- [123] L. Jongpaiboonkit *et al.*, “An adaptable hydrogel array format for 3-dimensional cell culture and analysis,” *Biomaterials*, vol. 29, no. 23, pp. 3346–3356, 2008.
- [124] W. J. Larsen, “Development of the heart and vasculature,” in *Human Embryology.*, 3rd ed., New York: Churchill Livingstone, 2001, pp. 151–228.
- [125] B. Bhushan and M. Caspers, “An overview of additive manufacturing (3D printing) for microfabrication,” *Microsyst. Technol.*, vol. 23, no. 4, pp. 1117–1124, 2017.
- [126] J. W. Choi, R. Wicker, S. H. Lee, K. H. Choi, C. S. Ha, and I. Chung, “Fabrication of 3D biocompatible/biodegradable micro-scaffolds using dynamic mask projection microstereolithography,” *J. Mater. Process. Technol.*, vol. 209, no. 15–16, pp. 5494–5503, 2009.
- [127] S. Moon *et al.*, “Layer by Layer Three-Dimensional Tissue Epitaxy by Cell-Laden Hydrogel Droplets,” *Tissue Eng. Part C*, vol. 16, no. 1, pp. 157–166, 2010.
- [128] P. S. Maher, R. P. Keatch, K. Donnelly, R. E. Mackay, and J. Z. Paxton, “Construction of 3D biological matrices using rapid prototyping technology,” *Rapid Prototyp. J.*, vol. 15, no. 3, pp. 204–210, 2009.
- [129] D. Tian, Y. Song, and L. Jiang, “Patterning of controllable surface wettability for printing techniques,” *Chem. Soc. Rev.*, vol. 42, no. 12, p. 5184, 2013.
- [130] W. L. Wang, C. M. Cheah, J. Y. H. Fuh, and L. Lu, “Influence of process parameters on stereolithography part shrinkage,” *Mater. Des.*, vol. 17, no. 4, pp. 2015–213, 1996.
- [131] J. Stampfl *et al.*, “Photopolymers with tunable mechanical properties processed by laser-based high-resolution stereolithography,” *J. Micromechanics Microengineering*, vol. 18, no. 12, 2008.

Chapter 2

FABRICATION AND CHARACTERIZATION OF GELS WITH INTEGRATED CHANNELS USING 3D PRINTING WITH MICROFLUIDIC NOZZLE FOR TISSUE ENGINEERING APPLICATIONS

Complete citation:

Rana Attalla, Celine Ling and Ponnambalam R Selvaganapathy. *“Fabrication and characterization of gels with integrated channels using 3D printing with microfluidic nozzle for tissue engineering applications.” Biomedical microdevices* 18.1 (2016): p.17.

Relative Contributions:

Attalla, R: Designed and performed all characterization experiments including nozzle fabrication, hydrogel printing, perfusion, and imaging. Interpreted and analysed the resulting data, and wrote the manuscript.

Ling, C: Assisted with biological cell culture and maintenance.

1. Introduction

Bioprinting is the ability to precisely position cells, soft material gels, and extracellular matrices in 3D. It has been of significant interest over the past two decades due to its potential in applications such as organ replacement, drug discovery, and biological studies [1]. Organ transplantation still remains as the ultimate approach to treating end-stage failure [2]. However, this therapy is invasive, costly, and the shortage of organs available for transplantation remains a serious problem. Therefore, new accessible therapies are needed to treat the millions of patients with organ failure worldwide. The goal is to develop a method for fabrication of natural-like, functional human tissue in order to repair and replace damaged or lost human organs. Bioprinting also shows promising potential for use in the drug discovery field. Currently used 2D culture models are not ideal for simulation of true 3D biological environments. Inkjet printing has already been used for years to print “bioinks” consisting of cells, DNA, and biomaterials [3,4], while fused deposition modelling (FDM) has been used to create 3D multi-material scaffolds for cell seeding [5]. The advantage of bioprinting is the ability to fabricate 3D multi-cellular structures with various biomaterials and extracellular matrices in order to recreate and understand cell interactions, behaviours, and relationships found in the human body. Human tissue architecture integrated with vascular networks provides a platform for the study of a more realistic physiological response to drug delivery, as well as an ideal replacement for damaged organs.

Classical tissue engineering methods involve fabrication of scaffolds made of either natural or synthetic materials and cells of interest seeded onto them [6–10]. These methods have been available for years, and have been used to restore and maintain the normal function of damaged tissues and organs. More recently, focus has shifted towards the additive layer-by-layer robotic biofabrication processes used to construct 3D functional living macrotissues and organ constructs [11–13]. This technology provides advantages over classical tissue engineering, including high precision of anatomic geometries as well as advanced control of cell seeding and alignment. This technique offers the ability to create spatially heterogeneous multimaterial structures by utilizing deposition tools that can simultaneously extrude a wide range of materials.

However, one particular area that has proved to be technically challenging in both these approaches is the integration of vascular networks in the scaffolds [14]. A few attempts have been made using microfluidic chips [15,16] as well as scaffold-free approaches based on tissue spheroids [17–20]. Some groups have also developed hybrid techniques involving both printing and sacrificial moulding of carbohydrate glasses, agarose gels, or gelatin, as well as bulk hydrogel immersion in a variety of extracellular matrices such as Matrigel, collagen, and fibrin[21–26]. Majority of these methods for vascular fabrication require additional steps including time-consuming fabrication of complex microfluidic chips, pretreatment or modification of material, removal of sacrificial materials, or slow layer-by-layer assembly. Other approaches that use flow focusing and extrusion methods where hollow gel fibers are deposited into a solution [27,28] have also been investigated. However, fibers cannot be precisely patterned and aligned in a solution, while anchoring of the gel poses a problem in cases where a mesh is used to drain the fluid [29]. Adhesion between fibers would also be difficult due to the immediate gel crosslinking that occurs upon submersion into a bath or wet substrate.

We have previously presented a preliminary proof-of-concept [30], demonstrating our ability to successfully integrate patterned hollow channels into bulk gels on a dry substrate using a commercial, open-source 3D printer in a single step process. However, the printing process was not fully characterized and viability of human cells in these printed structures was not demonstrated. Other groups have also used 3D printing to form gels embedded with hollow channels using a multi-step process. One group demonstrated fabrication of fully cross linked hollow tubes using a pressure-assisted freeform fabrication platform with a coaxial dispenser unit [26,31] creating a scaffold structure and then subsequently embedded the the extruded tubes into a bulk gel containing cells. More recently, another group of researchers used 3D printing process to printing hollow overlapping tubes and and immediately submerged the printed layer into crosslinker solution [32] to integrate the overlapping channels into a bulk gel structure. Both these groups have reported using higher concentrations of gel and cross-linker that allow for more rigid, mechanically stable structures, but may not be optimal environments for cell seeding and growth [33,34]. The high viscosity of pre-gelled solutions typically used in these demonstrations may decrease cell viability due to potential hydrodynamic damage

to the cells that occurs during mixing with these solutions [33]. High concentrations of crosslinker materials (>2%) can also have a negative impact on the cell's salt balance [34]. Therefore, development and complete characterization of the operating range of a single step printing process that could form structures with embedded channels for perfusion is needed. The concentrations of the polymer and the crosslinker used to form the gels should be such that they are suitable for growth of various types of cells. Finally, the technique should be versatile to change the dimensions of the channels printed in real-time so that dimensions of the channels printed could be dynamically changed to mimic real vascular geometry.

Here we describe a method for fast fabrication of gel layers with interspaced hollow tubes, directly on dry substrates, in precise geometries using a low- cost open-source 3D printer with custom-built a microfluidic nozzle. The printer uses the lowest reported gel and cross linker concentrations and produces stable and perfusable structures. We chose to use a low cost (\$600) printer as compared to expensive custom built options (\$20K) [26] that are typically used in extrusion based printing so that this technology can be widely available to all and users and researchers. In this paper, we perform for the first time, a full characterization of the operating range (printspeeds and extrusion flow rates) and capabilities of such a printer in producing patterned structures that are similar to the design. With this system, we demonstrate the ability to construct multi-layered structures with precise control of channel position, spacing, and diameter. We also demonstrate for the first time that these factors can be simultaneously manipulated during printing in order to create a single gel structure with variable architecture. The hollow tubes can have a wide range of diameters, are immediately perfusable, and could serve as vascular networks for tissue engineering applications. The interiors of scaffold-engineered tissue grafts are usually associated with poor nutrient diffusion. Perfusion from these embedded channels allows the required nutrients to reach cells in the bulk region of the construct, thus increasing cell viability.

2. Methods and Materials

2.1 Printing apparatus and setup:

The open-source printer (RepRapPro Mendel), which included an XYZ positioner (0.1 mm positioning accuracy) and a heated printbed (FIG. 2.1a), was modified with a custom built microfluidic printhead for coaxial hollow fiber extrusion (FIG. 2.1b). The original nozzle, intended for thermoplastic extrusion, was removed and code alterations were made such that the motor required for polylactic acid (PLA) feed was disabled. The printhead operated at a maximum speed of 40 m/min within the build envelope (20 cm W, 20 cm D, 14 cm H). Standard 3D CAD (STL) files were converted to printing instructions through open source g-code compiler software (Slic3r). Custom g-code files for specific line-by-line patterns were translated into movement commands using an open-source interpreter (Printrun) [see Appendix for sample code].

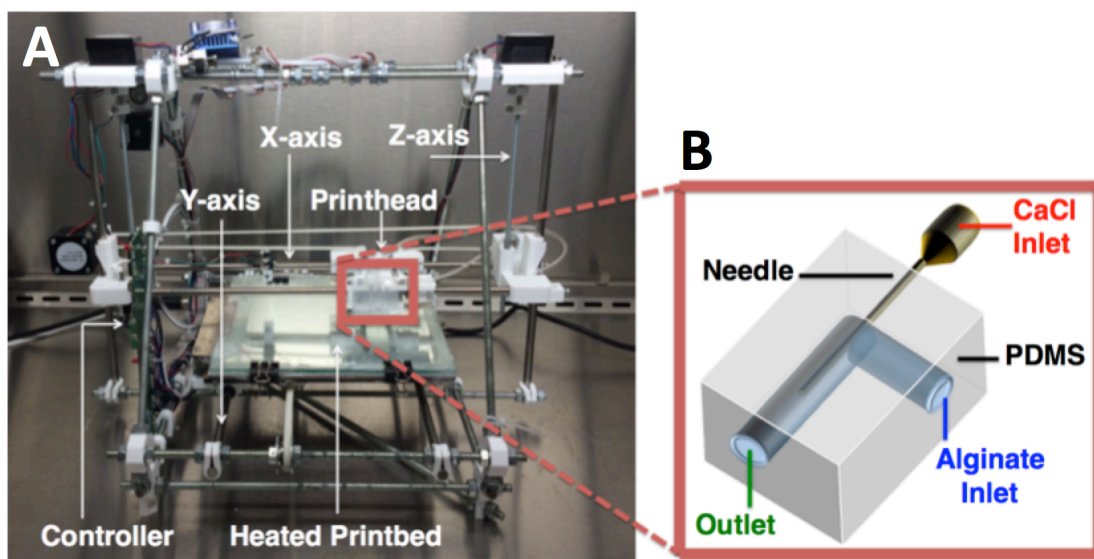


FIG. 2.1: (A) Modified 3D RepRap printer. (B) Coaxial extrusion nozzle schematic: 700 μ m needle, 2mm L-shaped channel.

The microfluidic printhead (FIG. 2.1b) consisted of an L-shaped cylindrical channel (2 mm) with an embedded central needle (700 μ m inner diameter). The distance between the nozzle outlet and inner needle outlet was 1.5 cm. A mould for this device was created using high resolution 3D printing of acrylic plastic. Polydimethylsiloxane

(PDMS) pre-polymer was cast and two elastomeric replicas were bonded together using oxygen plasma with the needle aligned along the centre. The format of the printhead is such that it can accommodate any number of co-axial streams simply by introducing additional L-shaped bends with embedded needles along the length of the channel.

2.2 Material extrusion:

The coaxial microfluidic printhead produced a central flow of CaCl₂ solution (100 mM, Fisher Scientific) surrounded by an annulus of sodium alginate (2% w/w, Sigma Aldrich). This concentric flow was extruded from the printhead as it was moved using a XYZ positioner leading to a patterned deposition on to a dry printbed. Diffusion of calcium ions from the inner stream into the surrounding alginate caused gelation to occur in the annulus and resulted in the formation of a hollow tube.

2.3 Cell culture and preparation:

Preliminary experiments with cells were done using *Escherichia Coli* K12, which was inoculated into 4 mL of LB (Luria Bertani) medium, with 4 µL ampicillin (100 µg/mL) and grown with vigorous shaking (~250 rpm at 37°C) to saturation growth (~12-16 hours for stationary phase). A final concentration of 10⁶ cells/mL in alginate was used for printing. Human umbilical vein endothelial cells (HUVEC) (Lonza Inc.) were later purchased and cultured. Endothelial basal media (EBM) (Lonza Inc.) was supplemented with fetal bovine serum (FBS), vein endothelial growth factor (VEGF), hydrocortisone, ascorbic acid, heparin, and gentamicin (GA-1000). This was used to make media changes to cell culture plates one day prior to experimentation in order to ensure 100% confluency and high cell yield. Sodium alginate powder and calcium chloride were sterilized with UV light. Alginate-EBM and calcium-EBM based solutions were made at 2% w/v and 0.1 M respectively. HUVECs were harvested using 0.25% Trypsin-EDTA and the cell suspension was diluted accordingly to create the required cell concentrations. Experiments were done using cell concentrations of 1.5x10⁶ cells/mL. The cell suspension was mixed in with the sodium alginate solution and left in the incubator for 1 hour prior to printing in order to improve cell dispersion and consistency in solution and avoid any clumping.

2.4 Cell-laden gel printing and maintenance

Printing procedures were carried out as previously described in order to create cell laden gel structures. In this case, EBM-based alginate and calcium were used as the outer and the inner fluids instead of water-based solutions. HUVECs were resuspended within the alginate solution prior to printing. Printed hollow channels were perfused with EBM in order to maintain the construct over a period of 72 hours. The sample was incubated in calcium-EBM based solution in order to avoid leeching of calcium from the gel structure. Re-perfusion and media changes were made daily in one set of samples. Another set of samples was left without perfusion, and only surrounding media changes were made.

2.5 Cell-laden gel imaging:

Live stain images of printed samples were taken using confocal microscopy (LSM510, Zeiss). Samples were stained using calceinacetoxymethyl ester (calcein AM) and ethidium homodimer-2 (Life Technologies) at a concentration of 0.5% v/v. Images of single cells embedded within the construct were obtained by sectioning 100 nm sample slices (Leica UCT Ultramicrotome) and post-stained with uranyl acetate and lead citrate for viewing using transmission electron microscopy (JEOL JEM 1200 EX TEMSCAN) [see Appendix for details].

3. Results and Discussion

3.1 Material extrusion:

Ionic crosslinking is one of the most common gelling methods used for sodium alginate, particularly using Ca^{2+} from calcium chloride solution as the crosslinking agent. Ionically crosslinked gels can be dissolved by the release of crosslinker ions in exchange for physiologically available monovalent cations such as sodium, making them a viable choice for biological application [26–29,32,35,36]. The concentration of calcium and its diffusion into the alginate coaxial layer govern the crosslinking phenomenon. The length of the printhead's outlet channel and the flow rates used are both major factors in

determining the extent of diffusion, and thereby affect the dimensions of the resulting tubes.

Typically alginate is extruded into a bath containing calcium chloride to form solid free floating wires [27]. The same procedure can be used with calcium chloride solution in the core and alginate in the annulus to form freely floating tube-like structure [28]. Inner and outer tube diameters of the fabricated hydrogel tubes can be changed by manipulation of respective flow rates (FIG. 2.2a-c).

Flow rates were tested between 1 to 20 mL/min using our coaxial nozzle. One set of experiments involved holding the inner calcium chloride flow constant at 10 mL/min, while the outer alginate flow rate was varied at 5, 10, and 20 mL/min. The second experiment varied the inner flow (5, 10, 20 mL/min) while the outer flow was constant at 10 mL/min. It was found that an increase in inner and outer flow rate resulted in a larger inner and outer diameter respectively. Similarly, a decrease in each of the flow rates caused their corresponding diameters to diminish, as was expected from previous work involving triaxial nozzles [28]. However, tubes extruded into a bath, as has been done in the past, cannot be precisely positioned, assembled or patterned onto a dry substrate. Extrusion into a bath solidifies the outer gel layer instantaneously, thereby ensuring that the tubes stay apart and cannot be integrated into a monolithic unit. Our work addresses both of these issues by integrating our coaxial extrusion mechanism with 3D printing.

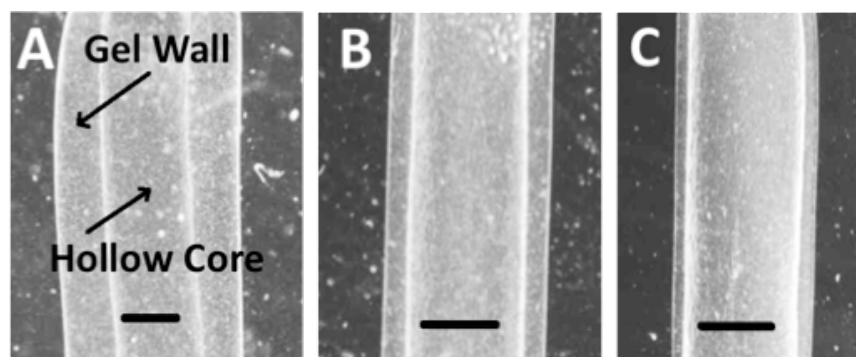


FIG. 2.2: (A-C) Hollow tubes extruded into CaCl_2 bath. Inner flow is constant at 10mL/min, while outer flow is (A) 20, (B) 10, and (C) 5mL/min respectively. Tubes extruded into a bath cannot be precisely positioned on a substrate. Extrusion into a bath solidifies the outer layer of the gel instantaneously and does not allow merging of adjacent tubes. Scale bars, 1mm.

3.2 Contiguous gel layer formation and perfusion:

When printed onto a dry substrate, the tubes were expected to be extruded in a configuration as shown in FIG. 2.3a where a gel tube would be formed due to extensive diffusion of the calcium ions into the alginate. This is indeed the case when the concentration of the calcium ions in the inner solution is high, the length of the printhead's co-flow channel is long. However, when the diffusion of calcium ions is not as extensive (in the order of milliseconds), the inner side of the annular alginate layer was crosslinked while the uncrosslinked solution on the outside spread laterally (FIG. 2.3b) prior to eventual crosslinking resulting in fusion between one parallel tube to the next (FIG. 2.3c). This formed a continuous solid gel layer with embedded, hollow channels (FIG. 2.3d) that were precisely placed according to the design used for printing (patterns depicted in FIG. 2.3e for monolayer structures and FIG. 2.3f for multilayer structures). This fusion phenomenon occurred provided that the distance between two adjacent channels is less than 3 mm. Under this separation distance, the initially uncrosslinked alginate solution was able to flow to fill the gaps between tubes. Once the gaps were filled, the calcium ions that are present in the annulus at high concentration continue to diffuse into the uncrosslinked alginate filling the gaps, eventually solidifying it. A continuous gel layer interspersed with channels that allows for perfusion was formed. A cross-section of this can be seen in FIG. 2.3g. This novel approach allows fast and easy printing of gel layers with well aligned, adjacent hollow channels using a simple one-step process (FIG. 2.3h). The length and width of the printed structure was only limited by the size of the printed.

The individual channels were extruded in a continuous fashion, allowing adjacent tubes to be connected at the ends (FIG. 2.3i). This allowed the entire 3D gel layer to be easily perfused. Media was able to flow easily from one end of the structure to the other without any obstruction, regardless of how the channels were patterned. However, printing at a gap spacing less than 0.5 mm caused overlap between hollow cores of the printed filaments. Although the channel was contiguous and perfused media was still able to flow through the construct, the top surface of the printed construct was no longer level and formed a periodic wavy shape.

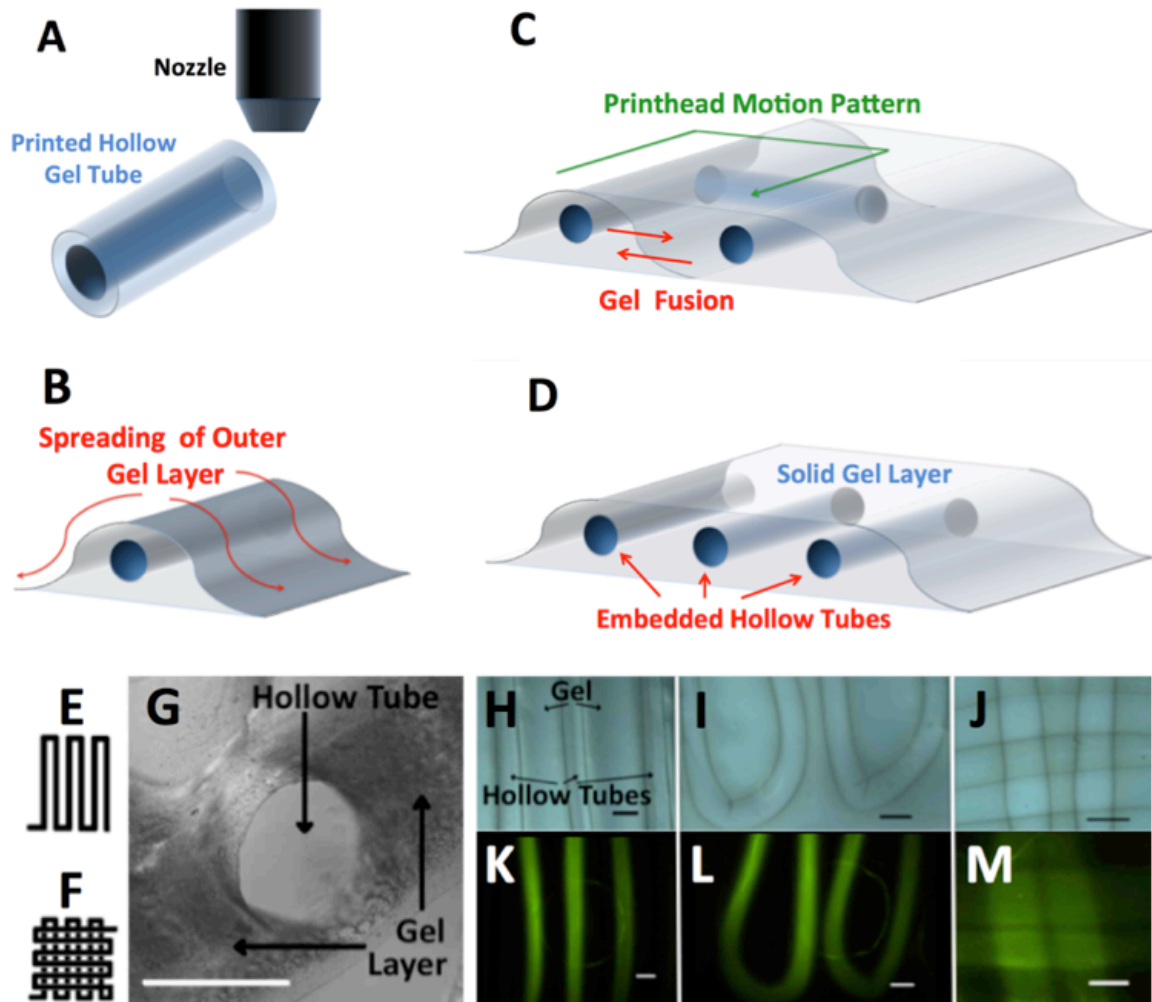


FIG. 2.3: Formation of a continuous gel layer with embedded hollow channels due to extrusion onto a dry substrate. (A) Extrusion of hollow gel tube onto substrate. (B) Later spreading of the outer uncrosslinked alginate layer of the tube. (C) The delay in the gelation of the outer alginate layer causes fusion of adjacent tubes during patterned deposition. (D) The final result is a solid gel construct with embedded, connected hollow channels. (E) Single and (F) dual layer patterns used for extrusion-based printing. (G) Cross-section of continuous gel layer formed. Hollow tube can be seen embedded in gel layer. (H) Parallel tubes printed continuously using the pattern in (E) show good alignment. (I) Bent connections between adjacent tubes when continuously printed. (J) Multi layer printing using pattern in (F). (K-M) FITC- nanoparticle flow through tubes shown in H-J respectively. Scale bars, 1mm.

Multi-layer hydrogel structures were also created with a connection from channels in one layer to the next, provided that printing was continuous (FIG. 2.3j). Channels did not collapse under the weight of additional layers but rather maintained their hollow form. The gel thickness between layers varied slightly depending on the alginate flow rate and printhead speed (~150–350 μm for 1–10 mL/min respectively). FIG. 2.3k,l,m show perfusion of the printed gel structures with solution containing fluorescent nanoparticles that demonstrate the structural integrity of both single and multilayer printed structures. The initial crosslink to form the structure of the channel, the speed of the printing that lays down the perfusion network, the rate of spread of the uncrosslinked gel to fill the gaps and the subsequent diffusion and crosslink of the gel due to diffusion of Ca^{2+} from the channels have to be optimized in order to ensure the formation of a continuous gel layer with structurally stable and interspersed vascular channels.

3.3 Characterization of flow rate and printhead speed:

We investigated the effect of flow rate and printhead speed on the printing process in order to establish dynamic working range of a bioprinter. Within the defined boundaries of this working range, the printer was expected to produce a printed pattern that is comparable to that of the original design in terms of its filament length and placement.

Flow rates available for testing were between 1-30 mL/min (limited by the syringe pump) and printhead speeds were varied from 1-40 m/min (limited by the printer motors). Experiments were performed by measuring the extruded structure dimensions, while fixing the flow rate and varying the printhead speeds. For simplicity both the inner and the outer flow rates were set at the same value in each of the experiments. The flow rate was then varied over the entire available range and the results presented in FIG. 2.4. At low flow rates (extrusion velocities) and high printhead speeds, the position of the printed fibers deviated significantly from the design, along the direction of printing as shown in FIG. 2.4a-i (red region). The poor pattern registration was likely because there was insufficient time for the material to settle and adhere on the substrate. This set of conditions was therefore, designated as poor pattern definition region. At very high flow rates (extrusion velocities) and irrespective of the printhead speeds, flow instabilities

occurred leading to formation of coils as shown in FIG. 2.4a-ii (blue region). It was designated as the flow instability region. Printing with flow rates and printhead speeds between these regions resulted in consistent fabrication of gel structures that contained parallel, uniform hollow channels (FIG. 2.4a-iii) with good registration and this region (green) was designated as the working range. Both the flow instability and poor registration regions may have arisen because of a mismatch between the extrusion velocity of the fiber and the speed of the printhead over the substrate. Ideally, one would expect that the registration of the pattern would be precise when the extrusion velocity matches with the printhead speed. At low flow rates the extruded fiber does not emerge fast enough from the nozzle to match the printhead speed. As the extruded fiber touches the dry substrate, it adheres at certain locations. Since the printhead speed is high, the fiber could potentially stretch between the points of adhesion. However, when encountering a bend the points of adhesion are closeby and therefore the printed fiber cannot be stretched as much as that along a straight line leading to a deviation from the printed pattern at those bends as seen in FIG. 2.4a-i. At high flow rates, the material is extruded at a rate much higher than that which could be accommodated smoothly due to relative motion between the printhead and the printbed. This leads to a classic coil pattern [37] indicating material piling and accumulation at these conditions. However, it should be noted that the continuous formation of gel while printing will also affect the viscosity of the extruded fiber making the process significantly more complex to analyze.

The average velocity with which the material is extruded can be calculated according to Eq. 1:

$$V = \frac{Q_{total}}{\pi r^2} \quad (1)$$

where V is the average extrusion velocity, Q_{total} is the total flow rate of CaCl₂ and alginate, and r is the nozzle radius. It was expected that a linear co-relation between the printhead velocity and material extrusion velocity will determine condition above which the flow instabilities would occur. Instead, it was found that there exists a critical flow velocity above which flow instabilities inevitably occur irrespective of the print-head speed within this range. This critical point occurred when both inner and outer flow rates were 13 mL/min, which translated to an overall average extrusion flow rate of 26

mL/min. The reason for this non-linearity may be because sodium alginate is a non-Newtonian fluid demonstrating viscoelastic properties. The process of gelling also leads to increase in viscosity of the extruded material. The dynamic viscosity of alginate is dependent on shear rate [38] and can be modelled using the Ostwald relation [39–43]:

$$\mu = K\gamma^{n-1} \quad (2)$$

Here, μ is dynamic viscosity, K is a scaling constant, and γ is shear rate. As the alginate gels upon extrusion, the gel viscosity increases in proportion to calcium ion diffusion into alginate coaxial layer [44–47]. It has been experimentally observed, both in our work and in other studies [26,32], that at lower flow rates a gel filament is extruded amongst a portion of uncrosslinked aqueous alginate. At higher flow rates, the gelled filament dimensions increase and the fraction of ungelled aqueous material decreases leading to a higher net effective viscosity. This indicates that a higher shear rate increases viscosity, and thereby reduces the Reynold's number [48]. It is well known that an asymmetric jet will reach a critical Re where fluid coiling/buckling occurs [49–51]. Since this critical point is dependent primarily on the extrusion velocity and not the printhead speed in the range of speeds under consideration, we see a sharp transition between precise printing and coil formation at various printhead speeds.

From FIG. 2.4a, the operating flow rates of 10 mL/min were found to be suitable as they produced precise pattern over a wide range of printhead speeds (5.5 – 40 m/min). However, the range of suitable flow rates was quite narrow. In order to expand the working range of flow rates, a set of conditions where the alginate flow rate was kept constant at 10 mL/min and flow rate of CaCl_2 solution was varied, was tested. The results shown in FIG. 2.4b, demonstrate that the working range of the printing process can be extended significantly. As shown in FIG. 2.4b precise patterns with <5% deviation were obtained in the range of inner flow rate of the CaCl_2 solution between 4-20 mL/min which corresponds to a total flow rate of 14-30 mL/min. This is in contrast to the much narrower range of 9-12 mL/min when the flow rates of both the fluids were set the same. The ability to vary the ratio between the inner and outer flow rates is critical in defining the inner diameter of the printed channels. Furthermore, the new conditions allow one to print rapidly even at very low flow rates. Development of a theoretical model would enable prediction of operating range of printing conditions for other gels with various

viscosity or concentration. However, the dynamics of fluid flow and material spreading is complex and could be a focus of subsequent research in this area.

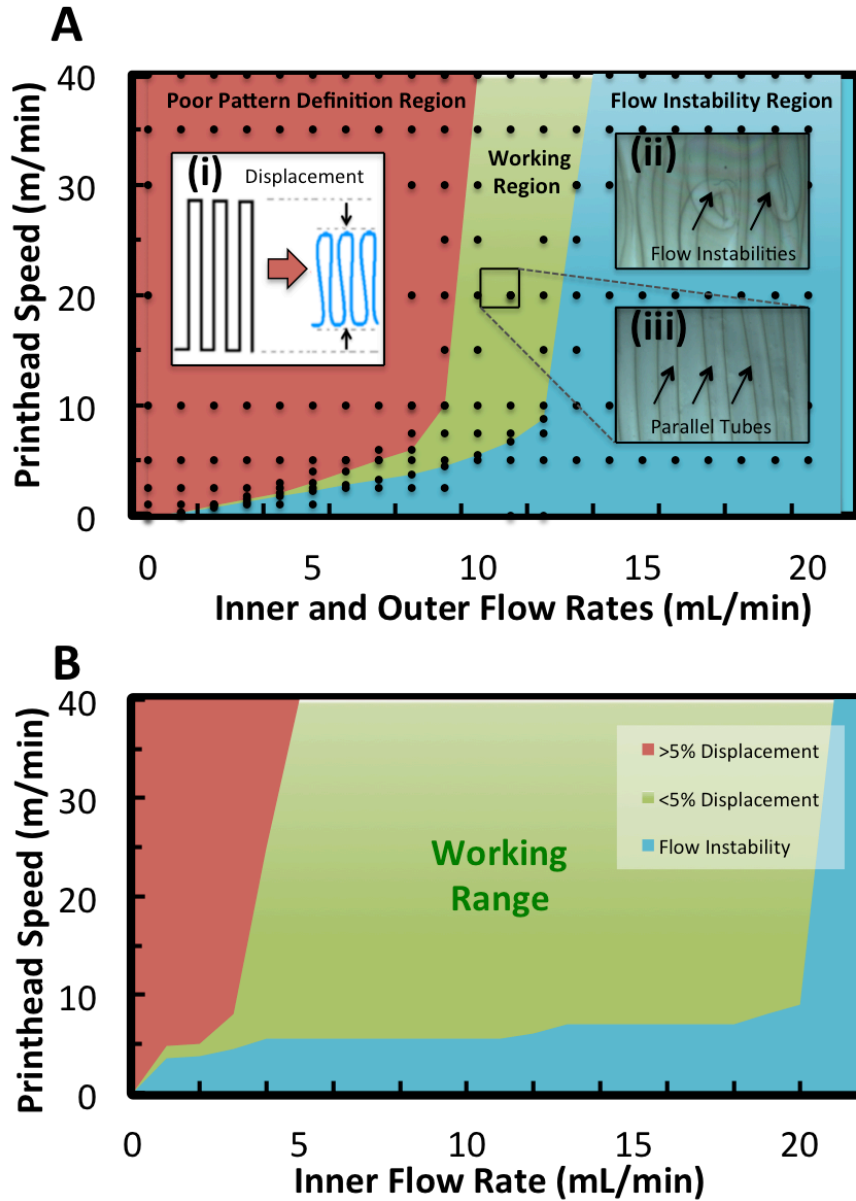


FIG. 2.4: Dynamic range of printing process using water-based alginate and calcium solutions when outer flow is (A) variable or (B) constant at 10mL/min. (A) shows points at which experiments were performed. (A-i) Illustration of gel displacement during operation above maximum speed. Because extrusion speed is significantly lower than that of the printhead, the tube is not given sufficient time to gel and settle on the substrate. This causes a displacement between intended patterning position and actual position. (A-ii) Flow instabilities occurring from operation below minimum speed. (A-iii) Parallel printed tubes resulting from printer operation in the optimal working range show good alignment.

3.4 Printing with cell media-based solutions:

Although distilled water-based cell-laden alginate structures have been successfully fabricated [26–28,32], media-based constructs provide a much more ideal environment for cellular integration in biological applications. Characterization of the relationship between printing flow rates and printhead speeds was repeated using cell media-based alginate and calcium chloride solutions (Fig. 2.5). Dulbecco's Modified Eagle's Medium (DMEM) and EBM-based solutions completed with 10% and 2% FBS respectively were used for testing. FIG. 2.5a shows that the region of precise definition occurred at lower flow rates as compared to the printing with alginate dissolved in DI water. Flow rates of 7 mL/min for both alginate and calcium chloride solutions produced conditions for the largest range of applicable printhead speeds (4 – 40 m/min) using media-based solutions. Similarly, the operating range of flow rates can be expanded when the inner and the outer flow rates are decoupled (FIG. 2.5b). Holding the outer alginate flow at 7 mL/min, the inner flow rate can be varied between 4-24 mL/min and still allow a wide range of printhead speeds to be used for precise registration of patterns.

The change in the operating range of the printer between cell media-based gels vs. gels prepared using water can be attributed to the viscosity of the solutions. Viscometer tests established that DMEM and EBM-based alginate solutions had viscosities that were significantly higher than that of water-based alginate (89, 190, 210cP for water-based, EBM/FBS-based, and DMEM/FBS-based alginate solutions respectively), which may be due to some amount of calcium chloride present in the media. Therefore the initial starting point of the cell media based solution is higher. It reaches the critical threshold for transitions between the different regimes faster and therefore the range of operation is shifted to lower speeds.

Temperature changes also impact fluid properties. Increases in temperature generally result in a decrease in fluid viscosity [52]. For example, water has a viscosity of 1cP at 20°C and 0.7cP at 37°C [53]. Similarly, DMEM and FBS viscosities are 0.78cP and 0.86cP respectively at 37°C [53–55]. Printing experiments were repeated using solutions at both 20 and 37°C, but the temperature variations did not impact the operation

of the printing process. Printing of various cell concentrations ($0.5, 1.5, 2.5, 4 \times 10^6$ cells/mL) was also tested, but no significant changes to the working range were observed.

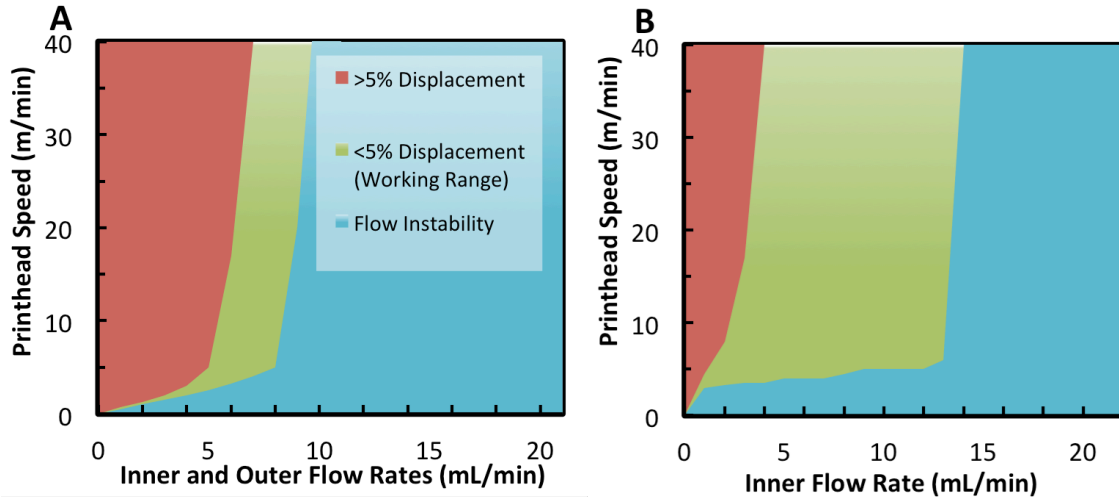


FIG. 2.5: Dynamic range of printing process using DMEM or EBM-based alginate and calcium solutions with 2% or 10% FBS when outer flow is (a) variable or (b) constant at 7mL/min. (Red) >15% displacement. (Orange) 5-15% displacement. (Green) <5% displacement – working range. (Blue) Flow instabilities.

3.5 Characterization of channel diameters:

Channel diameter of the printed hollow structures can be dependant on a variety of parameters, such as extrusion flow rates and printhead speeds. The effect of these two variables on channel size was investigated. In these experiments, outer flow rate of sodium alginate was constant at 10 mL/min during printing, while inner flow rates were varied between 5, 10, 15 and 20 mL/min and print head speed was varied from 10, 20, 30 and 40 m/min. The hollow channel diameters printed using each of the different inner flow rates were measured at each printhead speed ($n = 10$). A wide range of inner core diameters was achieved using this process: from 600 μm (5 mL/min and 40 m/min) to 1.8 mm (20 mL/min and 10 m/min) (Fig. 2.6a). It was found that large changes in core diameter were obtained by altering flow rate, while finer changes were made by adjusting the printhead speed (FIG. 2.6a). This demonstrated versatility in methods of control for both patterning and diameter definition. Operation at lower flow rates caused a decrease in core volume of the inner calcium chloride solution that eventually defined the hollow

channel, thereby resulting in smaller channel diameters. The channel diameter also decreased with respect to printhead speed. This may be due to longitudinal stretching of the deposited gel fiber as a result of calcium alginate’s elastic nature. Operation at lower printhead speeds allowed for the highest consistency and uniformity in channel diameter. There was a slight increase in variability of channel diameter as printing speeds were increased. It was also found that diameter changes with varying printer speeds were steeper when operating at higher flow rates.

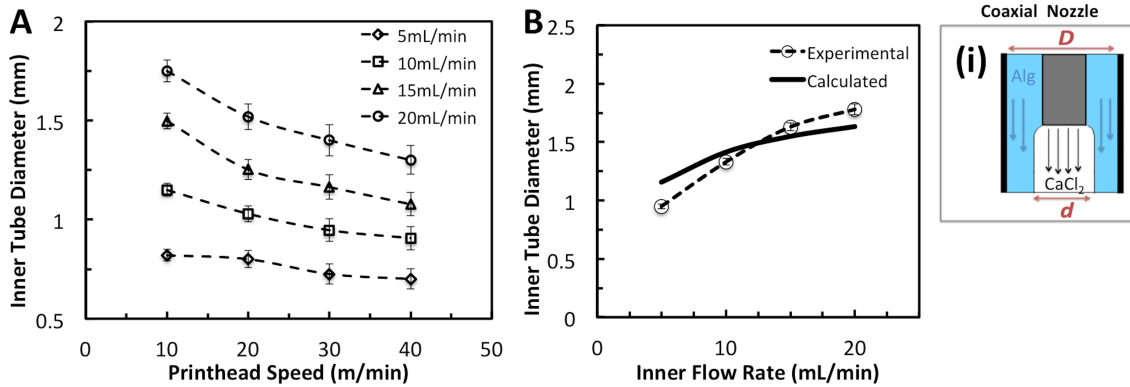


FIG. 2.6: (A) Inner tube diameter changes with respect to printhead speed and CaCl₂ flow rate. Flow rates of 5mL/min, 10mL/min, 15mL/min, and 20mL/min. Outer flow constant at 10mL/min. Tube diameters are found to decrease at lower flow rates and higher printhead speed. (B) Experimental and theoretical values of channel diameter at minimum printing speed. Minimum printing speeds were 5, 6, 7, and 9m/min for 5, 10, 15, and 20mL/min respectively. (B-i) Coaxial nozzle illustration showing core (*d*) to nozzle (*D*) diameter ratio for calculating tube diameters.

The observed experimental channel diameters were compared to expected values (FIG. 2.6b). These were calculated using inner to outer cylindrical volume ratios with respect to corresponding inner and outer flow rate ratios, shown in Eq.3:

$$\frac{Q_i}{Q_o} = \frac{\pi h \left(\frac{d}{2}\right)^2}{\pi h \left[\left(\frac{D}{2}\right)^2 - \left(\frac{d}{2}\right)^2\right]} \quad (3)$$

where Q_i and Q_o are inner and outer flow rate respectively, and d is core diameter (FIG. 2.6b-i). Printed channels were fabricated at various flow rates and their corresponding

minimum printhead speeds that produce precise definitions. This condition ensures that the printed channels are not stretched extensively. Print speeds of 5, 6, 7, and 9 m/min were used for inner flow rates of 5, 10, 15, and 20 mL/min respectively. The outer flow rate was constant at 10 mL/min. The diameters of these printed channels were then measured and compared to calculated values. The results demonstrate that there was agreement between the experimental values and the calculated ones. This confirms that the definition of the channel and its inner diameter is largely determined by the volumetric ratio of the co-flow conditions.

3.6 Demonstration of dynamic channel size changes:

Tissues in the body are composed of hierarchical vascular channels containing arteries, veins, and capillaries. Any true biological vascular network contains blood vessels of different dimensions, and therefore it may be necessary to be able to reproduce a similar morphology within the bioprinted tissue constructs. Schematic images shown in FIG. 2.7a-c represent potential designs for gel constructs with stepwise, alternating, or continuous changes in embedded channel dimensions. To emulate these schematic designs, flow rates were changed “on-the-fly” during the printing process using a programmable syringe pump in order to produce a variety of channel diameters within a single gel structure. The printhead speed was kept constant at 10m/min throughout the entire printing process. Alginate flow was set at 10 mL/min, while calcium flow was varied between 5, 10, and 15 mL/min in order to create channel diameters of 800 μ m, 1.2 mm, and 1.5 mm respectively. Filaments were printed to a length of 20 cm, with flow rate changed continuously every 1s. In FIG. 2.7d, channel diameter was decreased in a stepwise fashion by ramping the calcium flow rate down from 15 mL/min to 10 mL/min, and then to 5 mL/min. Alternating changes in channel diameter were achieved in FIG. 2.7e by pulsing the inner flow rate between 5 and 10 mL/min. Finally, the diameter of a single channel was changed continuously by introducing a smooth decrease of the central flow rate from 10 to 5 mL/min, as seen in FIG. 2.7f. Our 3D printing technique was able to produce a spectrum of tube diameters, which was made possible by the system’s ability to print a wide range of flow rates.

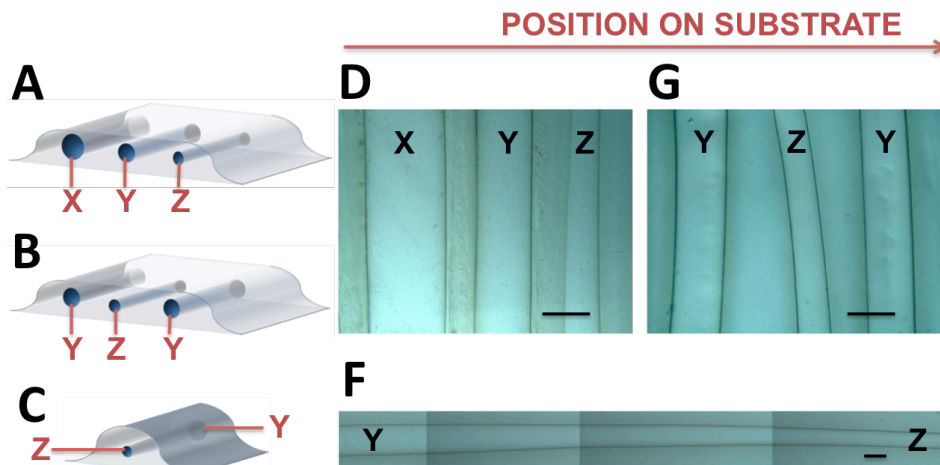


FIG. 2.7: (A-C) Schematic images illustrating single gel structures with varying changes in tube diameters: (A) stepwise, (B) alternating and (C) continuous increase or decrease in embedded channel dimensions. Dynamic change of tube diameters in a single gel structure is accomplished by varying CaCl_2 flow rates: (D) flow rate is increased stepwise (ramping) (E) flow rate is changed back and forth (pulsatile) (F) flow rate is changed continuously. X, Y, Z represent tubes generated by 15, 10, and 5 mL/min flow respectively. Outer flow constant at 10 mL/min. Scale bars, 1 mm.

3.7 Effect of material concentration:

The effect of material concentration on the relationship between applied flow rates and printhead speeds was examined. The ability to fabricate these channel-embedded structures is based on the diffusion gradient of calcium throughout the gel, which implies that changes in solution concentration would have a significant effect on the printing process. Printing using 0.5%, 1%, and 1.5% alginate as well as 25 mM, 50 mM and 75 mM calcium chloride solution was attempted. Flow rates of 4, 8, and 12 mL/min were tested using printhead velocities of 5, 20, and 40 m/min. Experiments were performed using both media-based and water-based solutions. Printing using alginate solution concentration <1.5% resulted in the extrusion of uncrosslinked liquid droplets (FIG. 2.8a), while calcium solutions of 25 or 50 mM produced amorphous crosslinked gel droplets (FIG. 2.8b). Printing using 75 mM CaCl_2 and 1.5% alginate was successful (FIG. 2.8c), and its performance was similar to that using 2% alginate and 100 mM calcium solution. These diameters of the printed structures and the definition of the patterns were consistent regardless of flow rate, print speed, and whether solutions were media or water

based. Other research groups have presented thorough characterizations of printing with alginate and calcium concentrations of $\geq 2\%$ [26,32]. However, printing under these conditions is not ideal for long-term cell maintenance. Increased viscosity at higher alginate concentrations would lead to cells being exposed to high shear forces during the mixing, which could cause cell death [33]. Higher concentrations of calcium can also create a hypertonic environment that would damage the cells [34]. Higher alginate and calcium solution concentrations were not tested, as they do not contribute to cell-friendly environments.

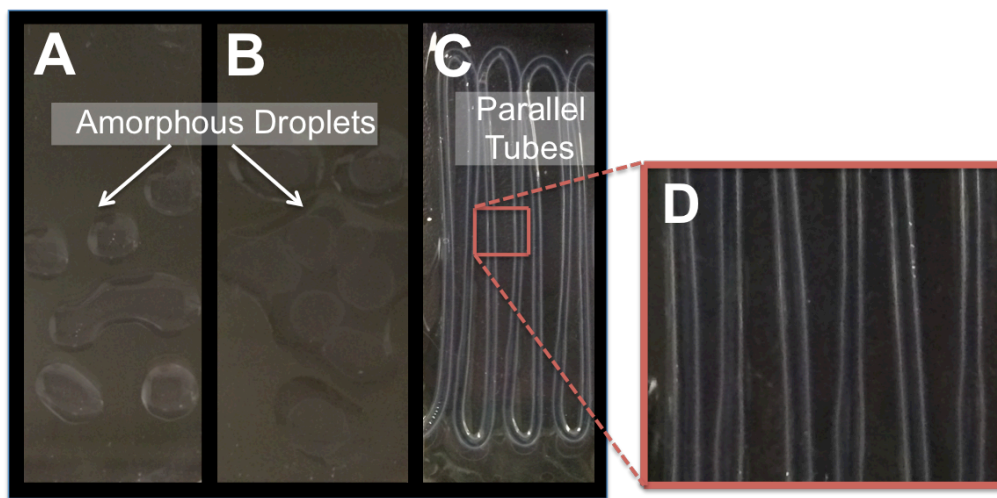


FIG. 2.8: Printing using variable concentrations of water-based alginate and calcium chloride solution. Similar results were observed using cell media-based solutions. (A) Unsuccessful printing using 0.5% alginate solutions. Uncrosslinked liquid droplets were dispensed. Similar results were observed using 1% solutions. (B) Unsuccessful printing using 25mM calcium solution. Amorphous, crosslinked gel droplets were produced. Similar results were seen using 50mM solutions. (C) Successful printing using 100mM calcium solution and 2% alginate results in channel fabrication. Similar results were observed using 75mM and 1.5% calcium and alginate solutions respectively. (D) Close-up of parallel channels in (C).

3.8 Effect of change in direction during printing:

Printing various shapes and patterns involves acceleration and deceleration of the print head and variation in print speed. In particular printing a 90° bend requires the print head to decelerate from steady state to zero velocity in one direction and then accelerate

back to steady state in an orthogonal direction. Therefore, it represents the extreme case where printed structure can deviate from the intended pattern. We investigated the effects of a 90° change in print-head direction on a gel filament when printing below, at, and above the minimum speed associated with a particular flow rate. This was done in order to determine the degree of deviation from the intended pattern that occurs depending on printhead velocity. Extrusion occurred using flow rates of 10 mL/min for both alginate and calcium chloride, for which the established minimum printhead speed is 5.5 m/min. The printhead velocity was varied between 5, 5.5 and 20 m/min. It can be seen that an almost exact right-angled corner was created when operating at minimum speed (FIG. 2.9a). Printing below this speed resulted in an overshoot (FIG. 2.9b), while operation at very high speeds resulted in formation of a curved filament was (FIG. 2.9c). When printing occurred at the minimum allowable speed using a given flow rate, the resulting printed structure was similar to the designed pattern programmed into the g-code file. It can be seen that operating even slightly below the minimum speed lead to drastic deviations from the intended design, while printing at significantly higher speeds created constructs that remained comparable to the original design. This is due to the elastic quality of the material.

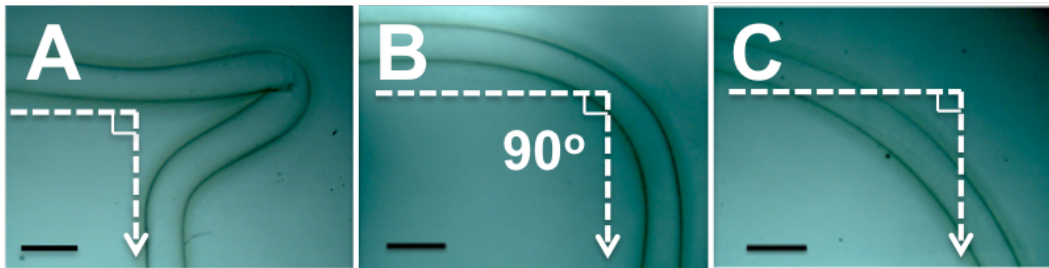


FIG. 2.9: Effect of printhead speed on a 90° change of orientation. Tubes are printed using a flow rate of 10mL/min at a speed of (A) 5 m/min, (B) 5.5 m/min (minimum speed), and (C) 20 m/min. Printing even slightly below the minimum speed (A), causes an overshoot to occur. At minimum speed (B), the tube forms a right angle when printing orientation is changed, while printing at higher speeds produces a curved tube (C). Dashed arrows indicate printhead motion path for intended filament extrusion. Scale bars, 2mm.

3.9 Printing cell-laden structures:

Vascular networks are composed of several types of vessels with varying architectures. However, all of these vessels have a common, inner endothelial cell layer that forms the central lumen. Umbilical veins are readily available and have been used for endothelial cell isolation for decades. Tissue engineering using human vein umbilical endothelial cells (HUVECs) currently represents the golden standard for endothelial cell based experiments [56].

Gel samples were printed using an inner and outer flowrate of 7 mL/min and at a printhead speed of 5 m/min, with cell concentrations of 1.5×10^6 cells/mL. FIG. 2.10b shows a cross-section of the printed cell-laden structure with an embedded hollow channel. An image of a single cell encapsulated within this gel can be seen in FIG. 2.10c. To illustrate the importance of nutrient diffusion for cells in a gel construct, images of channel-embedded constructs were compared to 1mm bulk gel layers that did not contain channels during a 3 day time period ($n = 5$). Samples were left under static conditions during this experiment. Fresh EBM media that VEGF was injected through the channels of perfused samples on each day. Both perfused and bulk constructs were submerged in media throughout the entire time period. Cell viability prior to printing was 100%. However, it has been found that viability decreases slightly following printing due to the shear forces associated with the extrusion process [57] and is expected to be lower than 100%. Results showed maintenance of HUVECs and higher viability for the perfused samples (FIG. 2.10d,e) as compared to the unperfused bulk gels (FIG. 2.10f,g). Quantitative analysis of cell viability within the fabricated samples is shown in FIG. 2.11. Hollow channel samples demonstrated good cell maintenance after 24 hrs and 72 hrs, with $81.4 \pm 14\%$ and $70.8 \pm 10.7\%$ viability respectively. However, non-vascularized samples exhibited a large decrease in cell viability during this time period, from $61.2 \pm 11.4\%$ to $20.4 \pm 5.4\%$. This result indicates that artificial 3D constructs fabricated using low concentration materials such as these could enhance the viability of cells seeded in them over long durations of time.

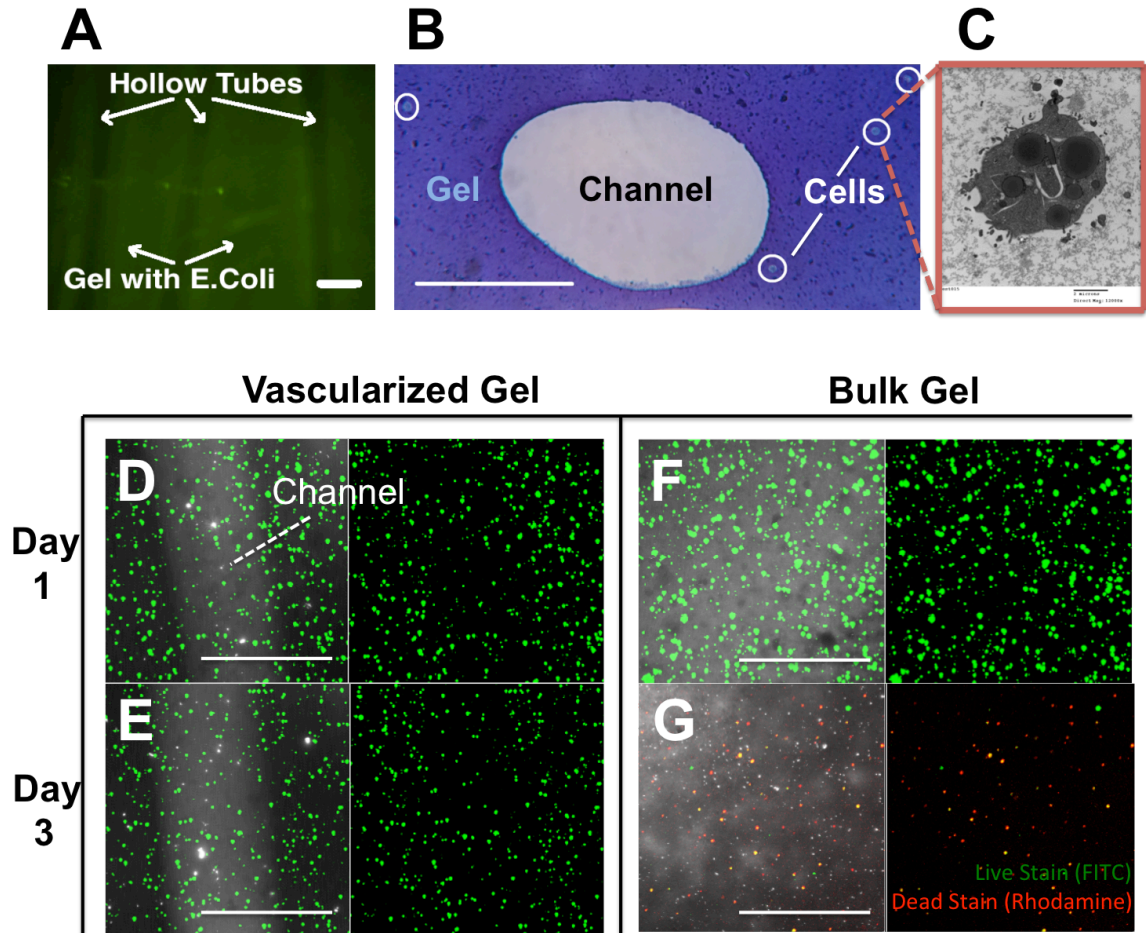


FIG. 2.10: (A) Gel layer with embedded hollow tubes, seeded with GFP Escherichia Coli K12. Scale bar, 2mm. (B) Cross-section of hollow channel embedded within HUVEC-laden gel. Scale, 500µm. (C) Cross-section of HUVEC embedded within gel. Cell organelles are visible. (D-G) Z-stack montages taken at intervals of 20µm, showing live/dead stain of gel constructs. Calcein indicates intracellular esterase activity by emitting green fluorescence, while ethidiumhomodimer is the red fluorophore indicative of plasma membrane integrity loss. (D, E) HUVEC-laden 3D printed gel constructs with embedded hollow channels, imaged on (D) Day 1 and (E) Day 3 post-printing. Constructs are printed at flow rates of 7mL/min at a printhead speed of 5m/min, and are re-perfused with media daily. (F, G) HUVEC-laden 1mm thick alginate gel layer on (F) Day 1 and (G) Day 3 post cell seeding. Scale bars, 1mm.

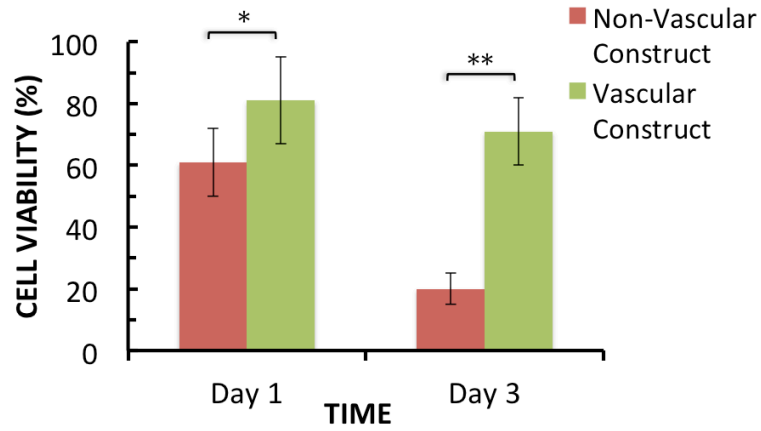


FIG. 2.11: Cell viability analysis over a 72hour time period. Fabricated hollow channel samples were compared to non-hollow alginate films cast at a 1mm thickness. Single asterisks (*) represent $p\text{-level} < 0.05$ and double asterisks (**) $p\text{-level} < 0.01$, indicating a significant difference between groups.

References

- [1] H. Bernstein, Ed., *Tissue Engineering in Regenerative Medicine*. New York: Springer, 2011.
- [2] J. L. Platt, “New directions for organ transplantation.,” *Nature*, vol. 392, no. 6679 Suppl, pp. 11–17, 1998.
- [3] M. Nakamura *et al.*, “Biocompatible inkjet printing technique for designed seeding of individual living cells.,” *Tissue Eng.*, vol. 11, no. 11–12, pp. 1658–1666, 2005.
- [4] T. Boland, T. Xu, B. Damon, and X. Cui, “Application of inkjet printing to tissue engineering.,” *Biotechnol. J.*, vol. 1, no. 9, pp. 910–917, 2006.
- [5] I. Zein, D. W. Hutmacher, K. C. Tan, and S. H. Teoh, “Fused deposition modeling of novel scaffold architectures for tissue engineering applications,” *Biomaterials*, vol. 23, no. 4, pp. 1169–1185, 2002.
- [6] M. Radisic, A. Marsano, R. Maidhof, Y. Wang, and G. Vunjak-Novakovic, “Cardiac Tissue Engineering using perfusion bioreactor systems,” *Nat. Protoc.*, vol. 3, no. 4, pp. 719–738, 2008.
- [7] L. Pan, Y. Ren, F. Cui, and Q. Xu, “Viability and differentiation of neural precursors on hyaluronic acid hydrogel scaffold,” *J. Neurosci. Res.*, vol. 87, no. 14, pp. 3207–3220, 2009.
- [8] A. Atala, S. B. Bauer, S. Soker, J. J. Yoo, and A. B. Retik, “Tissue-engineered autologous bladders for patients needing cystoplasty,” *Lancet*, vol. 367, no. 9518, pp. 1241–1246, 2006.
- [9] G. Matsumura, S. Miyagawa-Tomita, T. Shin’Oka, Y. Ikada, and H. Kurosawa, “First evidence that bone marrow cells contribute to the construction of tissue-engineered vascular autografts in vivo,” *Circulation*, vol. 108, no. 14, pp. 1729–1734, 2003.
- [10] B. Subramanian, D. Rudym, C. Cannizzaro, R. Perrone, J. Zhou, and D. L. Kaplan, “Tissue-engineered three-dimensional in vitro models for normal and diseased kidney.,” *Tissue Eng. Part A*, vol. 16, no. 9, pp. 2821–2831, 2010.
- [11] T. Xu *et al.*, “Hybrid printing of mechanically and biologically improved constructs for cartilage tissue engineering applications.,” *Biofabrication*, vol. 5, no. 1, p. 15001, 2013.
- [12] L. a Hockaday *et al.*, “Rapid 3D printing of anatomically accurate and mechanically heterogeneous aortic valve hydrogel scaffolds,” *Biofabrication*, vol. 4, no. 3, p. 35005, 2012.
- [13] M. S. Mannoer *et al.*, “3D printed bionic ears,” *Nano Lett.*, vol. 13, no. 6, pp. 2634–2639, 2013.
- [14] H. Bae *et al.*, “Building vascular networks.,” *Sci. Transl. Med.*, vol. 4, no. 160, p. 160ps23, 2012.
- [15] S. Kim, H. Lee, M. Chung, and N. L. Jeon, “Engineering of functional, perfusable 3D microvascular networks on a chip.,” *Lab Chip*, vol. 13, no. 8, pp. 1489–500, 2013.
- [16] C. Fidkowski, M. R. Kaazempur-Mofrad, J. Borenstein, J. P. Vacanti, R. Langer, and Y. Wang, “Endothelialized microvasculature based on a biodegradable elastomer.,” *Tissue Eng.*, vol. 11, no. 1–2, pp. 302–309, 2005.
- [17] V. Mironov, R. P. Visconti, V. Kasyanov, G. Forgacs, C. J. Drake, and R. R.

- Markwald, “Organ printing: Tissue spheroids as building blocks,” *Biomaterials*, vol. 30, no. 12, pp. 2164–2174, 2009.
- [18] K. Jakab *et al.*, “Tissue engineering by self-assembly of cells printed into topologically defined structures,” *Tissue Eng. Part A*, vol. 14, no. 3, pp. 413–421, 2008.
- [19] T. Boland, V. Mironov, A. Gutowska, E. a Roth, and R. R. Markwald, “Cell and organ printing 2: fusion of cell aggregates in three-dimensional gels,” *Anat. Rec. A. Discov. Mol. Cell. Evol. Biol.*, vol. 272, no. 2, pp. 497–502, 2003.
- [20] K. Jakab, B. Damon, A. Neagu, A. Kachurin, and G. Forgacs, “Three-dimensional tissue constructs built by bioprinting,” *Biorheology*, vol. 43, no. 3–4, pp. 509–513, 2006.
- [21] J. S. Miller *et al.*, “Rapid casting of patterned vascular networks for perfusable engineered three-dimensional tissues,” *Nat. Mater.*, vol. 11, no. 9, pp. 768–774, 2012.
- [22] L. E. Bertassoni *et al.*, “Hydrogel bioprinted microchannel networks for vascularization of tissue engineering constructs,” *Lab Chip*, vol. 14, no. 13, pp. 2202–11, 2014.
- [23] W. Lee *et al.*, “On-demand three-dimensional freeform fabrication of multi-layered hydrogel scaffold with fluidic channels,” *Biotechnol. Bioeng.*, vol. 105, no. 6, pp. 1178–1186, 2010.
- [24] V. K. Lee, A. M. Lanzi, H. Ngo, S. S. Yoo, P. a. Vincent, and G. Dai, “Generation of Multi-scale Vascular Network System Within 3D Hydrogel Using 3D Bioprinting Technology,” *Cell. Mol. Bioeng.*, 2014.
- [25] V. K. Lee *et al.*, “Creating perfused functional vascular channels using 3D bioprinting technology,” *Biomaterials*, vol. 35, no. 28, pp. 8092–8102, 2014.
- [26] Y. Zhang, Y. Yu, H. Chen, and I. T. Ozbolat, “Characterization of printable cellular micro-fluidic channels for tissue engineering,” *Biofabrication*, vol. 5, no. 2, p. 25004, 2013.
- [27] S. J. Shin *et al.*, “‘On the fly’ continuous generation of alginate fibers using a microfluidic device,” *Langmuir*, vol. 23, no. 17, pp. 9104–9108, 2007.
- [28] K. H. Lee, S. J. Shin, Y. Park, and S. H. Lee, “Synthesis of cell-laden alginate hollow fibers using microfluidic chips and microvascularized tissue-engineering applications,” *Small*, vol. 5, no. 11, pp. 1264–1268, 2009.
- [29] S. Beyer, T. Mohamed, and K. Walus, “A Microfluidics Based 3D Bioprinter with On-The-Fly Multimaterial Switching capability,” in *17th International Conference on Miniaturized Systems for Chemistry and Life Sciences*, 2013.
- [30] R. Attalla and P. Selvaganapathy, “3D Printing of Gels with Integrated Vascular Channels for Cell Culture using a Microfluidic Printhead,” in *18th International Conference on Miniaturized Systems for Chemistry and Life Sciences.*, 2014.
- [31] Y. Zhang, Y. Yu, A. Akkouch, A. Dababneh, F. Dolati, and I. T. Ozbolat, “In Vitro Study of Directly Bioprinted Perfusable Vasculature Conduits,” *Biomater. Sci.*, vol. 3, no. 1, pp. 134–143, 2015.
- [32] Q. Gao, Y. He, J. Fu, A. Liu, and L. Ma, “Coaxial nozzle-assisted 3D bioprinting with built-in microchannels for nutrients delivery,” *Biomaterials*, vol. 61, pp. 203–215, 2015.
- [33] Y. Chisti, “Hydrodynamic damage to animal cells,” *Crit. Rev. Biotechnol.*, vol.

- 21, no. 2, pp. 67–110, 2001.
- [34] P. Cheetham, K. Blunt, and C. Bucke, “Physical studies on cell immobilization using calcium alginate gels,” *Biotechnol. Bioeng.*, vol. XXI, no. 1979, pp. 2155–2168, 1979.
- [35] K. Y. Lee and D. J. Mooney, “Alginate: Properties and biomedical applications,” *Prog. Polym. Sci.*, vol. 37, no. 1, pp. 106–126, 2012.
- [36] C. K. Kuo and P. X. Ma, “Ionically crosslinked alginate hydrogels as scaffolds for tissue engineering: Part 1. Structure, gelation rate and mechanical properties,” *Biomaterials*, vol. 22, no. 6, pp. 511–521, 2001.
- [37] P.-T. Brun, B. Audoly, N. M. Ribe, T. S. Eaves, and J. R. Lister, “Liquid ropes: a geometrical model for thin viscous jets instabilities,” pp. 2–6, 2014.
- [38] A. Haug and O. Smidsrod, “Determination of Intrinsic Viscosity of Alginates,” *Acta Chem. Scand.*, vol. 16, no. 7, pp. 1569–1578, 1962.
- [39] V. W. Ostwald, “Ueber die rechnerische Darstellung des Strukturgebietes der Viskosität,” *Kolloid-Zeitschrift*, vol. 47, no. 2, pp. 176–187, 1928.
- [40] C. Tropea, A. Yarin, and J. Foss, Eds., *Springer handbook of experimental fluid mechanics*. Berlin: Springer Science & Business Media, 2007.
- [41] J. Berthier and P. Silberzan, Eds., *Microfluidics for biotechnology*, 2nd ed. Norwood: Artech House, 2010.
- [42] M. a LeRoux, F. Guilak, and L. a Setton, “Compressive and shear properties of alginate gel: Effects of sodium ions and alginate concentration,” *J. Biomed. Mater. Res.*, vol. 47, pp. 46–53, 1999.
- [43] T. a. Becker and D. R. Kipke, “Flow properties of liquid calcium alginate polymer injected through medical microcatheters for endovascular embolization,” *J. Biomed. Mater. Res.*, vol. 61, no. 4, pp. 533–540, 2002.
- [44] D. Rees, “Shapely Polysaccharides,” *Biochem. J.*, vol. 126, no. 2, pp. 257–273, 1972.
- [45] R. Kohn, “Ion Binding on Polyuronates-Alginate and Pectin,” *Biochem. J.*, vol. 126, no. 2, pp. 371–397, 1972.
- [46] S. Moe, G. Skjak-Braek, O. Smidsrod, and H. Ichijo, “Calcium alginate gel fibers : influence of alginate source and gel structure on fiber strength,” *J. Appl. Polym. Sci.*, vol. 51, no. 10, pp. 1771–1775, 1994.
- [47] I. Fernandez Farrés and I. T. Norton, “Formation kinetics and rheology of alginate fluid gels produced by in-situ calcium release,” *Food Hydrocoll.*, vol. 40, pp. 76–84, 2014.
- [48] A. B. Metzner and J. C. Reed, “Flow of Non-Newtonian Fluids-Correlation of the Laminar , Transition , and Turbulent-flow Regions,” *AIChE J.*, no. 4, pp. 434–440, 1955.
- [49] J. O. Cruickshank and B. R. Munson, “Viscous fluid buckling of plane and axisymmetric jets,” *J. Fluid Mech.*, vol. 113, no. 1, p. 221, 1981.
- [50] J. O. Cruickshank, “Low-Reynolds-number instabilities in stagnating jet flows,” *J. Fluid Mech.*, vol. 193, no. 1, p. 111, 1988.
- [51] T. Majmudar, M. Varagnat, W. Hartt, and G. McKinley, “Nonlinear Dynamics of Coiling in Viscoelastic Jets,” 2010.
- [52] A. Jeanes, J. E. Pittsley, and F. R. Senti, “Polysaccharide B-1459: A new hydrocolloid polyelectrolyte produced from glucose by bacterial fermentation,” *J.*

- Appl. Polym. Sci.*, vol. 5, no. 17, pp. 519–526, 1961.
- [53] O. Cakmak *et al.*, “Microcantilever based disposable viscosity sensor for serum and blood plasma measurements,” *Methods*, vol. 63, no. 3, pp. 225–232, 2013.
- [54] C. Wang, B. M. Baker, C. S. Chen, and M. A. Schwartz, “Endothelial cell sensing of flow direction,” *Arterioscler. Thromb. Vasc. Biol.*, vol. 33, no. 9, pp. 2130–2136, 2013.
- [55] T. Barnes, A. Shulman, A. Farone, M. Farone, and D. Erenso, “Assessment of the Elasticity of Erythrocytes in Different Physiological Fluids by Laser Traps,” *Opt. Photonics J.*, vol. 3, no. 2, pp. 211–216, 2013.
- [56] S. Baiguera and D. Ribatti, “Endothelialization approaches for viable engineered tissues,” *Angiogenesis*, vol. 16, no. 1, pp. 1–14, 2013.
- [57] Y. Yu, Y. Zhang, J. a Martin, and I. T. Ozbolat, “Evaluation of cell viability and functionality in vessel-like bioprintable cell-laden tubular channels.,” *J. Biomech. Eng.*, vol. 135, no. 9, p. 91011, 2013.

Chapter 3

3D BIOPRINTING OF HETEROGENEOUS BI- AND TRI-LAYERED HOLLOW CHANNELS WITHIN GEL SCAFFOLDS USING SCALABLE MULTI-AXIAL MICROFLUIDIC EXTRUSION NOZZLE

Complete citation:

Rana Attalla, Erin Puersten, Nidhi Jain and Ponnambalam R Selvaganapathy. “*3D Bioprinting of Heterogeneous Bi- and Tri-layered Hollow Structures inside Gel Layers using Multi-Axial Microfluidic Extrusion Nozzle.*” This paper is in preparation for submission.

Relative Contributions:

Attalla, R: Designed and performed experiments including sample printing, cell-laden gel fabrication, and imaging. Interpreted and analyzed the resulting data, and wrote the manuscript.

Puersten, E: Assisted in performing characterization experiments, imaging, and cell-laden sample printing.

Jain, N: Assisted with biological cell culture and maintenance.

1. Introduction

There is a tremendous need for the integration of artificially engineered blood vessels and vascular networks into cell-laden scaffolds that serve as templates to guide the formation of new tissue. Recent work has focused on fabrication of hollow constructs by means of 3D printing [1–5], sacrificial moulding [6–9], or planar processing [10–13]. However, many of these tissue engineering approaches focus only on creating a single-layered endothelium, and still lack the ability to fabricate perfusable conduit-like constructs composed of multi-layered vascular walls. In reality, biological veins and arteries consist of several layers of various cell types and extracellular matrices [14]. Therefore, it is important to develop systems with increased control over cellular and material alignment such that multiple cell types and matrices can be printed in close proximity to one another. This allows for the creation of complex hierarchical architectures integrated within the artificially fabricated tissues.

To address this technical challenge, some research groups have demonstrated the ability to create bi- or tri-layered hollow channel structures using various strategies. One such method involved loading of smooth muscles cells and endothelial cells onto separate fibrous substrates, and subsequently stacking then rolling these two layers around a surgical suture in order to create a bilayered blood vessel-like construct [15]. In a similar manner, another group also utilized a cylindrical mold to form a silk-based bilayered tubular scaffold by means of a combined weaving and dip-coating technique [16]. However, both of these methodologies require long, tedious processes as well have limited scalability in that only two concentric layers may be fabricated. Alternatively, successful fabrication of a tri-layered vascular structure by using a microfluidic device with an embedded glass channel as a mold, has been demonstrated [17]. Cell-laden biomaterials are manually pipetted into the mold to form three concentric layers that shape the blood vessel. This sort of strategy as well as the two previously described methods are only suitable for producing singular vascular grafts, but cannot be used to create larger 3D tissues with embedded complex channel networks. As a result, some methods have combined sacrificial molding and 3D bioprinting in order to integrate bi-layered hollow channel networks into thicker 3D matrices [18,19]. However, these

existing techniques require time consuming, multi-step processes involved in laying down supporting materials and removal of sacrificial spacers. In many cases, the current approaches also lack versatility in creating heterogeneous multi-layered structures, thereby limiting the material complexity necessary to facilitate a successful and viable multi-cellular strategy.

In order to address these limitations, we have developed a microfluidic nozzle design that allows multi-axial extrusion of hydrogels in order to 3D print bi- and tri-layered hollow conduits for use in vascular tissue engineering applications. We demonstrate, for the first time, the ability to bioprint 3D gel matrices with embedded hollow channels networks that are composed of hierarchal concentric layers. These concentric layers can contain distinctly different biocompatible materials or biological cells in order to realize more complex tissue architectures. We demonstrate successful printing of an inner layer containing endothelial cells and a surrounding layer of supporting fibroblast cells, thereby demonstrating our system's increased control of material and cellular alignment in 3D. With our strategy, we are able to incorporate a variety of biocompatible materials in order to successfully improve cell adhesion and increase cell viability. Our automated, low-cost 3D bioprinting method allows us to precisely pattern and fabricate a wide range of conduit dimensions in a fast and simple fashion. Additionally, we clearly identify the operational printing range at variable flow rates and material concentrations. Our device design allows for versatility in material incorporation, scalability to include multiple concentric layers, and produces hierarchal structures that can be printed either in tubular form or as thick, multilayered gel films with integrated channels. This tissue engineering technique has strong potential to be used in the creation of artificial veins and arteries, which consist of various layers of different cells and extracellular matrices.

2. Methods and Materials

2.1 Extrusion device and setup:

We have previously demonstrated the use of a low-cost open source 3D printer for 3D biofabrication of hollow channels using a custom-made coaxial nozzle [6]. However, that technique lacked the ability to create hierarchal structures with concentric layers that would better mimic the complex architecture found in true biological conduits. In this work, we use a similar open-source printer (RepRap Ormerod) (FIG. 3.1a) and modify it to include a multi-axial extrusion nozzle that allows us to create these complex hierarchal constructs. Our nozzle was fabricated using the soft lithographic approach by mold casting of polydimethylsiloxane (PDMS) in a 3D printed mold followed by oxygen plasma bonding, in a manner similar to that previously described [6].

The nozzle device consisted of a winding 2mm hollow channel with embedded needles of varying sizes. The needles were placed through corresponding tracks that were precisely sized to match the needle gage and led down to the center of the hollow channel (FIG. 3.1b). A custom, 3D printed bracket was used to stabilize and center the embedded needles in their respective tracks during printing in order to ensure that proper alignment was maintained (FIG. 3.1c). The needle gages increased in size from the innermost to outermost flow, thereby allowing the formation of progressively larger concentric layers encapsulating one another in order to create a hierarchal conduit structure. In a tri-axial setup (FIG. 3.1b), a 2mm hollow channel PDMS device was used. It contained a 26-gage flat-tip needle (0.26mm and 0.47mm inner and outer diameter respectively) that was used for the inner-most flow, followed by a 20gage needle (0.63mm and 0.91mm inner and outer diameter respectively) used for the next concentric flow such that one co-flowing stream was embedded within the next and there was no interference between them. When the device was scaled up to allow for multi-axial extrusion (FIG. 3.1c), a third 18-gage needle (0.83mm and 1.27mm inner and outer diameter respectively) was used in order to produce an additional concentric layer. In this case, the PDMS nozzle device was also modified to contain a 3mm winding hollow channel instead, such that the channel was large enough to accommodate the additional flows. This custom extrusion platform is

highly scalable as it can easily accommodate any number of flows by incorporating additional needles and bends to the PDMS channel.

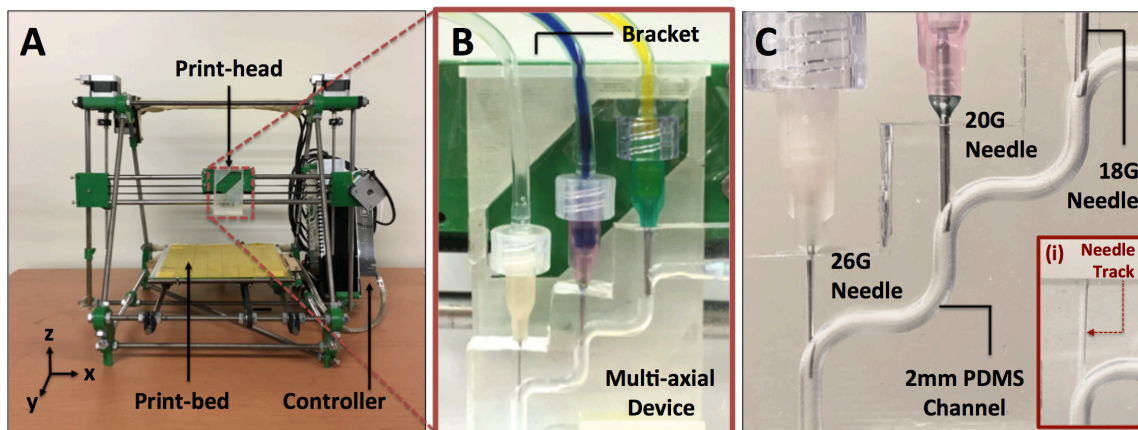


FIG. 3.1: A) A low-cost, open source 3D printer (RepRap Ormerod) that has been modified by removing the original nozzle and replacing it with a custom, microfluidic nozzle. B) Scalable design allows incorporation of multi-axial extrusion. A 3D printed bracket was used to stabilize the embedded needles during printing in order to maintain proper alignment. C) Custom-made tri-axial PDMS nozzle. Patterned channel is 2mm in diameter. Patterned needle tracks are used to guide the needles to the center of the channel, as shown in (i).

2.2 Extrusion mechanism:

In our microfluidic printhead, the 26 gage flat-tip needle was used for the inner flow of calcium chloride (100mM, Fisher Scientific), which acted as the crosslinker. The 20 gage needle was used to flow the uncrosslinked constituent of the inner gel layer (alginate (2%w/v, Sigma-Aldrich) stained with blue dye), while the 2mm hollow PDMS channel in which the needles were embedded was used to flow the uncrosslinked constituent of the outermost gel layer (alginate stained with yellow dye) (FIG. 3.2a). Diffusion of calcium ions from the central flow into the surrounding alginate flows caused gelation to occur and a hollow tube to be formed (FIG. 3.2b). As the hollow tube continued to gel upon extrusion, it was printed directly onto a dry substrate using the aforementioned RepRap Printer. The xyz positioning system of the printer allowed the hollow tubes to be precisely patterned onto the printbed. It should be noted that the outermost layer was not completely gelled as it exited the nozzle of the printer. It

therefore spread on the dry substrate and merged with the adjacent layer before it slowly crosslinked by the diffusion of the crosslinker from the lumen of the channel.

In order to allow visual differentiation between the concentric layers, the inner and outer alginate flow were dyed different colours (FIG. 3.2a). Fluorescein (500 μ g/mL, Fluka) and methylene blue (500 μ g/mL, Sigma-Aldrich) were used for the inner and outer alginate flows respectively. These dyes have limited solubility in alginate solutions and aggregate into particles, which limits their diffusion across layers, making them ideal for visualization. FIG. 3.2b shows an example of an extruded hollow tube on a dry substrate, with the concentric alginate gel layers that are clearly differentiated from one another.

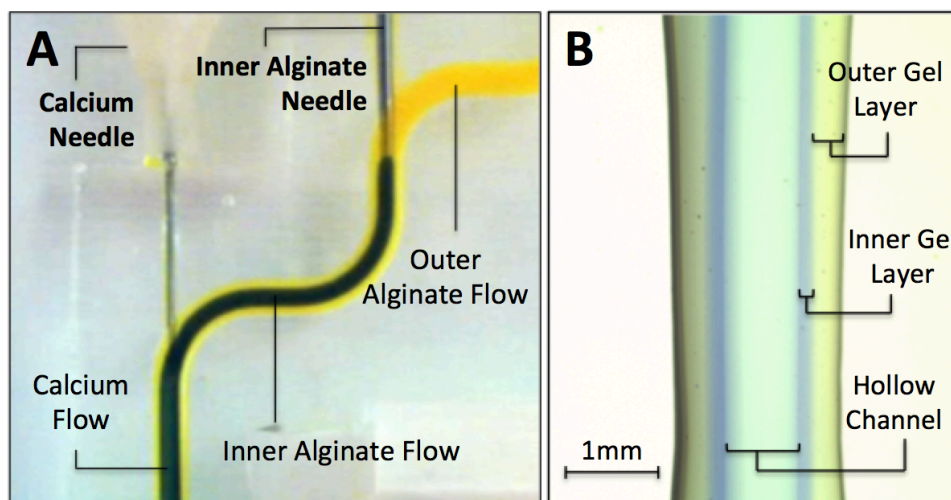


FIG. 3.2: A) Triaxial extrusion of calcium and alginate flows. Dyed solutions allow visual differentiation between the hierarchical layers. The inner alginate flow (blue) and outer alginate flow (yellow) can be seen, while the calcium flow is left un-coloured. B) A hollow gel tube is produced upon extrusion, and the separate concentric layers can be clearly distinguished from one another.

2.3 Cell culture:

Human umbilical vein endothelial cells (HUVEC) (Lonza Inc.) transfected with red fluorescent protein (RFP) were used. Endothelial basal media (EBM) (Lonza Inc.) was supplemented with fetal bovine serum (FBS), vein endothelial growth factor (VEGF), hydrocortisone, ascorbic acid, heparin, and gentamicin (GA-1000). Mouse 3T3 fibroblasts (ATCC) transfected with green fluorescent protein (GFP) were also cultured according to standard protocols. Dulbecco's Modified Eagle Medium (DMEM) (Sigma)

completed with 10% fetal bovine serum (FBS) (Thermofisher) and 1% penicillin streptomycin (Thermofisher) was used to make media changes to cell culture until 100% confluency was achieved. Cells were harvested using 0.25% Trypsin-EDTA and the cell suspension was diluted accordingly to create the required cell concentrations, followed by mixing into the uncrosslinked hydrogel solutions. Experiments were done using cell concentrations of 2×10^6 cells/mL.

2.4 Cell-Laden gel printing and imaging:

Alginate and calcium chloride solutions were made at 2%w/v and 0.1M respectively in sterilized water, and the cell suspension was mixed in with the sodium alginate solution prior to printing. In the case of multi-material printing, collagen (5mg/mL, Santa Cruz Biotechnology) and fibrinogen (50mg/mL, Sigma-Aldrich) were used alongside 2.5% w/v alginate. First, printing of an alginate-collagen composite was performed by extruding a central core of calcium chloride (0.1M), an inner gel layer of alginate (2.5% w/v), and an outer layer of alginate-collagen mix (0.5% w/v and 2.5mg/mL final concentration each, respectively). Collagen was neutralized using with 20 μ L/mL of sodium hydroxide (1N, Fisher Scientific) in order to facilitate slow gelation (approx. 30 minutes), and then immediately mixed with alginate. In the second multi-material printing strategy, central core and outer gel concentrations remained the same as previously described with alginate-collagen composites. The outer gel layer, however, consisted of an alginate-fibrinogen mix (1% w/v and 25mg/mL final concentration each, respectively). A higher concentration for alginate was used to compensate for the low viscosity of fibrinogen, as it was not crosslinked to form a fibrin gel until after printing. Crosslinking prior to printing (whether by means of pre-mixing or introducing thrombin into the central core flow alongside the calcium) was found to cause consistent clogging of the nozzle. Therefore, the alginate-fibrinogen samples were soaked in thrombin (250U/mL, Sigma-Aldrich) post-printing for 30min, thereby forming alginate-fibrin gels. The alginate in alginate-fibrin samples was dissolved by soaking the samples in sodium citrate (4% w/v, Sigma-Aldrich) for 20 minutes and then washing with Dulbecco's Phosphate Buffered Saline (Sigma-Aldrich). This procedure was not done for alginate-collagen constructs, as the samples were found to disintegrate and destabilize due to weak

mechanical stiffness associated with low concentration. To avoid this, attempts were made to print higher concentrations of collagen. However, printing with higher concentrations of collagen proved futile as it resulted in consistent clogging of the nozzle, in a manner similar to that of printing fibrin that had been crosslinked prior to printing. Because collagen requires pre-mixing in order to crosslink, this could not be avoided.

Printing procedures were carried out using the extrusion mechanism previously described in order to create cell laden gel structures. Printed hollow channels that contained multiple cell types (heterogeneous co-culture) were perfused with completed EBM that had been supplemented with 10% FBS in order to maintain the viability of both cell types within the construct over a period of 72 hours. Structures that contained only HUVECs were maintained in regular EBM media. Samples were incubated at 37°C and 5% carbon dioxide. Re-perfusion and media changes were made daily. Live stain images of printed samples were taken using an inverted brightfield and fluorescence microscope (IX51, Olympus).

3. Results and Discussion

3.1 Fabrication of 3D structures:

With our technique, we demonstrated the ability to fabricate 3D structures to be used in tissue engineering applications. We were able to form either heterogeneous hollow gel tubes (FIG. 3.3a), as well as solid, single-layer (FIG. 3.3b) or multi-layer (FIG. 3.3c) scaffolds that have integrated hollow perfusion channels in them by printing the tubes close enough to one another that the outer gel layers were able to merge. The calcium in the lumen of the hollow channels caused alginate to crosslink immediately in its vicinity, which resulted in the instantaneous formation of a solid gel shell at the diffusion interface [20,21]. This shell also limited the degree to which calcium ions were able to permeate, thereby slowing the entire crosslinking process. Because there were several concentric layers of alginate being extruded, the calcium ions were not able to diffuse and penetrate through all the layers quickly enough for complete gelation to occur prior to deposition [6]. This caused lateral spreading of the outermost uncrosslinked

layers to occur upon deposition, and led to fusion between one parallel hollow tube to the next, thereby creating a solid gel layer (1.5-2.25mm thickness depending on flow rate and printspeeds) with embedded hollow channels. With our triaxial extrusion device, we were able to create a distinct second embedded gel layer surrounding those hollow channels, which allowed us the opportunity to increase the material and cellular complexity of our 3D structures.

The microfluidic nozzle design allows for scalability in the number of additional concentric layers by incorporating multiple needles. It also allows for a wide range of achievable hollow channel and gel layer dimensions by simple alterations to the 3D mold or needle diameters. FIG. 3.3d shows a scaled up version of the nozzle device that allows multi-axial extrusion. A new PDMS device was fabricated to contain a 3mm winding hollow channel (previously 2mm) in order to accommodate the additional concentric flows and prevent any interference or instability from occurring. An additional embedded needle (18 gage) was incorporated into the device, which allowed us to produce 3 concentric alginate gel layers and a hollow calcium core (FIG. 3.3d). Our device is also versatile in its ability to create various types of conduit-like structures. For example, it can even be used to create non-hollow solid fibres with multiple encased gel layers (FIG. 3.3e). This was simply done by extruding both a central and surrounding flow of alginate directly onto a moistened hydrophilic polycarbonate substrate (Sterlitech) that has been coated in calcium chloride solution. The calcium chloride caused the deposited fiber to immediately solidify and resulted in the production of solid bi-layered wires. Our tri-axial strategy allows us to create gel structures with multiple hierarchal layers that can be laden with various cell types or other biocompatible extracellular matrices, thereby serving as complex tissue engineering scaffolds.

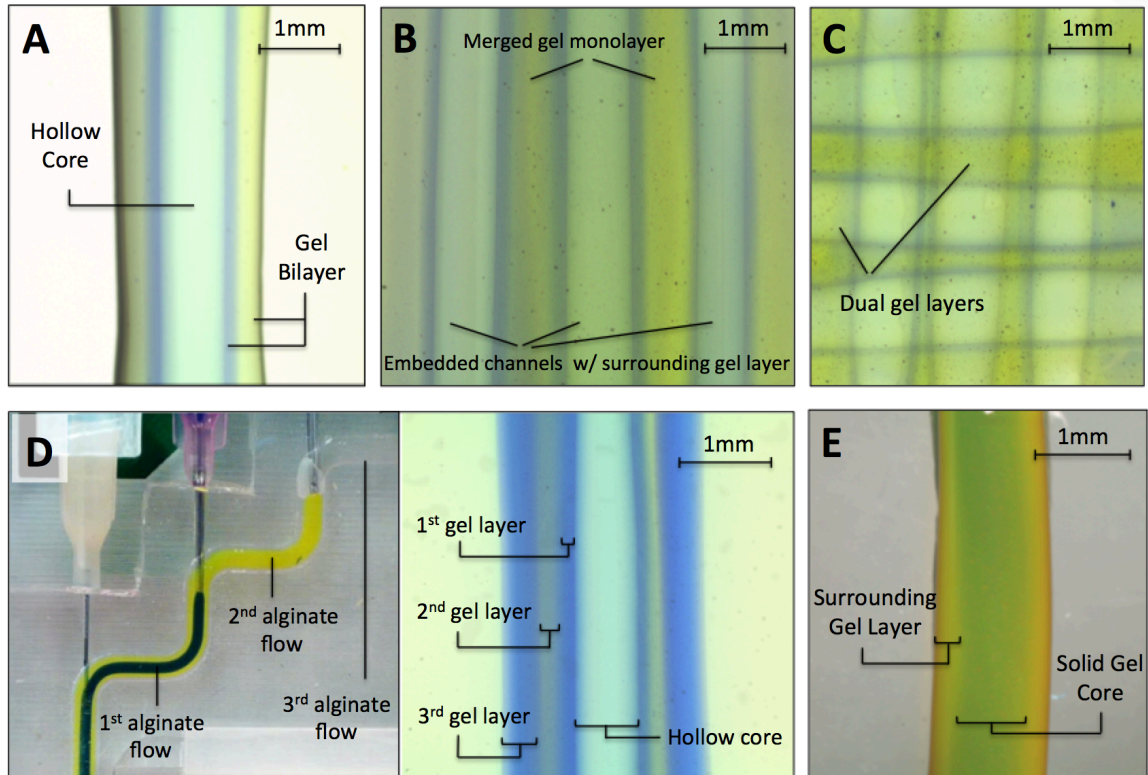


FIG. 3.3: 3D fabrication of hydrogel scaffolds. A) Triaxial extrusion of a bilayered conduit that has been deposited onto a dry substrate. When the conduits are patterned in close proximity to one another, the outer uncrosslinked gel layers of adjacent, parallel tubes fuse together and result in a solid B) single-layer (~1.6mm thickness) or C) multi-layered gel film (~3.2mm thickness) being formed with embedded hollow channels. D) Modification of the scalable microfluidic nozzle design allows multi-axial extrusion that can be used to create conduits with multiple distinct gel layers and a hollow core. Up to three concentric gel layers surrounding the hollow core can be seen in (D). E) Versatility of the device allows it to be successfully used for creating and patterning solid fibers with several concentric gel layers.

3.2 Characterization of triaxial printing:

It is important to characterize the printable working range of this device and extrusion mechanism in order to determine the operational range, obtain optimal results and ensure that ideal scaffold architectures are obtained. The system was characterized in terms of calcium flow (hollow core), inner alginate flow (gel layer 1), outer alginate flow (gel layer 2), and the printspeed (traverse of the printhead) in order to determine the operational printing range (represented by the green region in FIG. 3.5). Each of the flow

rates were varied from 1 – 6mL/min and the printspeed was varied from 1 – 16m/min. Extruded tubes must demonstrate the following three requirements in order to be categorized under the viable printing range (FIG. 3.4a): 1) precisely follow the required printing pattern and show good alignment, 2) produce distinctly different concentric layers of alginate gel that can be easily visualized, and 3) contain a hollow, perfusable core. It was necessary to accurately match the extrusion velocity of the hollow tubes to velocity of the moving print-head in order to ensure that these conditions were met. We refer to this velocity as the optimal printing speed. The corresponding optimal printing speed (in m/min) for each set of flow rates within the viable printing range was determined, as is indicated by the values reported on each point in the green region of the graphs in FIG. 3.5. As expected, the required optimal printing speed increased as the extrusion flow rates for calcium or alginate increased as well. However, if the extrusion velocity superseded the maximum possible printspeed (16m/min) of the printer, it resulted in flow instabilities and patterning irregularities (FIG. 3.4b). The black region of the FIG. 3.5 graphs is representative of this phenomenon. When the printspeed was greater than the extrusion velocity, it caused stretching of the hollow channel and surrounding gel layers as is discussed in detail in *Section 3.3*.

We found that at high alginate flow rates and low calcium flow rates, inadequate crosslinking occurred due to the drastic increase in ratio of alginate volume to calcium. We found that this insufficient crosslinking occurred when the total inner and outer alginate flow rate (Q_i and Q_o respectively) was greater than three times the calcium flow rate (Q_c) – that is, $Q_i + Q_o > 3Q_c$. This is supported by previous work that has confirmed longer gelation times are required at higher alginate flow rates and lower calcium flow rates [9]. It is because the calcium ions cannot sufficiently diffuse through all the layers of alginate, which results in a narrow, gelled inner core and a large amount of uncrosslinked solution on the periphery [20,21]. The ungelled material caused blotting to occur during the printing process, as well as a significant amount of mixing between concentric layers (FIG. 3.4c). Therefore, it was expected that greater jet instability would occur at higher alginate flow rates. We observed this behaviour in our experimental results, as blotting and insufficient crosslinking became inevitable at higher alginate flow rates (as is indicated by the yellow region in the graphs in FIG. 3.5).

Another region of non-viable printing occurred when the relative flow rates of calcium, inner alginate and outer alginate were not able to produce concentric, triaxial layers (FIG. 3.4d). The occurrence of this non-triaxial extrusion (which is represented by the orange region in FIG. 3.5) indicates that the inner alginate flow has reached either a maximum or minimum shell thickness. This shell thickness is dependent on a number of factors, including imposed flow velocity, and flow rates of surrounding fluids [22–24]. It has been found that this gel layer thickness increases when its imposed flow rate increases, but decreases when the surrounding fluid flow rate is higher than its imposed flow rate [25], which corresponds well with our findings. An inner alginate flow rate that is significantly higher than the outer alginate flow causes the inner alginate shell to approach its maximum diameter. In FIG. 3.4d(i), the blue inner alginate stream in the nozzle can be seen approaching the boundaries of the PDMS channel wall and the yellow outer alginate flow can no longer be visualized. This means that the inner alginate shell reached a maximum diameter of 2mm (i.e. the diameter of the nozzle channel that it is constricted by). The inner alginate shell became larger than the diameter of the outer alginate, which resulted in non-triaxial extrusion since a distinct boundary between the two alginate layers could not be observed (FIG. 3.4d(i)). On the other hand, when the calcium and outer alginate flow rates are significantly higher than the inner alginate flow rate, the inner flow approaches its minimum diameter. Inside the PDMS channel, the inner alginate shell became smaller than the calcium core, and this resulted in a flow instability between the two adjacent streams that is not suitable for producing a hollow core (FIG. 3.4d(ii)). The minimum diameter of the inner alginate shell was found to occur when the ratio of inner alginate flow rate to calcium and outer alginate combined flow rates was 1:10 or greater (i.e. $10Q_i \leq Q_c + Q_o$).

Printing using lower flow rates of both inner and outer alginate relative to the calcium flow rate resulted in consistent clogging of the device, and was therefore not operational. This can likely be attributed to non-triaxial extrusion as well, as a result of instability that occurs when the diameter of the alginate sheath flow is significantly smaller than the calcium core. We found that clogging generally occurred when the total alginate flow rate is less than or equal to the calcium flow rate (i.e. $Q_i + Q_o \leq Q_c$).

Mapping of the triaxial printing range allowed us to determine the boundaries for achieving optimal hollow channel fabrication. Because operating at a calcium flow rate of 3mL/min provided the largest viable printing range, we continued to use this flow rate to conduct further experiments in the next section – specifically to investigate the effects of material concentration on the printing range.

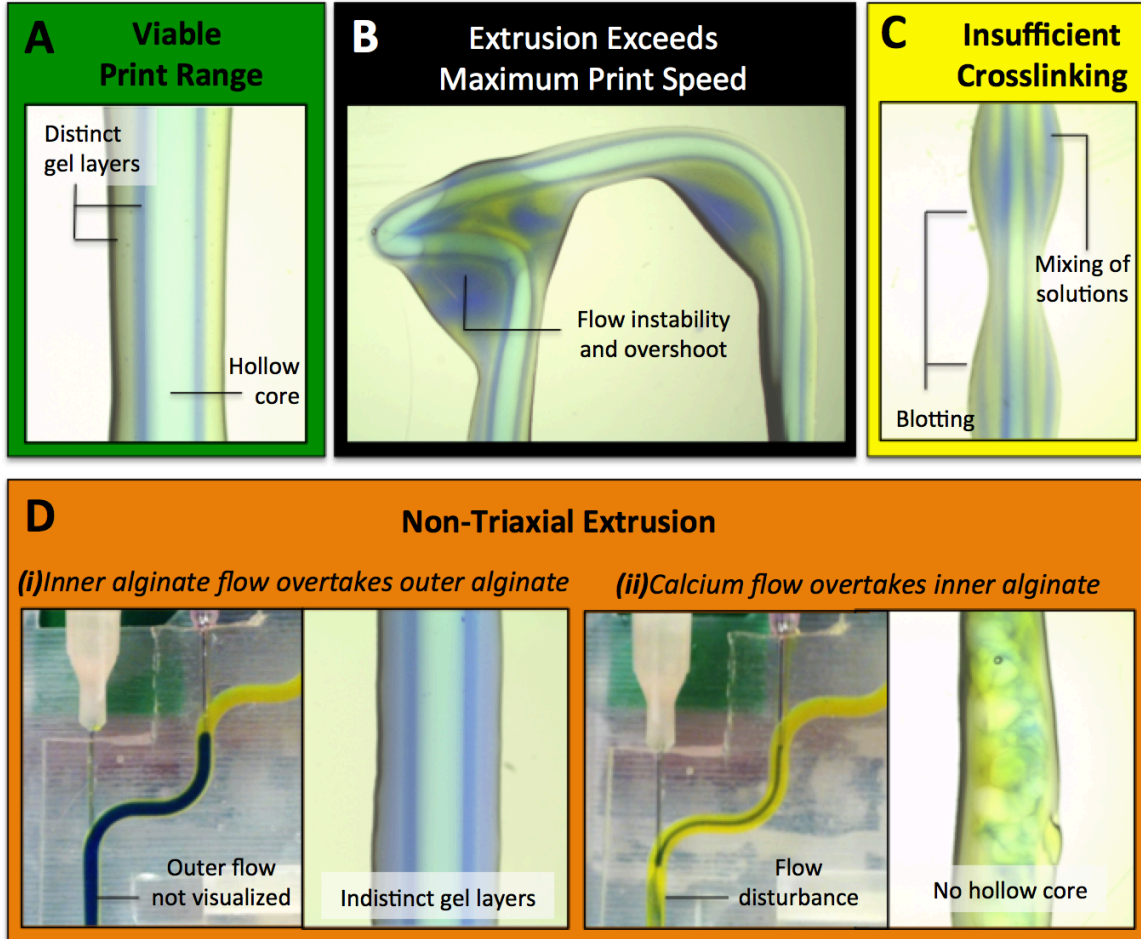


FIG. 3.4: Representative images for each condition within the printing range. A) Printing within the operational range at the optimal printspeed produces viable, well aligned tubes with distinct concentric gel layers and a hollow core. B) When the extrusion velocity of the hollow tube increase beyond the maximum speed of the printer (black) flow instabilities occur. C) Increased alginate flow rates relative to calcium flow results in insufficient crosslinking of outer-most layers (yellow) and leads to blotting or mixing of solutions during printing. D) (i)An inner alginate flow that is significantly greater than the outer alginate flow does not produce distinct gel layers due to the outer flow being overtaken by the inner flow. (ii)At higher calcium flow rates, an inner alginate flow that is significantly lower than the calcium flow rate results in flow instabilities and is not suitable for producing a hollow core.

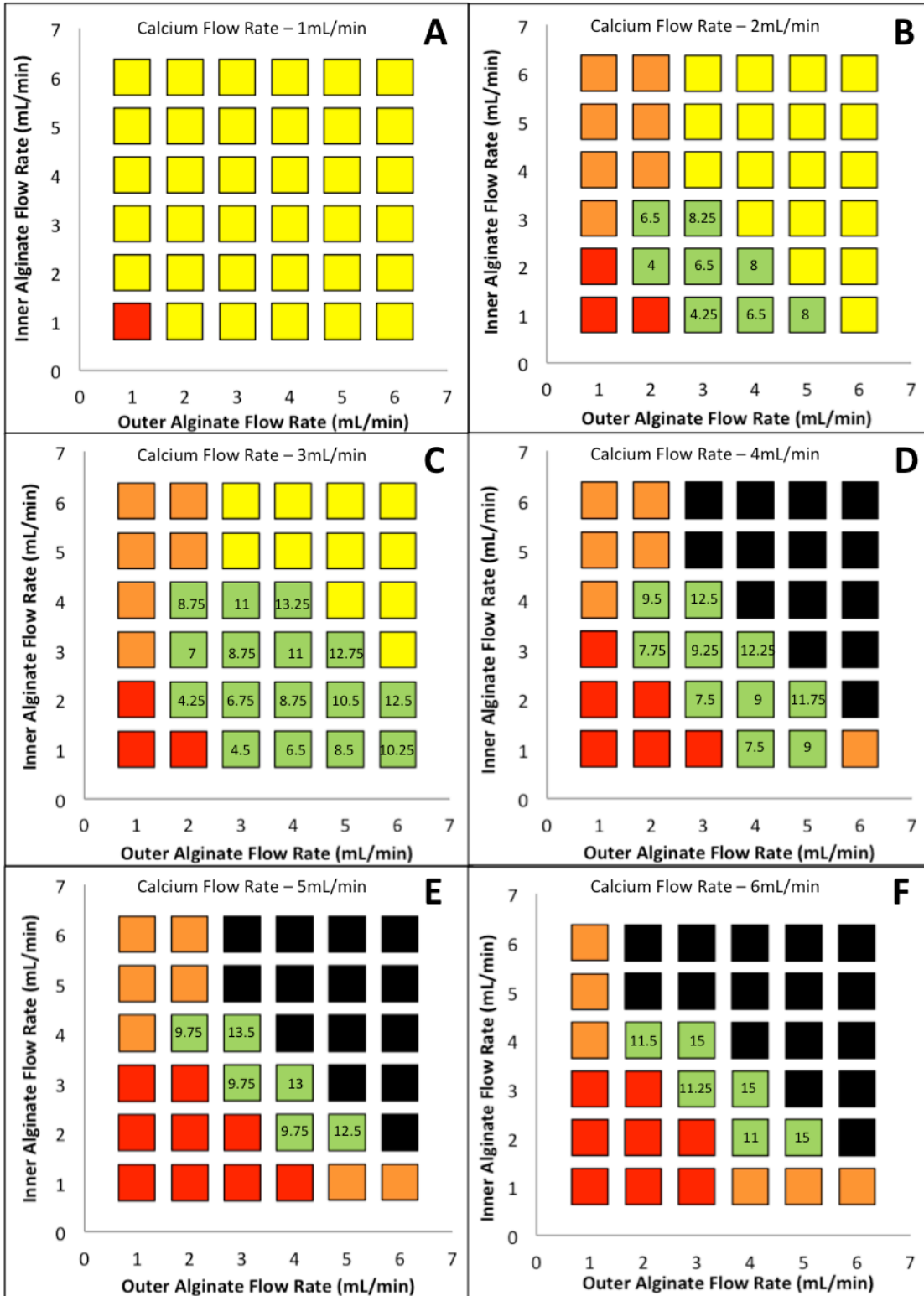
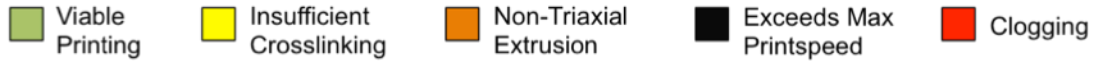


FIG. 3.5: Mapping of the dynamic printing range of the tri-axial extrusion device. All flow rates are varied between 1-6mL/min. Each graph represents a different calcium flow rate – graphs A) to F) represent calcium flow rates of 1 to 6mL/min respectively. Printing within the operational range (green) at the optimal required printspeed (indicated in m/min on each point in the operational range) produces viable, well aligned tubes with distinct concentric gel layers. All other mapped regions are non-operational due to clogging, insufficient crosslinking, non-triaxial extrusion, or surpassing the printspeed threshold. Low alginate flow rates cause consistent clogging of the microfluidic nozzle (red). Insufficient crosslinking (yellow) occurs due to high alginate to calcium volume ratios. Non-triaxial extrusion (orange) is a result of an inner alginate flow that is significantly less than the calcium flow, or an inner alginate flow that is significantly greater than the outer alginate flow. If gel extrusion velocity is greater than the maximum printspeed threshold (16m/min), flow instabilities occur.

3.3 Effect of alginate and calcium concentration on printing:

Changes to material concentrations can have a large impact on printing viability. Printing tests were performed in order to determine the operational range of alginate or calcium concentrations for viable printing. All tests were performed at a constant calcium flow rate of 3mL/min. First, the concentration of calcium chloride was tested at 25mM (concentrations lower than this could not be printed) and 175mM, while alginate concentration was maintained at 2% (FIG. 3.6a,b). As expected, the viable printing range was reduced significantly at 25mM in comparison to 100mM (as was used in the previous section) and was extended when a concentration of 175mM was used. This was due to the high concentration gradient of calcium between the inner lumen and the alginate layers, which caused faster diffusion of the ions and accelerated formation of a solid annular shell [26]. This enhanced the intermolecular interactions and reduced the range of insufficient crosslinking. However, the increased diffusion and crosslinking also caused increased clogging at lower alginate flow rates. At low flow rates, the alginate streams passed through the nozzle channel more slowly, which allowed a longer time period for gelation to occur. Therefore, the rapidly solidified gel layers aggregated too quickly and led to clogging at the nozzle orifice.

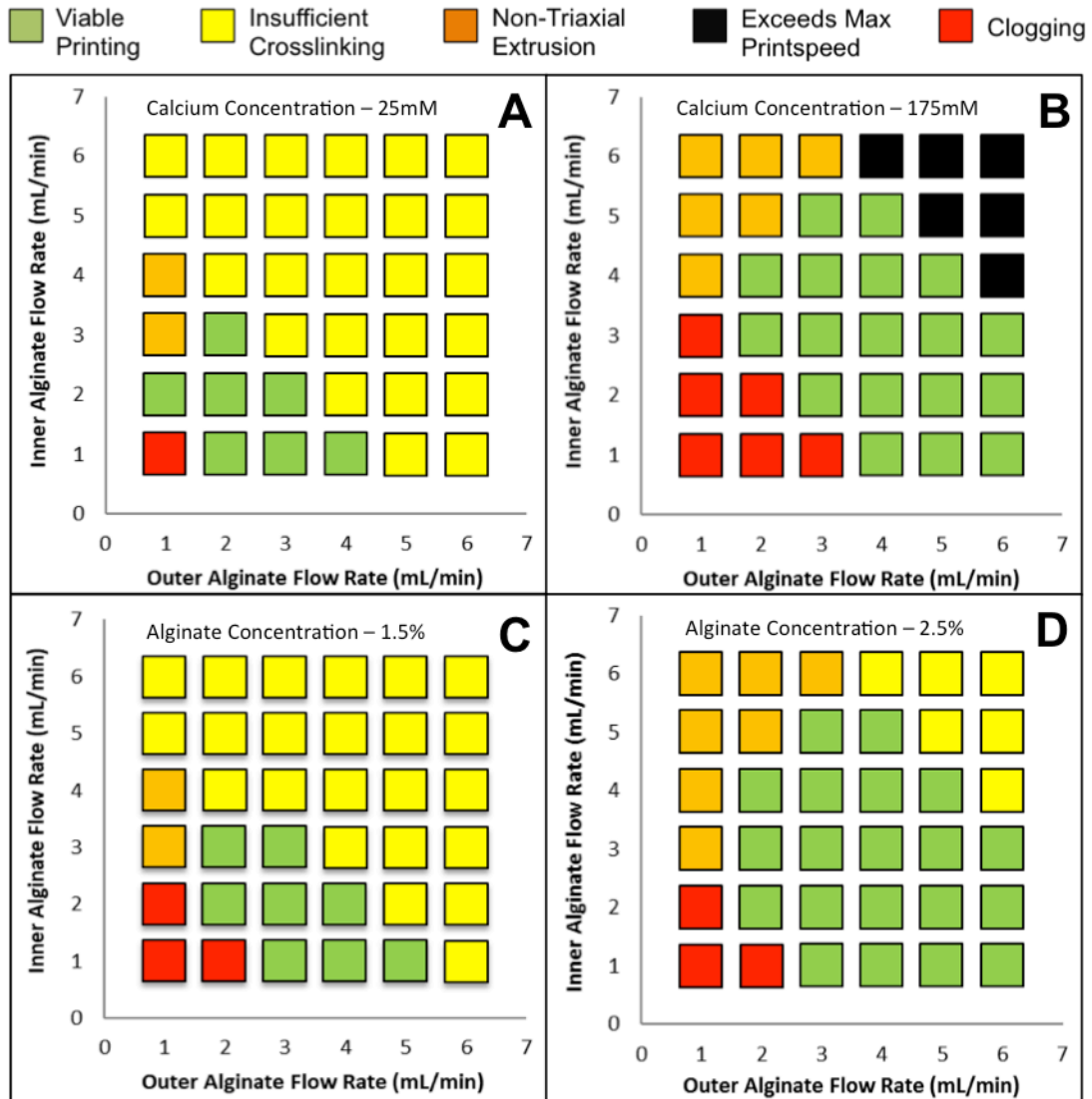


FIG. 3.6: (A-B) Effect of varying calcium concentration on viable printing range, with 2% alginate concentration and calcium flow rates held constant at 3mL/min: (A) – 25mM and B) – 175mM). (C-D) Effect of varying alginate concentration on viable printing range, with 100mM calcium concentration and calcium flow rates are held constant at 3mL/min: (C) – 1.5% and D) – 2.5%).

Next, the concentration of alginate was tested at 1.5% (concentrations lower than this could not be printed) and 2.5% with a constant calcium concentration of 100mM (FIG. 3.6c,d). We found that viable printing increased at higher concentrations and that the region of insufficient crosslinking or “blotting” decreased. This can be explained by examining the occurrence of instability in a viscoelastic flow, and considering the

relationship between viscosity and breakup length. It is well known that the breakup length (the distance from the nozzle exit to the point where the flow is no longer coherent [27]) decreases at lower viscosities [28–30]. Because higher alginate concentrations caused an increase in viscosity, this resulted in a decrease of the aforementioned breakup or “blotting” phenomenon during printing. The extruded flow remained visually stable and the conduit was therefore printed within the viable range with no visual instability observed upon deposition, although the peripheral alginate may not yet have completed gelation.

Lower concentrations of these materials are generally preferred for cellular incorporation in order to maintain isotonic conditions and prevent hydrodynamic damage [31,32]. However, higher concentrations allow improved mechanical strength of the printed structures as well as expansion of the operational range. This increased printing stability using higher material concentrations proved to be particularly useful when printing multi-material structures, and therefore an alginate concentration of 2.5% was used in such cases for increased structural stability. This is discussed in detail in *Section 3.6*.

3.4 Effect of flow rate and print speed on printed channel dimension:

We investigated the effect of flow rate on the size of the hollow channel and concentric gel layers when printing at the corresponding optimal printspeed (FIG. 3.7). Alterations to calcium flow rate caused significant changes to all conduit dimensions (FIG. 3.7a). When calcium flow rate was varied and inner and outer alginate flow was held constant at 2mL/min and 4mL/min respectively, we were able to achieve hollow channel dimensions of $0.69\pm 0.01\text{mm}$ to $1.18\pm 0.04\text{mm}$, inner gel layer dimensions of $1.05\pm 0.02\text{mm}$ to $1.47\pm 0.05\text{mm}$, and outer gel layer dimensions of $1.85\pm 0.06\text{mm}$ to $2.31\pm 0.05\text{mm}$. When the inner alginate flow rate was altered, little effect was seen to the alginate gel layer dimensions (FIG. 3.7b). However, a slight reduction in hollow channel diameter was observed. A similar phenomenon was observed when the outer alginate flow was manipulated (FIG. 3.7c). Outer gel layer dimensions remained relatively constant, while a slight decrease in inner gel layer and hollow channel diameter were found to happen at higher outer alginate flow rates. These findings coincide well with

previous studies done with concentric fluid extrusion [25,33], which describe a simple analytical relationship between the flow rates and the diameter of the hollow channel as shown in the following equation [25]:

$$D = R \left(1 - \left(1 - \frac{2Q_C}{Q_T} \right)^{\frac{1}{2}} \right)^{\frac{1}{2}} \quad (1)$$

where D is the channel diameter, Q_C is the central flow rate, Q_T is the total sum of the flow rates, and R is the radius of the extrusion channel. It was therefore expected that channel dimensions would increase with higher core calcium flow rates, and decrease with higher surrounding sheath flow rates due to the constriction enforced onto the inner flows by an increased outer alginate flow. The theoretical values of channel diameters in our system were calculated based on the above equation and modelled in FIG. 3.7a-c. The experimental results followed the same trends as expected from the calculations. However, the diameters of the printed hollow channels were slightly larger than predicted values. The slight discrepancy in values can be attributed to the fact that the theoretical model was based on fiber extrusion into a solution, while ours were printed on a dry substrate. In our case, the lateral spreading phenomenon that occurs during our printing method may have caused slight flattening of the channel and its dimensions to increase.

With our technique, we were able to fabricate conduits that have a wide range of feasible channel and gel layer dimensions by manipulation of each individual extrusion flow rate. However, it is important to note that even a slight increase to the printspeed above the optimal value can cause significant variation to the printed dimensions due to stretching of the triaxial flow during extrusion. Therefore, we characterized the effect of various printspeeds on hollow channel and concentric gel layer dimensions, as is presented in FIG. 3.7d. As expected, the conduit dimensions decreased with increased printspeeds. This effect was particularly significant on the outer diameter (ranging from 2.04 ± 0.04 mm to 1.68 ± 0.03 mm) because it was the least crosslinked layer, which made it more elastic and flexible to deformation. The advantage of this type of behaviour was that we were able to demonstrate a range of narrower, micro-dimensions that can be achieved by manipulating the printing technique in this way.

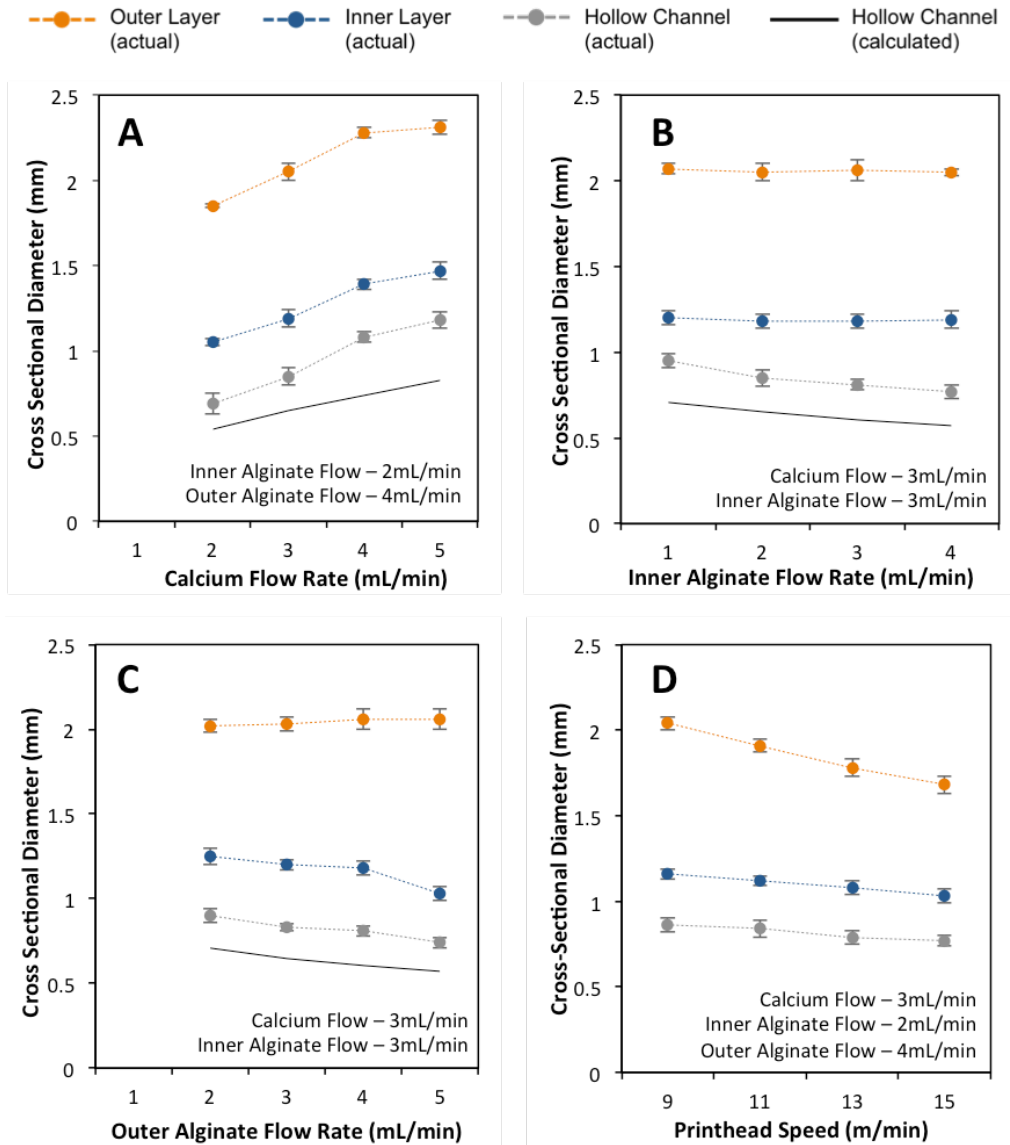


FIG. 3.7: (A-C) Effect of varying flow rates on conduit dimensions. Under each condition, two flow rates are held constant while one is varied. Calcium, inner, and outer alginate flow rates are varied in A), B), and C) respectively. D) Effect of printspeed on conduit dimensions, while flow rates are held constant.

3.5 Multi-cellular printing:

Vascular networks are complex structures that contain multiple cell types, which exist in separate concentric layers. In this section, we demonstrate the ability to seed and print hollow tubes containing concentric layers of two different cell types – specifically RFP transfected HUVECs and GFP transfected 3T3 fibroblasts. HUVECs exist within the inner lumen of a biological blood vessel, whereas fibroblasts are typically found in the

surrounding extracellular matrix [34]. Fibroblasts are often included in endothelial coculture systems due to their production of VEGF and subsequent angiogenic tendencies [35–37]. For this reason, we seeded HUVECs within the inner alginate solution and while 3T3s are encapsulated in the outer alginate solution. Printing was carried out at low flow rates of 2mL/min for all flows in order to conserve the cell-laden materials. The corresponding optimal printspeed (4m/min) was used. Upon printing, a cell-laden hollow gel tube was produced (FIG. 3.8a). Imaging on day 1 revealed clearly distinct layers of each cell type with excellent alignment. FIG. 3.8b shows printing of two parallel cell-laden tubes in close proximity to one another, which resulted in gel fusion and formation of a gel slab integrated with hollow perfusion channels. Merging of outer most alginate layer in this way can be used to form the contiguous bulk of cell-laden ECM of the hydrogel structure while the inner gel layers for the lumen of the perfusion channels, which increases the cellular and material complexity to our construct. Day 1 imaging of the construct's top slice revealed that the concentric architecture was preserved not only in the XY plane (FIG. 3.8a-i, b-i), but in the Z-planes as well (FIG. 3.8a-ii, b-ii). This confirmed that the outer-most layers of fibroblasts encapsulated the inner HUVEC layers, thereby maintaining the structure's hierarchal nature.

In our experiments, we found that printing hollow alginate structures laden with fibroblasts allowed the cells to migrate into the inner lumen of the tubes and line it, thereby forming a tubular monolayer of cells over a period of 21 days (FIG. 3.8c-ii). This phenomenon was unexpected, as fibroblasts cannot successfully adhere to alginate when seeded directly onto the hydrogel surface [38]. However, previous work has shown fibroblasts to be able to grow and proliferate over a period of 25 days when encapsulated within alginate microcapsules [39]. Because fibroblasts are highly motile [40], it can be expected that the cells were able to grow within our alginate structures and then migrate through the gel into the hollow tube. Although the fibroblasts cannot attach to the alginate, they may remain anchored via tight junctions to the cells encapsulated within the gel. The hollow tube guided these motile cells and served as a template to shape them and form a lumen. The HUVECs, however, did not continue to grow over long periods of time (FIG. 3.8c-i). This was expected, as HUVECs are not known to sustain long-term growth when encapsulated in unmodified alginate gels[41].

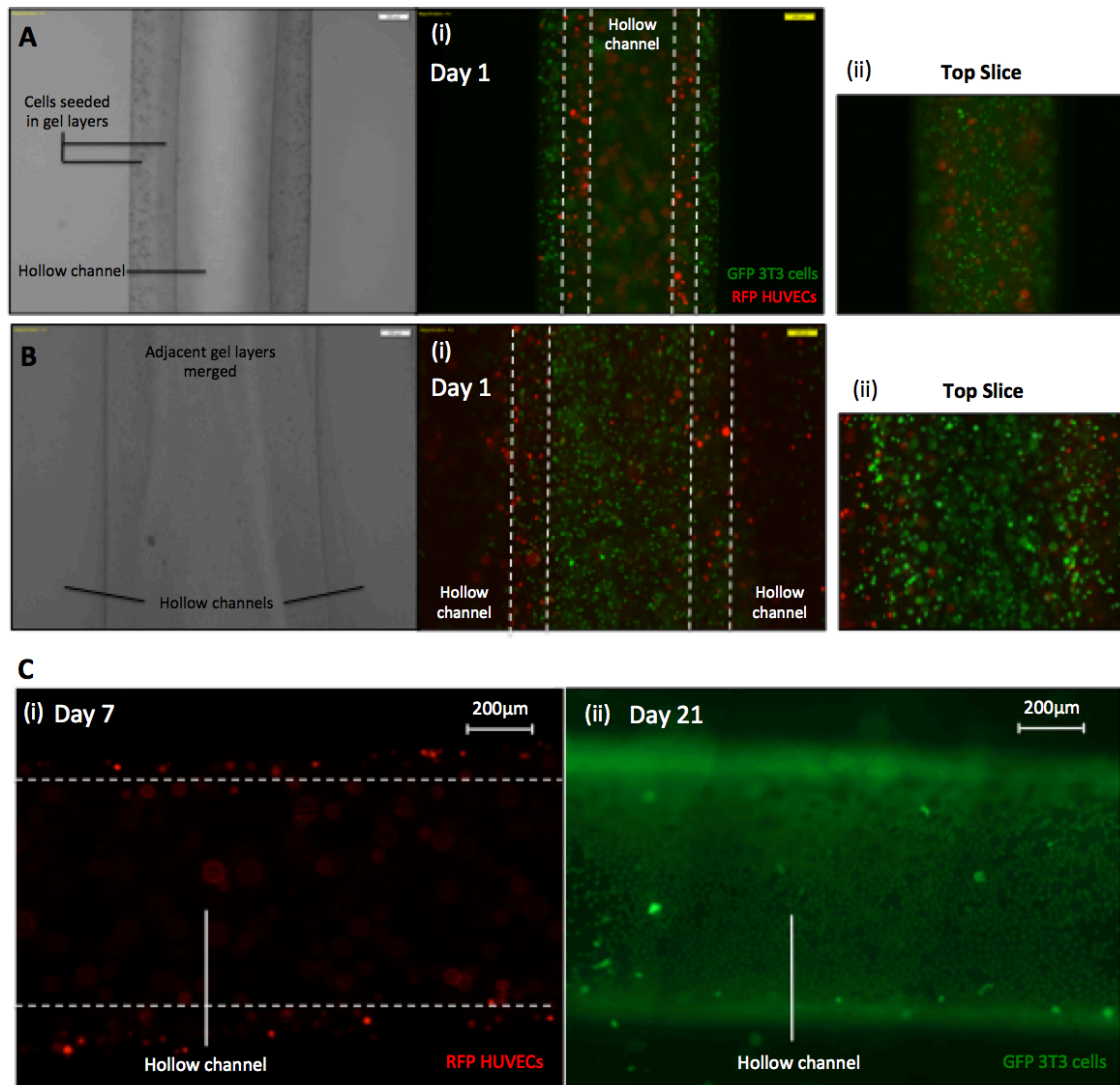


FIG. 3.8: Multi-cellular printing. A) Hollow gel tube is printed with two distinct, hierarchical layers. The inner layer contains HUVECs while the outer layer contains 3T3s, as would normally be found in a typical blood vessel architecture. Structure is imaged on Day 1. B) Merging of two parallel printed tubes results in the formation of cell-laden (HUVECs) conduits embedded in a surrounding bulk ECM that contains secondary cells (3T3s). Structure is imaged on Day 1. Central, cross-sectional slices are seen in (A-i) and (B-i), while the (A-ii) and (B-ii) show top slices of the constructs. These confirm that the hierarchical architecture is maintained in the X, Y, and Z planes. C) HUVECs and 3T3s behave differently when encapsulated in the hollow alginate structures. (C-i) HUVECs do not migrate or line the channel, but rather remain encapsulated in the alginate and quickly decrease in viability. Image is taken on day 7, after which point very few live cells remain. (C-ii) 3T3s migrate into the lumen and form a hollow monolayer of cells that line the inner side of the channel. Image is taken on day 21.

3.6 Multi-material printing:

Fabrication of hollow gel channels composed of more cell-friendly matrices such as collagen or fibrin would aid in the challenge of achieving endothelialisation within the hollow channels. Although alginate is nontoxic and does not activate a chronic immune response in biological tissues, it lacks the necessary ligands required to regulate cellular interactions and promote mammalian cell adhesion [42,43]. Collagen, on the other hand, is the most widely used tissue-derived natural polymer as it is composed of specific amino acid sequences that are recognized by cells. Fibrin is another major component of native ECM and has been found to induce angiogenesis, thereby playing an important role in natural wound healing [44,45]. These materials are well known to promote cell-adhesion and have been shown to be ideal for vascularization techniques [3,19,46,47]. Incorporating collagen and fibrin into our scaffolding structures will allow the cells to proliferate and achieve the morphology necessary for creating a true lumen. However, both these materials have low mechanical stiffness (0.18-0.25kPa and 0.12-0.14kPa for 3mg/mL collagen and 6mg/mL fibrin respectively) in comparison to alginate, which is well known for its structural integrity (3kPa at 3% w/v) [13].

For these reasons, we incorporated a combination of hydrogel materials (specifically alginate with collagen or fibrin) in order to create constructs that were both structurally stable and exhibited superior cell adhesion. To accomplish this, we continued to use a central core flow of calcium chloride and an inner flow of alginate, while substituting the outer flow for a hybrid hydrogel mix that consisted of either HUVEC-laden alginate-collagen (FIG. 3.9a) or alginate-fibrinogen (FIG. 3.9b). We found that printing multi-material structures with an inner alginate layer concentration of 2.5% w/v was necessary in order to achieve successful extrusion. As previously discussed in *Section 3.3*, higher concentrations of alginate were found to increase stability of the extruded jet. This inner jet stabilization provided the necessary support required by the surrounding lower viscosity materials during extrusion. Use of alginate concentrations lower than 2.5% were found to be unsuccessful in printing of viable conduits due to excessive pooling of materials. Attempts were also made to use higher concentrations of calcium chloride in order to decrease gelation time prior to extrusion. However, because

low inner and outer flow rates were used (2mL/min) in order to conserve materials, the high calcium concentrations caused immediate clogging of the nozzle (refer *Section 3.3*).

After printing, sodium citrate was used to dissolve the alginate in alginate-fibrin samples in order to create constructs that were composed solely of fibrin, thereby providing an ideal scaffold for endothelial cell adhesion. With this method, it was found that the endothelial cells seeded in the fibrin layer were able to regain their morphology and successfully attach to the lumen of the matrix, thereby resembling the endothelial wall of a blood vessel (FIG. 3.9c). This citrate mechanism was not used with alginate-collagen samples, as they were found to disintegrate and lose their structure if the alginate was removed. This is because collagen has a significantly lower mechanical stiffness at this working concentration (0.18-0.25kPa at 3mg/mL) in comparison to fibrin (1-2.5kPa at 25mg/mL) [48]. The higher strength allowed the fibrin to maintain its structural composition in the absence of alginate, which confirmed that high hydrogel concentration is necessary for successful printing. Printing with higher collagen concentrations was not possible and caused consistent clogging (as is explained in *Section 2.4*). However, it was found that the use of a composite hydrogel mixture containing collagen still showed higher cell viability over a 5-day period in comparison to constructs composed solely of alginate (FIG. 3.9d). Hybrid samples containing both fibrin and alginate also showed superior live cell counts (482±43 cells and 556±25 cells for alginate-collagen and alginate-fibrin in comparison to 233±22 cells in alginate) (FIG. 3.9d), confirming that our strategy for fabricating multi-material structures is advantageous in increasing the biocompatibility of our constructs without compromising the structural integrity.

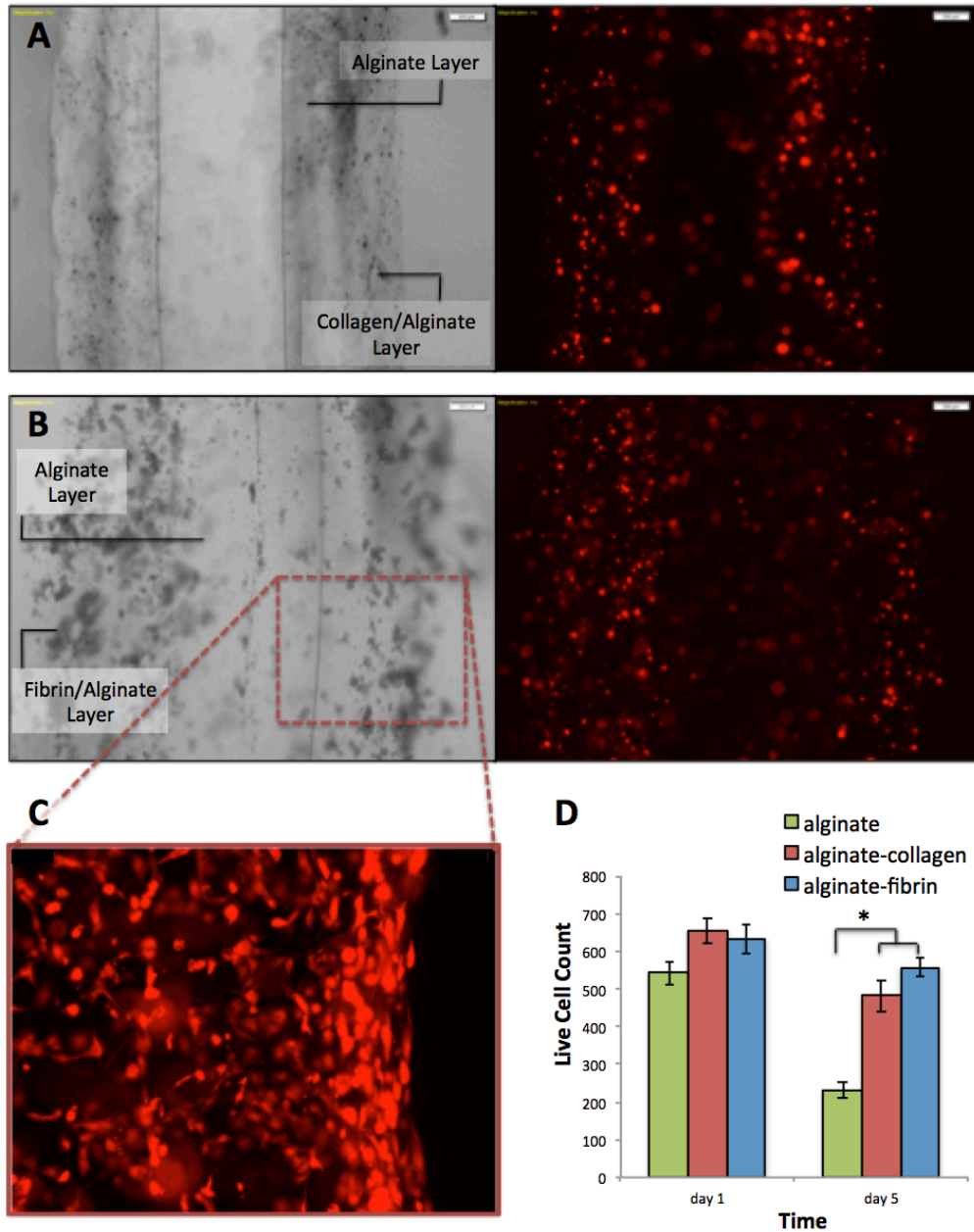


FIG. 3.9: Multi-material printing is feasible using triaxial extrusion, which allows weaker matrices that are more cell-friendly to be printed with the support of stronger, structurally sound materials. Hollow gel structures printed using an inner supporting layer of alginate and an outer HUVEC-laden layer of A) alginate-collagen or B) alginate fibrin. Images show that cells are encapsulated within the outer-most layer. C) Dissolving the alginate using citrate allows the cells to adhere to the fibrin layer, showing good morphology, and form an endothelial wall. D) Printing of these cell-laden hybrid materials results in increased live cell counts over a 5-day period in comparison to structures printed using only alginate. Single asterisk (*) represents p -level <0.01 .

References

- [1] J. S. Miller *et al.*, “Rapid casting of patterned vascular networks for perfusable engineered three-dimensional tissues,” *Nat. Mater.*, vol. 11, no. 9, pp. 768–774, 2012.
- [2] A. P. Golden and J. Tien, “Fabrication of microfluidic hydrogels using molded gelatin as a sacrificial element,” *Lab Chip*, vol. 7, no. 6, pp. 720–725, 2007.
- [3] V. K. Lee, A. M. Lanzi, H. Ngo, S. S. Yoo, P. A. Vincent, and G. Dai, “Generation of multi-scale vascular network system within 3D hydrogel using 3D bio-printing technology,” *Cell. Mol. Bioeng.*, vol. 7, no. 3, pp. 460–472, 2014.
- [4] V. K. Lee *et al.*, “Creating perfused functional vascular channels using 3D bio-printing technology,” *Biomaterials*, vol. 35, no. 28, pp. 8092–8102, 2014.
- [5] L. E. Bertassoni *et al.*, “Hydrogel bioprinted microchannel networks for vascularization of tissue engineering constructs,” *Lab Chip*, vol. 14, no. 13, pp. 2202–11, 2014.
- [6] R. Attalla, C. Ling, and P. Selvaganapathy, “Fabrication and characterization of gels with integrated channels using 3D printing with microfluidic nozzle for tissue engineering applications,” *Biomed. Microdevices*, vol. 18, no. 17, 2016.
- [7] V. Mironov, R. P. Visconti, V. Kasyanov, G. Forgacs, C. J. Drake, and R. R. Markwald, “Organ printing: Tissue spheroids as building blocks,” *Biomaterials*, vol. 30, no. 12, pp. 2164–2174, 2009.
- [8] Y. Zhang, Y. Yu, H. Chen, and I. T. Ozbolat, “Characterization of printable cellular micro-fluidic channels for tissue engineering,” *Biofabrication*, vol. 5, no. 2, p. 25004, 2013.
- [9] Q. Gao, Y. He, J. Fu, A. Liu, and L. Ma, “Coaxial nozzle-assisted 3D bioprinting with built-in microchannels for nutrients delivery,” *Biomaterials*, vol. 61, pp. 203–215, 2015.
- [10] Y. Ling *et al.*, “A cell-laden microfluidic hydrogel,” *Lab Chip*, vol. 7, no. 6, pp. 756–762, 2007.
- [11] J. P. Gleghorn, C. S. D. Lee, M. Cabodi, A. D. Stroock, and L. J. Bonassar, “Adhesive properties of laminated alginate gels for tissue engineering of layered structures,” *J. Biomed. Mater. Res. - Part A*, vol. 85, no. 3, pp. 611–618, 2008.
- [12] M. Cabodi, N. W. Choi, J. P. Gleghorn, C. S. D. Lee, L. J. Bonassar, and A. D. Stroock, “A microfluidic biomaterial,” *J. Am. Chem. Soc.*, vol. 127, no. 40, pp. 13788–13789, 2005.
- [13] S. Muehleder, A. Ovsianikov, J. Zipperle, H. Redl, and W. Holnthoner, “Connections Matter: Channeled Hydrogels to Improve Vascularization,” *Front. Bioeng. Biotechnol.*, vol. 2, no. November, pp. 1–7, 2014.
- [14] Y. Gao, “Architecture of the Blood Vessels,” in *Biology of Vascular Smooth Muscle: Vasoconstriction and Dilatation*, Singapore: Springer, 2017, pp. 3–12.
- [15] Y. Liu, J. Lu, H. Li, J. Wei, and X. Li, “Engineering blood vessels through micropatterned co-culture of vascular endothelial and smooth muscle cells on bilayered electrospun fibrous mats with pDNA inoculation,” *Acta Biomater.*, vol. 11, no. 1, pp. 114–125, 2015.
- [16] S. Liu *et al.*, “Bilayered vascular grafts based on silk proteins,” *Acta Biomater.*, vol. 9, no. 11, pp. 8991–9003, 2013.

- [17] A. Hasan, A. Paul, A. Memic, and A. Khademhosseini, “A multilayered microfluidic blood vessel-like structure.,” *Biomed. Microdevices*, vol. 17, no. 5, p. 88, 2015.
- [18] C. Norotte, F. S. Marga, L. E. Niklason, and G. Forgacs, “Scaffold-free vascular tissue engineering using bioprinting,” *Biomaterials*, vol. 30, no. 30, pp. 5910–5917, 2009.
- [19] S. Sakai, S. Yamaguchi, T. Takei, and K. Kawakami, “Oxidized alginate-cross-linked alginate/gelatin hydrogel fibers for fabricating tubular constructs with layered smooth muscle cells and endothelial cells in collagen gels,” *Biomacromolecules*, vol. 9, no. 7, pp. 2036–2041, 2008.
- [20] T. Boland, T. Xu, B. Damon, and X. Cui, “Application of inkjet printing to tissue engineering,” *Biotechnol. J.*, vol. 1, no. 9, pp. 910–917, 2006.
- [21] K. Pataky, T. Braschler, A. Negro, P. Renaud, M. P. Lutolf, and J. Brugger, “Microdrop Printing of Hydrogel Bioinks into 3D Tissue-Like Geometries,” *Adv. Mater.*, vol. 24, no. 3, pp. 391–396, 2012.
- [22] D. D. Joseph, K. Nguyen, and J. E. Matta, “Jets into liquid under gravity,” *J. Fluid Mech.*, vol. 128, pp. 443–468, 1983.
- [23] T. Majmudar, M. Varagnat, W. Hartt, and G. McKinley, “Nonlinear Dynamics of Coiling in Viscoelastic Jets,” 2010.
- [24] J. O. Cruickshank and B. R. Munson, “Viscous fluid buckling of plane and axisymmetric jets,” *J. Fluid Mech.*, vol. 113, no. 1, p. 221, 1981.
- [25] K. H. Lee, S. J. Shin, Y. Park, and S. Lee, “Synthesis of Cell-Laden Alginate Hollow Fibers Using Microfluidic Chips and Microvascularized Tissue-Engineering Applications **,” *Small*, vol. 5, no. 11, pp. 1264–1268, 2009.
- [26] C. K. Kuo and P. X. Ma, “Ionically crosslinked alginate hydrogels as scaffolds for tissue engineering: Part 1. Structure, gelation rate and mechanical properties,” *Biomaterials*, vol. 22, no. 6, pp. 511–521, 2001.
- [27] F. W. Kroesser and S. Middleman, “Viscoelastic jet stability,” *AIChE J.*, vol. 15, no. 3, pp. 383–386, 1969.
- [28] M. Goldin, R. Pfeffer, and R. Shinnar, “Break-up of a capillary jet of a non-Newtonian fluid having a yield stress,” *Chem. Eng. J.*, vol. 4, no. 1, pp. 8–20, 1972.
- [29] Y. Kitamura and T. Takahashi, “Breakup of jets in power law non-newtonian – newtonian liquid systems,” *Can. J. Chem. Eng.*, vol. 60, no. 6, pp. 732–737, 1982.
- [30] R. P. Mun, J. A. Byars, and D. V. Boger, “The effects of polymer concentration and molecular weight on the breakup of laminar capillary jets,” *J. Nonnewton. Fluid Mech.*, vol. 74, no. 1, pp. 285–297, 1998.
- [31] Y. Chisti, “Hydrodynamic damage to animal cells.,” *Crit. Rev. Biotechnol.*, vol. 21, no. 2, pp. 67–110, 2001.
- [32] P. Cheetham, K. Blunt, and C. Bucke, “Physical studies on cell immobilization using calcium alginate gels,” *Biotechnol. Bioeng.*, vol. XXI, no. 1979, pp. 2155–2168, 1979.
- [33] T. Takei, N. Kishihara, S. Sakai, and K. Kawakami, “Novel technique to control inner and outer diameter of calcium-alginate hydrogel hollow microfibers, and immobilization of mammalian cells,” *Biochem. Eng. J.*, vol. 49, no. 1, pp. 143–147, 2010.

- [34] S. Baiguera and D. Ribatti, “Endothelialization approaches for viable engineered tissues,” *Angiogenesis*, vol. 16, no. 1, pp. 1–14, 2013.
- [35] S. Fuchs, E. Dohle, M. Kolbe, and C. J. Kirkpatrick, “Outgrowth endothelial cells: sources, characteristics and potential applications in tissue engineering and regenerative medicine,” *Bioreact. Syst. Tissue Eng. II*, pp. 201–217, 2010.
- [36] A. Reinisch *et al.*, “Humanized large-scale expanded endothelial colony-forming cells function in vitro and in vivo,” *Blood*, vol. 113, no. 26, pp. 6716–6725, 2009.
- [37] M. Poh *et al.*, “Blood vessels engineered from human cells,” *Lancet*, vol. 365, no. 9477, pp. 2122–2124, 2005.
- [38] B. Sarker *et al.*, “Evaluation of fibroblasts adhesion and proliferation on alginate-gelatin crosslinked hydrogel,” *PLoS One*, vol. 9, no. 9, 2014.
- [39] P. L. Chang, G. Hortelano, D. E. Awrey, and M. Tse, “Growth of recombinant fibroblasts in alginate microcapsules,” *Biotechnol. Bioeng.*, vol. 43, no. 10, pp. 925–933, 1994.
- [40] K. C. Olbrich, T. T. Andersen, F. A. Blumenstock, and R. Bizios, “Surfaces modified with covalently-immobilized adhesive peptides affect fibroblast population motility,” *Biomaterials*, vol. 17, no. 8, pp. 759–764, 1996.
- [41] S. J. Bidarra, C. C. Barrias, K. B. Fonseca, M. A. Barbosa, R. A. Soares, and P. L. Granja, “Injectable in situ crosslinkable RGD-modified alginate matrix for endothelial cells delivery,” *Biomaterials*, vol. 32, no. 31, pp. 7897–7904, 2011.
- [42] B. Alberts, *Molecular Biology of the Cell*, 3rd ed. Garland Science, 2017.
- [43] S. Beyer, T. Mohamed, and K. Walus, “A Microfluidics Based 3D Bioprinter with On-The-Fly Multimaterial Switching capability,” in *17th International Conference on Miniaturized Systems for Chemistry and Life Sciences*, 2013.
- [44] C. Perka, U. Arnold, R.-S. Spitzer, and K. Lindenhayn, “The use of fibrin beads for tissue engineering and subsequential transplantation,” *Tissue Eng.*, vol. 7, no. 3, pp. 359–361, 2001.
- [45] X. Chen *et al.*, “Prevascularization of a fibrin-based tissue construct accelerates the formation of functional anastomosis with host vasculature,” *Tissue Eng. Part A*, vol. 15, no. 6, pp. 1363–1371, 2008.
- [46] C. J. Hansen *et al.*, “High-throughput printing via microvascular multinozzle arrays,” *Adv. Mater.*, vol. 25, no. 1, pp. 96–102, 2013.
- [47] R. F. Nicosia and A. Ottinetti, “Modulation of microvascular growth and morphogenesis by reconstituted basement membrane gel in three-dimensional cultures of rat aorta: a comparative study of angiogenesis in matrigel, collagen, fibrin, and plasma clot,” *Vitr. Cell. Dev. Biol.*, vol. 26, no. 2, pp. 119–128, 1990.
- [48] H. Duong, B. Wu, and B. Tawil, “Modulation of 3D fibrin matrix stiffness by intrinsic fibrinogen–thrombin compositions and by extrinsic cellular activity,” *Tissue Eng. Part A*, vol. 15, no. 7, pp. 1865–1876, 2009.

Chapter 4

SILICON CARBIDE NANOPARTICLES AS AN EFFECTIVE BIOADHESIVE TO BOND COLLAGEN CONTAINING COMPOSITE GEL LAYERS FOR TISSUE ENGINEERING APPLICATIONS

Complete citation:

Rana Attalla, Celine Ling and Ponnambalam R Selvaganapathy. “*Silicon carbide nanoparticles as an effective bioadhesive to bond collagen containing composite gel layers for tissue engineering applications.*” *Advanced Healthcare Materials* 7.5 (2018)

Relative Contributions:

Attalla, R: Designed and performed all characterization experiments including sample synthesis, testing, and imaging. Interpreted and analyzed the resulting data, and wrote the manuscript.

Ling, C: Assisted with sample fabrication and mechanical testing, as well as biological cell culture and maintenance.

Note to the Reader:

A supplementary section is included at the end of the chapter containing additional figures and information that are referred to throughout the body of the chapter.

1. Introduction

The creation of functional artificial organs requires the ability to perfuse 3D tissue constructs with essential nutrients and remove metabolic waste. Current AM techniques that have been used to create perfusion networks such as 3D printing with or without the use of sacrificial spacers [1-4] can have many disadvantages including material waste, cost, or time-consuming and tedious processing [5-7]. The removal process of sacrificial spacers can often compromise the structural integrity of the fabricated constructs [8]. There are also limitations with respect to achievable feature resolution when printing gel-like materials due to spreading of the material during deposition. Some of these materials can only be printed by means of UV light exposure and the use of a photoinitiator, which can be highly toxic to exposed cells [9]. Biofabrication via planar processing, on the other hand, employs mold casting to replicate microchannel features and conserves valuable bioinks [10,11]. Due to its simple and adaptable nature, it has significant potential in the creation of heterogeneous-layered constructs that are incorporated with high-definition features, while using small amounts of valuable material [12].

Current planar processing techniques have utilized a variety of bonding methods to fuse multiple layers together to form tissue constructs with integrated microfluidic networks. For instance, thermal bonding has been used to integrate multiple layers of agarose gels embedded with microfluidic channels [13]. Heating the agarose gel layers to 65°C for few seconds leads to melting of the gel at the interface, which fuses when the temperature is lowered. Although moderate short-term cell viability was demonstrated, this method is suitable only for gels that melt and exposure to high temperatures may not be suitable for many other types of cells. Alternatively, chemical methods to bond gel layers have also been used in particular with alginate, that gels through ionic crosslinking [14]. In this method, citrate (a calcium chelator) is sprayed on the gel surface to uncrosslink the surface. Subsequent contact with another alginate layer, similarly processed, leads to crosslinks between the two layers as calcium from the bulk diffuses to the interface [14,15]. Strong bond strength was achieved; however this method is strictly limited to alginate and would not be suitable for alternative hydrogels such as collagen, which are biologically more relevant. Exposure to high concentrations of citrate may also have adverse effects on cell viability over the longer time frame. Finally, “liquid glue”

containing precursors that form the gel layers to be bonded has also been used to adhere multiple alginate/collagen composite layers. In this method, temperature controlled fibrillogenesis was used to assemble cross linked collagen fibrils that connect the collagen in the gel layer with those in the glue, forming a bond[16]. Although this method avoids adverse conditions, such as high temperatures and use of chaotropic agents, it is arduous to assemble more than a few layers and the use of liquid glue restricts it to integration of large channels only.

Therefore, a simple, versatile and scalable method to adhere layers of biologically important extracellular matrices such as collagen while still preserving the microstructural features, such as microchannel embedded in it, does not exist. Although collagen is the most commonly used tissue-derived natural ECM [17], it has not been extensively used in layer-by-layer processes due to a number of reasons such as its weak mechanical properties, that make it difficult to handle, as well as lack of an effective adhesive to form strong bond between its layers. Alginate, on the other hand, forms structurally sound gels, but may not be an effective ECM for many types of cells [18, 19]. Therefore, creating hybrid gel films composed of both of these materials allowed adequate mechanical properties to be achieved, as well as maintain favorable properties for cell growth. However, this composite material still needs effective adhesive materials to form multilayer composites. In this paper, we demonstrate the first use of silicon carbide nanoparticles (SiC) as adhesives to adhere composite hydrogel layers to integrate perfusion channels in their bulk. SiC has previously been used in a number of biological applications such as DNA transformation, RNA purification, cell imaging, and in dental implants [20-24]. Yet, there has been no reported use as a hydrogel adhesive until now.

2. Methods and Materials

2.1 Preparation of gel solutions:

Gel solutions were prepared using solely sodium alginate (Alg) (2% w/w, Sigma Aldrich) or a combination of both sodium alginate and collagen (3mg/mL, Santa Cruz Biotechnology) mixed together into a 50:50 composite (Alg-Col). In order to prepare the

hybrid gels consisting of both alginate and collagen, the acidic collagen solution was first neutralized with 20 μ L/mL of sodium hydroxide (1N, Fisher Scientific), which facilitates slow gelation (typically 30min or more). After neutralization, the alginate solution was quickly mixed with collagen at a 1:1 ratio. Subsequently, CaCl₂ solution (100mM, Fisher Scientific) was used as a crosslinking agent in order to solidify the gel films. This was done by applying a calcium soaked filter paper to the surface in order to achieve a flat film, and then the mold was submerged into a calcium bath in order to complete gelation. Hydrogels were created using both Milli-Q water-based (Alg, Alg-Col) and cell media-based solutions (Alg-EBM, Alg-Col-EBM) for testing as it is likely that in practical applications the hydrogels will be loaded with cell media to promote growth and tissue formation after fabrication.

2.2 Fabrication of microchannel structures:

Several patterned molds (*FIG. S4.2*) were fabricated using high definition 3D printing of UV-curable acrylic plastic (VisiJet EX200) in order to create particular network designs with varying channel dimensions (150 μ m – 1mm) and high-resolution spacing (500-600 μ m) between specific features. The uncrosslinked hydrogel solutions composed of Alg-Col-EBM were cast onto these molds, followed by immediate gelation via crosslinking using calcium chloride solution. The films were given sufficient time to solidify (~1hr) and were easily peeled from the mold. These patterned films were then adhered to a flat gel piece thereby creating enclosed microchannel structures. This method was extended to include multiple layers within a single scaffold structure in order to create thicker tissue constructs. Adhesive was also used to create interconnects by means of adhering tubing to the fabricated hollow gel channel, thereby forming inlet and outlet junctions to be used for perfusion.

2.3 Mechanical testing:

Mechanical testing was used to determine the effectiveness of each adhesive with various hydrogel materials. Samples for tensile testing were cast at a thickness of 500 μ m and cut (with the aid of a premarked template) into rectangular sections measuring 1cm in width and 2.5cm in length. Silicon carbide (SiC) nanoparticles and silica nanoparticles

were used as adhesives to bond two hydrogel pieces at a concentration of 0.01wt% and 50wt% respectively (*Section S1*). The silicon carbide (SiC) nanoparticles (Sigma Aldrich) were diluted in deionized (DI) water. The silica nanoparticles was obtained as a suspension from Sigma Aldrich (TM-50 Ludox nanosilica solution) and used as is. Two pieces were bonded together using 250 μ L of the various adhesive solutions and pressing them together with a light force in order to create a test sample with an overlapping 1cm by 1cm joint area. Care was taken to ensure that the hydrogels and the interface were completely wet during the entire duration of testing.

Mechanical and lap shear testing of the adhered hydrogel samples was performed using an Instron SFL machine (Instron, Norwood) (*FIG. S4.3a*). A 50N load cell was used and the elongation rate was set to 5mm/min. The data acquisition and processing were performed using Merlin software. The maximum load force, determined by the peak of the produced load/extension curve, was normalized with respect to lap junction area in order to calculate the maximum tensile stress. Custom-made grippers (*FIG. S4.3b*) that are more suitable for handling of delicate hydrogels were used to stabilize the soft test specimens. Bond strength was assessed using varying concentrations of each adhesive as well as altering the duration of time between adhesive administration and mechanical testing.

2.4 Cell Culture and preparation:

Mouse 3T3 fibroblasts (ATCC) were cultured according to standard protocols. Dulbecco's Modified Eagle Medium (DMEM) (Sigma) completed with 10% fetal bovine serum (FBS) (Thermofisher) and 1% penicillin streptomycin (Thermofisher) was used to make media changes to cell culture until 100% confluency was achieved. Sodium alginate powder and calcium chloride were sterilized with UV light. Alginate-DMEM and calcium-DMEM based solutions were made at 2%w/v and 0.1M respectively. The 3T3s were harvested using 0.25% Trypsin-EDTA and the cell suspension was diluted accordingly to create the required cell concentrations. Experiments were done using cell concentrations of 2.5×10^6 cells/mL. The cell suspension was mixed in with a 1:1 collagen and alginate-DMEM solution prior to casting. Live and dead stain images of cell-laden samples were taken using confocal microscopy (LSM510, Zeiss). Samples were stained

using calcein acetoxymethyl ester (calcein AM) and ethidium homodimer-2 (Life Technologies) at a concentration of 0.5% v/v. Z-stack sample projections were formed using image slices taken along the Z-axis from the bottom of the sample to the surface at intervals of 10 μ m or 20 μ m.

3. Results and Discussion

3.1 Hollow channel network fabrication and perfusion:

Our design principle is simple: composite gel layers made of alginate and collagen, embedded with microscale features, are fabricated using mold casting. These layers are peeled off from the mold and adhered to one another in order to form thick, 3D structures with embedded microfeatures such as hollow microchannels in the bulk (FIG. 4.1). With an appropriate bonding method, this layer by layer approach is suitable for fabricating large, multilayered scaffolding structures that may be composed of various materials for tissue engineering purposes. A suitably designed microchannel network in these layer can perfuse the entire bulk and maintain the viability of cells seeded in it. Here, we demonstrate the ability to successfully create multilayered hydrogel structures with embedded hollow channel networks of varying dimensions that are easily perfusable, using SiC as an appropriate biocompatible adhesive.

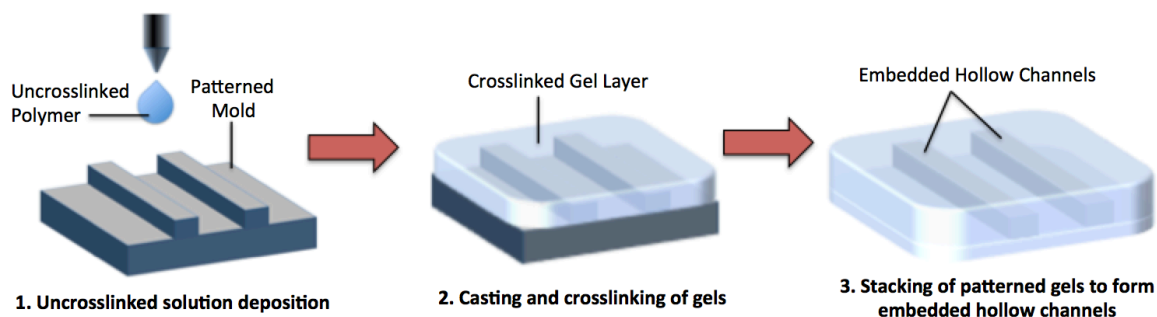


FIG. 4.1: Schematic of the Casting, Peeling, Stacking (CPS) strategy used for fabrication of 3D structures with embedded hollow channels. 1. Uncrosslinked liquid polymer is deposited onto the 3D printed patterned molds. The solution spreads evenly 2. Upon gelation, a solid layer is formed and the firm gels are easily peeled and removed from the molds. 3. Adhesive is deposited in between patterned gel layers, and films are stacked upon one another thereby creating embedded hollow features within the bulk of the construct.

Hydrogel gel solutions composed of 1% w/w alginate and 1.5mg/mL collagen in cell media was cast as thin layers on 3D printed molds that had microchannel features (FIG. S4.2). The layers were peeled off and then adhered to another layer of thin and flat hydrogel (FIG. 2a-i), thereby creating enclosed hollow channel network or patterns (FIG. 2a-ii). We used SiC and nanosilica solution (which has been previously reported to adhere gelatin^[12]) to bond the layers together. The concentrations used for both these materials were the lowest that produced successful bonding (0.01% and 30% w/w in water for SiC and nanosilica respectively). When used to create large channels (width $\geq 2\text{mm}$), both SiC and nanosilica were successful in bonding and the channels were easily perfused. (FIG. 2a-iii). However, when bonding gel layers with small channels (width $< 2\text{mm}$), the concentrated nanosilica solution produced good bonding but also caused complete blockage of the channels thereby impeding our ability to perfuse the channels. On the other hand, low concentration SiC solution allowed us not only to successfully bond but also did not block the channels. We were able to perfuse hollow channels with widths as small as $200\mu\text{m}$ (FIG. 4.2b-i). It should be noted that without the use of SiC as an adhesive, injected media would leak outside the hollow channels upon perfusion (FIG. 4.2b-ii), while bonding with SiC allowed leak-proof perfusion of the construct (FIG. 4.2b-iii). Furthermore, SiC was also successful in bonding microchannels ($150\mu\text{m}$) that were closely spaced ($500\text{-}600\mu\text{m}$) and did not cause any channel blockage (FIG. 4.2c-i). Such resolution and spacing of channels allowed us to perfuse them, enabling nutrient and oxygen transport, which maintained the viability of the cells (FIG. 4.2c-ii,iii). Such perfusion channels are critical when constructing bulk gels constructs with large thickness in which case the cells in the bulk quickly become deficient in nutrients^[1a,c]. We determined that hollow channels fabricated using silicon carbide as an adhesive can withstand high pressures during perfusion – upwards of 300mmHg (FIG. S4.4). This is significantly higher than normal blood pressures found in biological vascular networks.

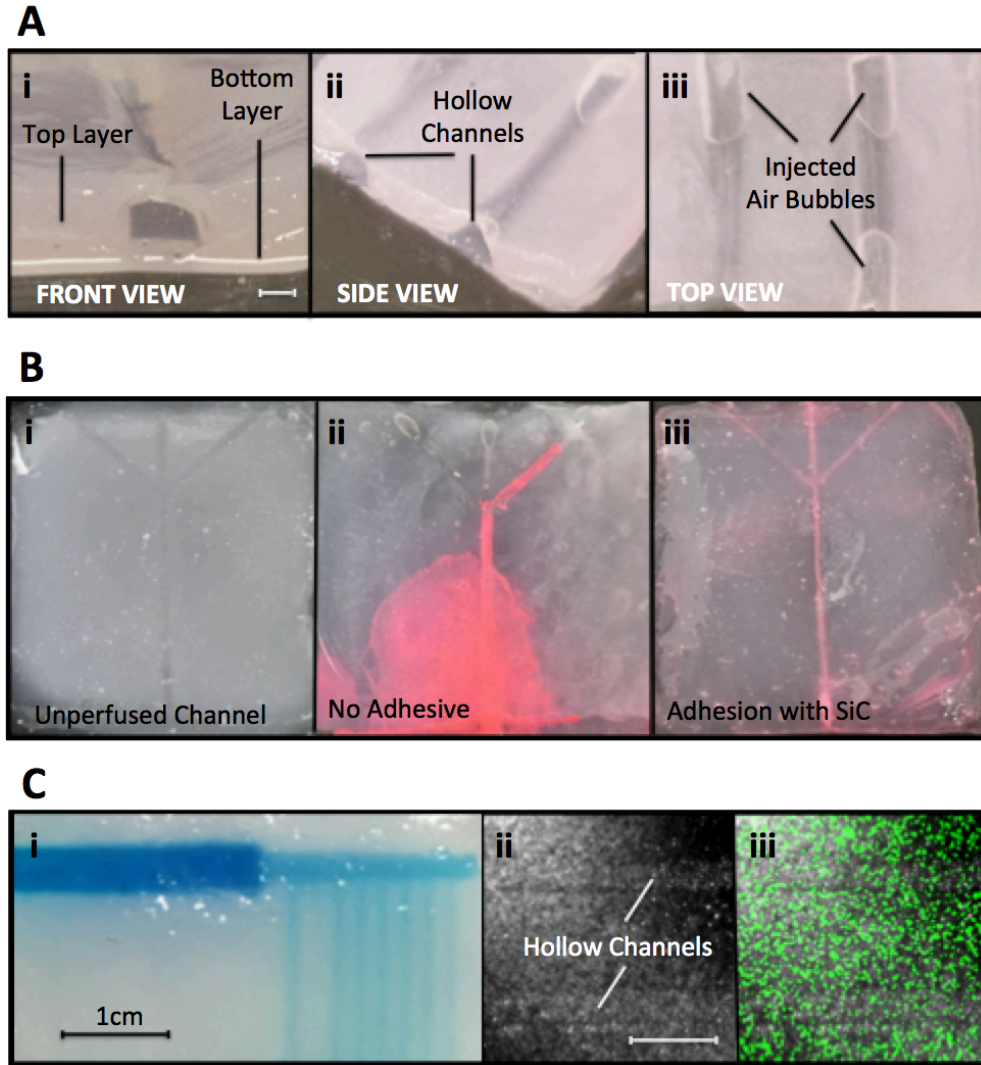


FIG. 4.2: A) i) Large hollow channel fabrication by adhesion of molded Alg-Col-EBM hydrogel onto flat film. Scale bar, 1mm. ii)Hollow channels maintain their structural integrity (iii) These channels are easily perfusable as seen by the injected air bubbles. B) i)Branched hollow channel network embedded in media-based hybrid gel via planar processing. Channel dimensions are $200\mu\text{m}$ width by $400\mu\text{m}$ height. ii)When the branched network is perfused without any adhesive used to bind the layers, injected media leaks out of the channel and in between the two layers. iii)When the branched network is perfused post adhesion using 0.01% SiC, media flows easily from one end of the construct to the other. There is no observed flow obstructions or leakages. C) i)Perfusion of high-resolution channel network patterns adhered with SiC. Channel cross-sections are $150\times 200\mu\text{m}$ and are spaced $500\mu\text{m}$ apart. Scale bar, 1cm. ii)Confocal microscopy used to image microchannels in (i). iii)Z-stack projection showing live stain of cells seeded in the hydrogel matrix surrounding the patterned microchannels seen in ii), thereby demonstrating maintenance of cell viability in bulk regions.

With our layer-by-layer technique, we have demonstrated that single gel layers containing microchannels with complex patterns and a wide range of widths (250 μm – 1mm) can be fabricated (FIG. 4.3a,b). In addition, we can also stack these single gel layers and bond them using the adhesives to form thick gels (8mm) with embedded hollow channels (FIG. 4.3c) that can be perfused. These experiments demonstrate that SiC at very low concentration is an effective adhesive and can create thick multilayer gel structures with leak-proof integrated channels that can be used for perfusion.

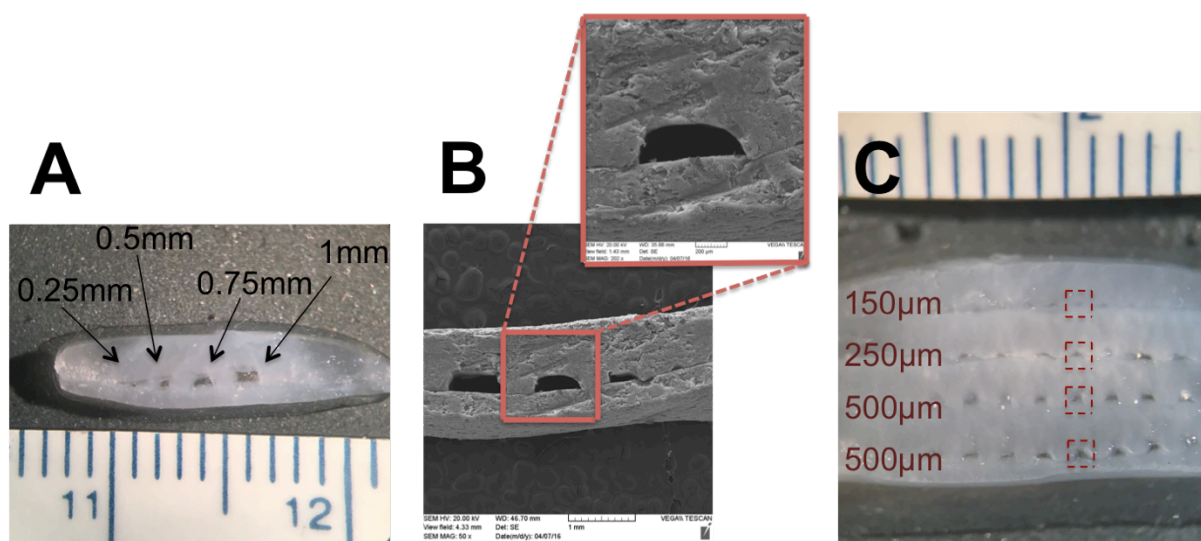


FIG. 4.3: A) Cross-section of embedded hollow microchannels following SiC adhesion of two hydrogel layers. Fabricated hollow channel dimensions varied over a wide range (250 μm -1mm). B) SEM image of cross-section seen in (A). C) Cross-sectional image thick, multilayered hydrogel (8mm) containing embedded channels of varying sizes. This demonstrates the ability to perfuse large, thick constructs such that nutrients can be transported to bulk regions of the construct that are otherwise unreachable.

3.2 Adhesion strength of various composite hydrogels:

We performed mechanical testing to compare the effect of the nanoparticle adhesives on different hydrogel materials that would be used in tissue engineering applications. We performed lap-shear adhesion tests (n=5) on hydrogels composed of alginate (Alg) and collagen (Col) prepared using Milli-Q water and cell media (Endothelial Basal Media – EBM). The results shown in FIG. 4.4 indicate that both the

adhesives significantly improve the bond strength in gels containing collagen and/or prepared using cell media. First, blocks of alginate gels prepared in DI water was tested. They were bonded with each other using procedures described in the methods section. Neither SiC nor nanosilica showed any improvement in bond strength over the simple pressing of the two gels together (control). Alginate inherently is adhesive due to exchange of ionic crosslinks when two gel layers are brought close to each other. This effect seems to dominate over any other adhesive effects that may exist.

Next, gel blocks incorporating alginate and collagen (1% w/w and 1.5mg/mL respectively) and prepared using DI water were tested. Both nanosilica and SiC suspensions improved the adhesion strength with the addition of collagen to the hydrogel (Alg-Col) (0.52 ± 0.05 and 0.55 ± 0.09 kPa for nanosilica and SiC respectively in comparison to 0.38 ± 0.07 kPa for control samples without any adhesive as shown in FIG. 4.4). Successful bonding of gelatin using nanosilica solution has previously been reported [25]. Since gelatin is derived from collagen, it is expected to follow a similar bonding scheme where the adsorption of multiple polymer chains onto the surface of a single nanoparticle causes the nanosilica particles to act as connectors between the gel interfaces and result in adhesion between layers. SiC also demonstrated effective bonding in Alg-Col gels. Similarly to nanosilica, this can be explained in terms of particle adsorption that occurs due to electrostatic interaction [26]. SiC nanoparticles have an isoelectric point of 4.9 and are typically negatively charged in physiological pH [27]. Collagen is zwitterionic and contains both positive and negatively charged groups. Therefore, the nanoparticles are likely to bond to positively charged amino acids groups on the collagen through electrostatic interactions, which leads to an effective increase in bond strength. In contrast, when using water-based gels consisting of only alginate, bonding with SiC nanoparticles proved to be ineffectual as alginate contains little charges groups unlike collagen.

We then tested the alginate gels prepared using cell media instead of DI water. Since the intention is to seed cells into the gels, incorporation of cell growth media (EBM) into these gels will be critical. Surprisingly, the adhesion strength of the control (Alg-EBM gels pressed with one another) significantly reduced (0.1 ± 0.04 kPa) as compared to those prepared using DI water, as shown in FIG. 4.4. This indicates that the

high ionic strength of the cell media (6.4g/L NaCl) can prevent significant ionic crosslinking between the chains from the different gel layers due to charge screening [28]. Indeed viscosity measurements on alginate have shown that higher ionic strength leads to lower viscosity resulting from weaker inter chain crosslinking [29]. These correspond well with our finding (*FIG. S4.1*) that the ultimate tensile strength of the Alg-EBM gel is lower than the Alg-water gel due to weaker inter-chain interaction.

Interestingly, the nanoparticle adhesives were able to significantly improve the adhesion strength between Alg-EBM hydrogel blocks (0.27 ± 0.04 kPa and 0.39 ± 0.07 kPa for nanosilica and SiC respectively, as shown in *FIG. 4.4*). The enhancement can be attributed to binding of peptides in the EBM to the nanoparticles, which may result in aggregation of the particles and binding of the gels to the particles. Past work has shown that colloidal nanosilica flocculate in solution in the presence of amino peptides [30]. Such interaction was also observed in our experiments resulting in formation of a thin white precipitate layer, which may have resulted in enhanced adhesion when the two gel layers are brought in contact. We hypothesize that nanosilica and SiC, precipitate on to the surface of the gel and bind with the peptide chains that are present. The large surface of the particles provides multiple anchoring locations, which facilitates the increase in bond strength.

Finally, we tested hybrid alginate and collagen containing gels blocks prepared using cell media (Alg-Col-EBM) and found that both the nanosilica and the SiC substantially improved the adhesion strength between them (Alg-Col-EBM) (0.43 ± 0.1 , and 0.39 ± 0.03 kPa for nanosilica and SiC samples respectively in comparison to 0.08 ± 0.04 kPa for control samples as shown in *FIG. 4.4*). Without the nanoparticle adhesives, the bond strength is weak and microchannel networks formed using this method is likely to leak. The administration of SiC and nanosilica on hybrid media-based gels resulted in bond strengths that surpassed the mechanical strength of the bulk gels themselves. This resulted in failure at the bulk gel as opposed to interfacial delamination at the joint, as was the case for all other materials. The type of bond failure was assessed in detail for varying materials, time, and concentration in *Supplementary Section S2*. These experiments demonstrate that SiC nanoparticle solutions can significantly improve the adhesion strength of collagen containing gels prepared using cell growth media

solutions and therefore are ideally suited to serve as adhesives for layer by layer assembly of thick gels with integrated perfusion networks. Nanosilica which has been previously used to as a high strength tissue adhesive serves as a suitable comparison to our silicon carbide nanoparticle adhesive. As shown in our work, we are able to achieve similar bonding strengths with SiC in comparison to nanosilica, while at the same time achieving high microchannel resolutions that are not possible with nanosilica.

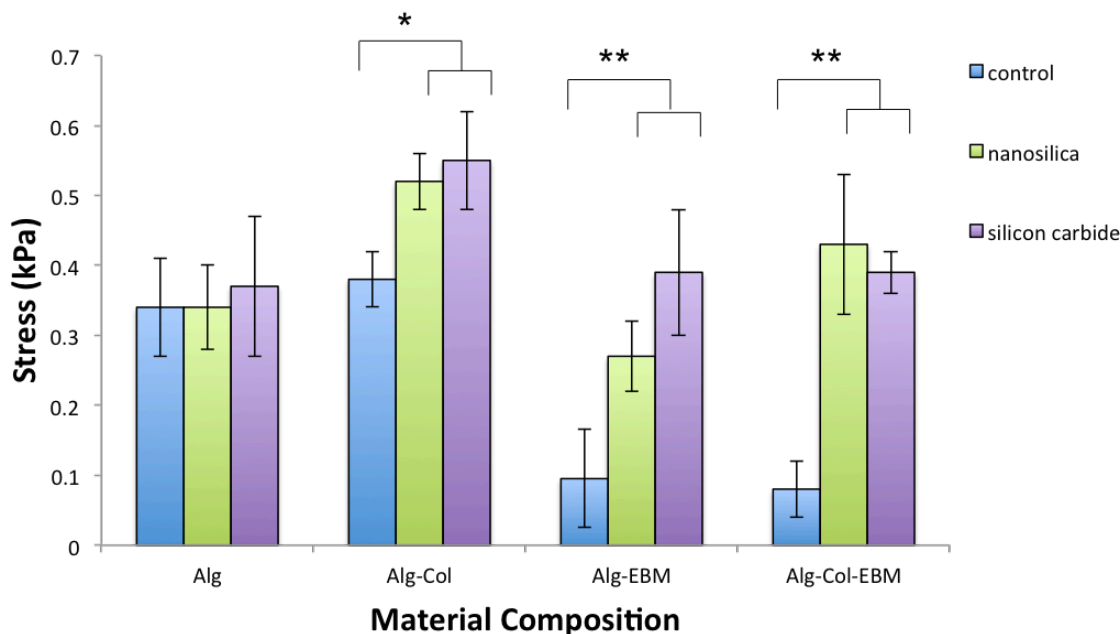


FIG. 4.4: Lap shear tests were performed on hydrogel samples of varying material compositions, adhered using nanosilica solution or SiC. Control values indicate samples tested without any interfacial adhesive applied. Both adhesives were found to be ineffective with water-based alginate alone, while nanosilica and SiC demonstrated some effect upon the incorporation of collagen. Both adhesives achieved successful bonding to varying degrees when used with media-based alginate or hybrid hydrogels. Single asterisks (*) represent p -level < 0.05 and double asterisks (**) p -level < 0.01 , indicating a significant difference between groups.

3.3 Effect of adhesive concentration and time on bond strength:

We also characterized the influence of concentration of the nanoparticle concentration on the adhesive strength to determine the minimum concentration suitable for our application. Hydrogel blocks composed of alginate and collagen were prepared and bonded together using nanoparticle adhesives as described in the methods section. Concentrations of the adhesive solution were varied from 0.001-1%, and 10-50% for SiC

and nanosilica solution respectively. Any concentration below 10% for nanosilica was similar to the control case and therefore is not reported. All samples were maintained in solution to prevent dehydration. Lap shear tests were performed on these samples to identify optimal concentrations for each adhesive to establish a strong bond between layers ($n=5$) (FIG. 4.5). It was found that the strongest adhesion with SiC occurred at a concentration of 0.01% ($0.39 \pm 0.03 \text{ kPa}$) (FIG. 4.5a). This concentration coincides well with the documented water solubility limit of SiC nanoparticles. At higher concentrations, nanoparticles aggregated and settled over time. Formation of aggregates prevents conformal contact between the gel layers and leads to poor bonding. In the case of nanosilica solution, the adhesive strength was low until the concentration was 20%. It then increased as the concentration was increased to 30% ($0.51 \pm 0.08 \text{ kPa}$) (FIG. 4.5b) and remained more or less the same upon further increase. At this concentration, the solution was found to transition to a sol gel state.

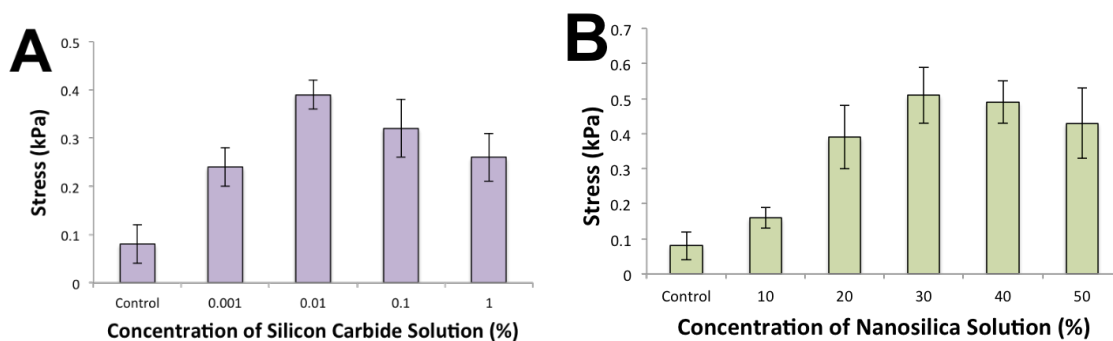


FIG. 4.5: Lap shear tests performed on media-based composite gel samples with varying concentrations of each adhesive. A) Maximum stress values for hydrogel samples with 0.001-1% SiC. Maximum bond strength was found to occur at 0.01% concentration. B) Maximum stress values for hydrogel samples with 10-50% nanosilica solution. Bond strengths were maximized at concentrations of $\geq 30\%$.

We also examined whether the adhesive strength improved over the time after bonding. In this test, Alg-Col-EBM gel samples were bonded with SiC and nanosilica adhesives and allowed to age for varying durations of time from 1-48 hrs before testing. The results ($n=5$), shown in FIG. 4.6, demonstrate that the adhesive strength of the SiC bonded interface increased gradually until ~ 24 hrs indicating a slow integration and binding of the nanoparticles to the polymers in the gel. In contrast, the adhesive strength

of the gel layers bonded with nanosilica adhesive was found to rapidly reach the maximum within 3hrs, likely due to the significantly higher concentrations used. Previous studies on nanosilica have shown instantaneous bonding [25] but have not tested the time to achieve the maximum bond strength. These results show that the adsorption of the polymer chains onto the nanoparticle reach equilibrium at 3hrs for nanosilica.

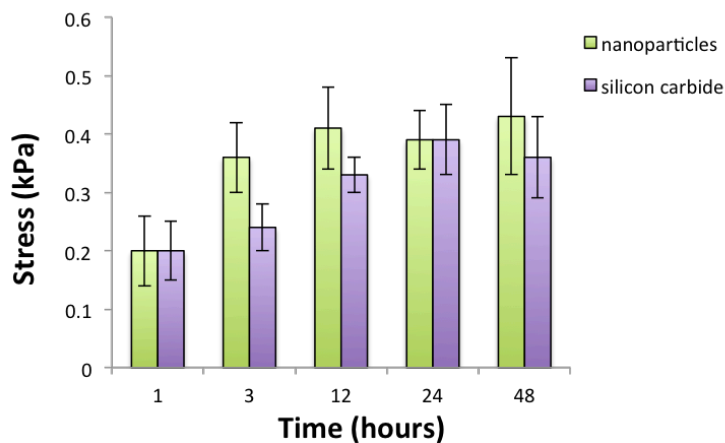


FIG. 4.6: Lap shear tests performed on media-based composite gels to determine the time duration required for bonding to reach completion. Bonding strengths of SiC and nanosilica compared over a 48hour time period. It was found that nanosilica required >3hours to reach maximum bond strength, while SiC required >12hours.

3.4 Cytotoxicity testing of adhesives:

The hydrogels used throughout our experiments are some of the most commonly used biomaterials used for scaffold fabrication in tissue engineering applications. As such, it is important to determine the cytotoxic effects of each of the adhesives and to determine their suitability for tissue engineering applications. Mouse 3T3 fibroblasts were cultured and harvested at concentrations of 2.5×10^6 cells/mL. Cells were seeded within media-based alginate and collagen composite gels, and cast into 0.5mm thick gel films that were then cut into 1x1cm sections. Cell viability was $96.67 \pm 2.1\%$ prior to embedding in gel structures. Cell seeded samples were coated with each adhesive (0.01% and 50% of SiC and nanosilica respectively) and then maintained in media for 7 days ($n=3$). Cell culture media was renewed every 48 hours. Live and dead stain images of the samples were taken on day 1, day 3, and day 7 of the experiment (FIG. S4.5) and compared to a control sample with no adhesive administration. The thinness of these gel

films allows for sufficient nutrient diffusion from the surrounding media to easily penetrate through the films to the embedded cells, thereby creating an environment where exposure to the adhesive is the only common factor affecting viability.

On day 1, all samples demonstrated good live cell density (697.75 ± 86.4 , 720.4 ± 53.02 and 451 ± 100 cells/mm² for the control, SiC, and nanosilica respectively) (FIG. 4.7). There was a slight decrease in comparison to pre-casting cell counts, likely due to cell death occurring during resuspension in viscous uncrosslinked gel solution [31]. On day 3 and day 7, a significant decrease in live cell density within the gel was observed in samples with nanosilica (165.75 ± 14.9 cells/mm² and 44 ± 17.35 cells/mm²). Surprisingly, the cell density remained nearly the same for gels with SiC coating (654.71 ± 64.11 cells/mm² and 580.2 ± 109.7 cells/mm² on day 3 and day 7 respectively, which was comparable to the control samples at 672 ± 84.36 cells/mm² and 562.4 ± 95.68 cells/mm²). Although silica nanoparticles have been used as an adhesive of biological tissues before, the effect of these adhesives [25] on survival of cells have not been investigated. Our results suggest that high concentrations of nanoparticles may have a detrimental effect at least in layers of gel close to the nanoparticles. Lower concentrations of nanoparticles as used in the case of SiC are more suitable and do not seem to affect cell population. This result demonstrates that nanosilica may not be a suitable adhesive for layer-by-layer assembly of gel layers to fabricate hydrogel constructs. Since each individual layers will be 500 μ m to 1 mm, the effect on nanosilica on cell viability will be significantly detrimental. It also demonstrates that SiC would be an ideal inter-layer adhesive for this application, as confirmed by the high cell viability maintained within the hollow channel structures shown FIG. S4.6. Although silicon carbide is a ceramic that is well known for its biocompatibility, its nanoparticle form has raised concerns regarding cellular uptake and the potential negative responses that this could cause. Several groups have studied the impact of intracellular accumulation on cytotoxicity, genotoxicity, oxidative stress, and pro-inflammatory response in cells [32,33], and found that changes occurred only at concentrations higher than 50 μ g/mL. Our work utilizes a much lower SiC concentration of 10 μ g/mL where no significant changes have been shown to occur, making this a suitable strategy for tissue engineering applications.

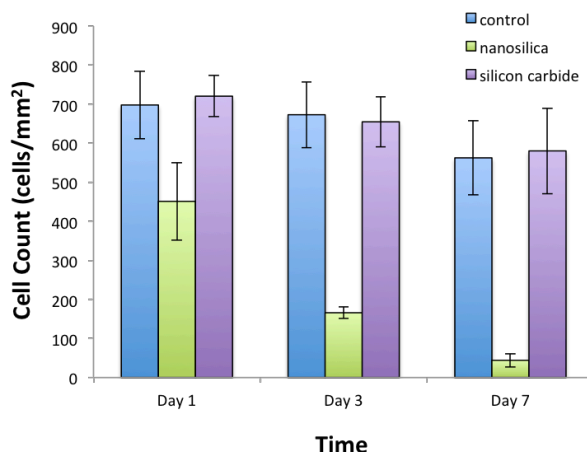


FIG. 4.7: Cytotoxic evaluation of various adhesives when administered onto cell seeded media-based hybrid gels. Comparison of live cell counts (acquired with ImageJ) within samples exposed to each adhesive over a 7-day period. Culture media was renewed every 48hrs. Live cell count maintained in SiC samples, while a significant reduction in cell count was observed in nanosilica samples.

3.5 Adhesion of hydrogels to hard substrates:

During experimentation, we discovered the ability to use nanosilica solution to adhere hydrogels to hard surfaces such as glass (FIG. S4.7). As a demonstration, a 0.5mm thick media-based hybrid gel film, measuring 1x2.5mm, was adhered to a No.1 60x22mm cover glass using 250 μ L of nanosilica solution. Mechanical testing revealed the formation of a strong and effective bond between the two surfaces (n=5) and failure occurred in the bulk of the gel (FIG. 4.8) rather than delamination of the interface. It is expected that the nanosilica solution would successfully adhere to the glass substrate, as nanosilica has commonly been used in the past to liquid glass coatings [34-36]. Indeed, the ability to adhere soft material gels to hard surfaces can be advantageous in applications involving biomaterial coating of substances. Surfaces that initially may not lend themselves well to cell seeding and adherence could then be modified and coated with soft scaffolding materials that would allow for the growth of various cell cultures. This could also allow the creation of heterogeneous, multilayered structures with the incorporation of both hard and soft materials that would thereby improve upon both the mechanical and biocompatible characteristics of the construct as a whole.

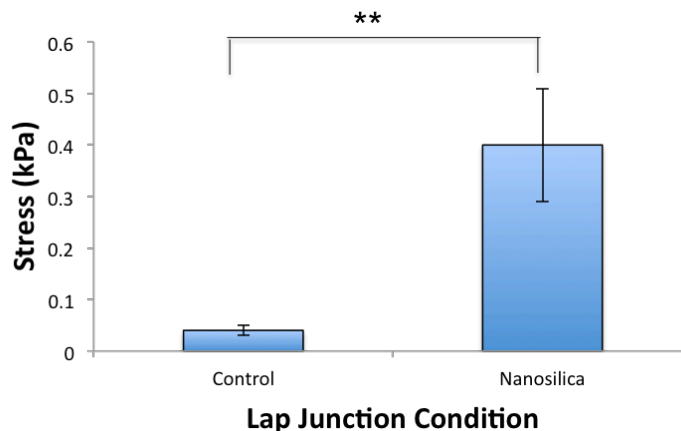


FIG. 4.8: Ultimate stress values for bonding of media-based hybrid gels to No.1 coverglass. Control values represents lap junction where no adhesive was administered. Double asterisks (**) represent p-level<0.01, indicating a significant difference between groups.

Although nanosilica solution was unsuccessful for fabrication of high-resolution channels and also resulted in low cell viability, it proved useful in creating inlet and outlet connections by adhering polyvinyl chloride (PVC) tubing to the gel structures. This is not surprising, as coagulation and adsorption of silica in the presence of PVC has previously been observed [37] and there have been several reported cases of PVC/silica composite fabrication [38-40]. Gel structures with a 2mm embedded hollow channel were fabricated via adhesion with nanosilica solution (FIG. 4.9a-i), and a 2mm Tygon tube was inserted 5mm into the length of channel (FIG. 4.9a-ii). After deposition of 100 μ L of nanosilica onto the overlapping junction, the hollow channel could easily be perfused after 1hr (FIG. 4.9a-iii). Mechanical testing (FIG. S4.8) revealed a strong bond had been formed between the two interfaces (n=3) (FIG. 4.9b). It is also possible that interconnects be formed using glass, as we have confirmed strong adhesion of hydrogels to glass substrates using nanosilica.

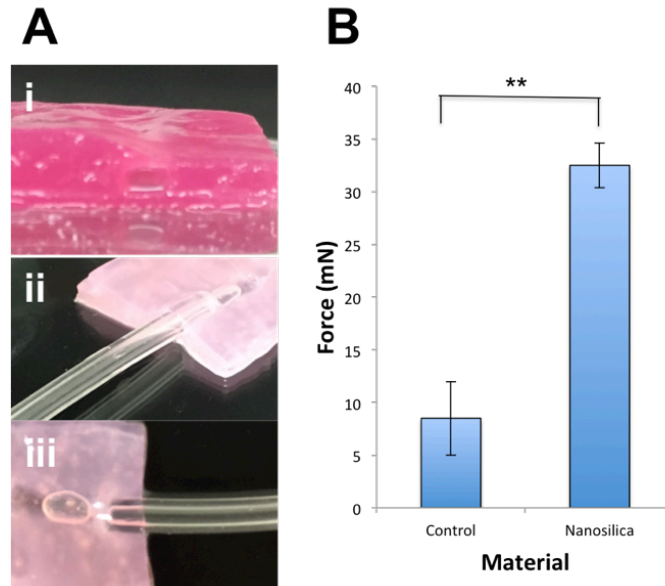


FIG. 4.9: A) i) Cross-sectional image of 2mm embedded hollow channel in media-based composite hydrogel, post adhesion using nanosilica solution. ii) PVC tube (2mm diameter) was inserted 5mm into the hollow channel. The junction was sealed using 100 μ L of nanosilica. iii) Air bubble was injected into the tube, demonstrating the continuity between the tube and hollow channel. B) Mechanical tests were performed to determine the effectiveness of the bond between the tube and channel. Double asterisks (**) represent p-level $<$ 0.01, indicating a significant difference between groups.

Supplementary Section

Section S1: Determination of Adhesive Concentration Testing Range

The visual effects of adhesive administration to the hydrogel samples are important, as they are indicative of potential interactions between the various materials. The range of adhesive concentrations to be tested was also determined primarily based on observed qualitative changes in the test sample appearance following administration of a specific adhesive. In the case of silicon carbide, the sample did not appear to undergo any change that could be visualized and appeared similar to the control sample in appearance (*FIG. S4.9a,c*). At higher concentrations (1%), there were noted instances where particle aggregates could be seen on the gel surface. Nano-powders are often made of agglomerates that are 10-20 times larger than the primary nanoparticles [41]. In the case of silicon carbide, individual particles were found to be ~25nm (*FIG. S4.10b*) but formed aggregates at higher concentrations that were a few micrometers in size (*FIG. S4.10a*). Because the documented solubility for silicon carbide in water is approximately 0.01%, we chose a concentration testing range between 0.001-1% in order to fully encompass the full transition from diluted to aggregate adhesive solutions.

The nanosilica solution caused the hydrogel specimens to become opaque or cloudy in appearance following approximately 15min of settling time (*FIG. S4.9b,d*). The consistency of the administered solution was also found to change from liquid to solid phase. At higher concentrations (>20%), the solution became completely solidified whereas it achieved a semi-solid state at lower concentrations ($\leq 20\%$). Imaging revealed individual nanoparticles to be ~25-30nm in size (*FIG. S4.10c*), which settled to form a solid gel like layer at higher concentrations. We tested nanosilica concentrations between 10-50% in order to determine the effects of semi-solid to solid phase transition on bonding capabilities.

Section S2: Types of Adhered Bond Failure

We examined the types of bond failure that occurred with each of the various types of hydrogels (*FIG. S4.11a*). The water-based samples underwent failure at the joint

in the case of both adhesives, meaning that the lap junctions separated by means of interfacial peeling (*FIG. S4.12*). This is due in part to the rigidity and strong mechanical properties of the hydrogel as well as the comparatively low or non-existent bond strength. Such was also the case when using media-based alginate specimens. Although the bond strength was notably higher than the control, it was not sufficiently stronger than the gel itself thereby causing failure to happen at the joint. *FIG. S4.11c* illustrates a sample force-displacement curve for samples experiencing interfacial during mechanical testing. However, administration of silicon carbide or nanosilica solution onto media-based composite gels achieved effecting bonding that was as strong or stronger than the gel material itself. This in turn, caused fracture to occur outside the junction by means of gel tearing (*FIG. S4.13*), thereby producing a force-displacement curve similar to that seen in *FIG. S4.11d*.

We investigated the effect of time and adhesive concentration on the type of bond failure that would occur, specifically for media-based hybrid gels with silicon carbide and nanosilica (n=5). Time tests were performed using concentrations of 0.01% and 50% SiC and nanosilica respectively, and concentration experiments were carried out 48hrs post adhesive deposition. We determined that test samples adhered using nanosilica solutions failed by gel tearing 80-100% of the time when the duration of the experiment exceeded 1hr (*FIG. S4.11e*) and at concentrations greater than 30% (*FIG. S4.11f*). Tensile tests of gel samples coated in nanosilica were performed (*FIG. S4.14*) in order to determine fracture strength of bulk gels when exposed to various concentrations of this solution (*FIG. S4.11b*). Samples were tested at 48hrs post deposition of 200ul of solution. It was found that peak strength was achieved at 30% ($0.55\pm 0.06\text{kPa}$) concentration due to the formation of the hard shell coating surrounding the test sample. However, fracture strength decreased slightly at concentrations of 40% and 50% (0.46 ± 0.05 and $0.42\pm 0.02\text{kPa}$ respectively), which can likely be attributed to the increased brittleness and reduced elasticity of the sample. Because bond strength at 50% was found to be $0.43\pm 0.1\text{kPa}$, which is greater or equal to the strength of the gel itself, this explains the reason for 100% failure rate by tearing. Bond strength values at 30% and 40% (0.51 ± 0.08 and $0.49\pm 0.06\text{kPa}$ respectively) were less than or equal to the corresponding fracture strength, thereby explaining the decrease in frequency of failure by tearing.

Samples adhered using silicon carbide failed by tearing much less frequently in comparison to those bonded with nanosilica. Test samples experienced only 20% failure by tearing after 24hrs (*FIG. S4.11g*) as well as at concentrations of 0.01% and 0.1% (*FIG. S4.11h*). Application of SiC solution did not result in any phase changes or additional reinforcement to the sample, as was the case with nanosilica. Therefore, the fracture strength of the gels was $0.42 \pm 0.08 \text{ kPa}$, similarly to the reported control value in *FIG. S4.11b*. The bond strengths at 0.01% and 0.1% were 0.39 ± 0.03 and $0.32 \pm 0.06 \text{ kPa}$ respectively. The low occurrence of failure by tearing can therefore be explained by lower bond strength comparative to the gel fracture strength.

Material	Water-Based Alginate	Water-Based Alginate/Collagen	Media-Based Alginate	Media-Based Alginate/Collagen
Ultimate Tensile Stress (kPa)	4.64 ± 0.11	3.15 ± 0.09	1.83 ± 0.07	0.42 ± 0.08

FIG. S4.1: Ultimate tensile stress for various materials due to changes in ionic strength.

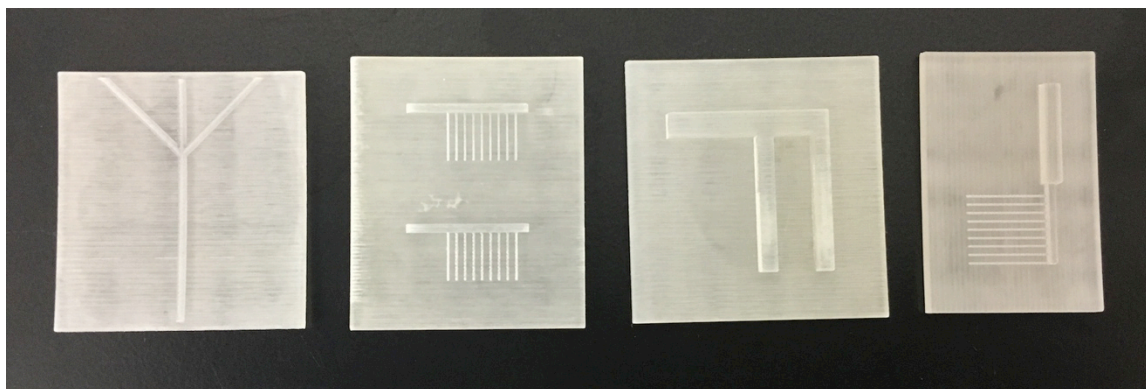


FIG. S4.2: Several 3D printed acrylic molds used for casting of hydrogel layers with embedded hollow channels networks of varying dimensions.

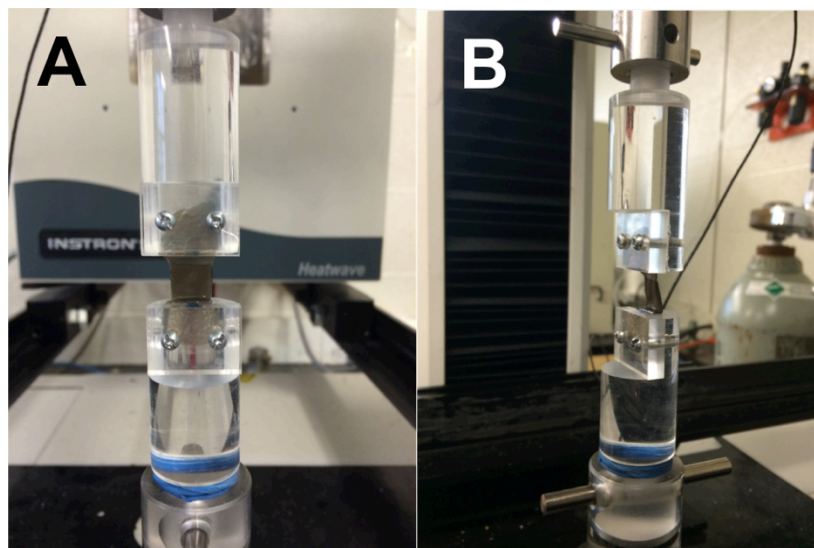


FIG. S4.3: Mechanical testing apparatus and setup using stained gel. A) Instron machine used for mechanical testing of adhered hydrogel specimens. B) Custom-made grippers used for stabilization of delicate samples.

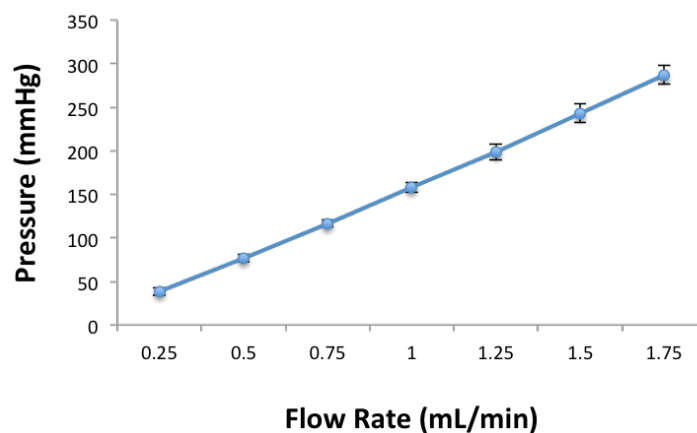


FIG. S4.4: Using a pressure transducer (Edwards Lifesciences LLC, Irvine, CA, USA) and patient monitor (SpaceLabs 90369 Patient Monitor, SpaceLabs Medical Inc.), pressure testing performed by perfusing of a single 200x400 μ m hollow channel that was fabricated with silicon carbide as an adhesive. Perfusion flow rates were varied in a step-wise manner, and the corresponding pressures were recorded. The channel was found to successfully withstand high pressures, upwards of 300mmHg.

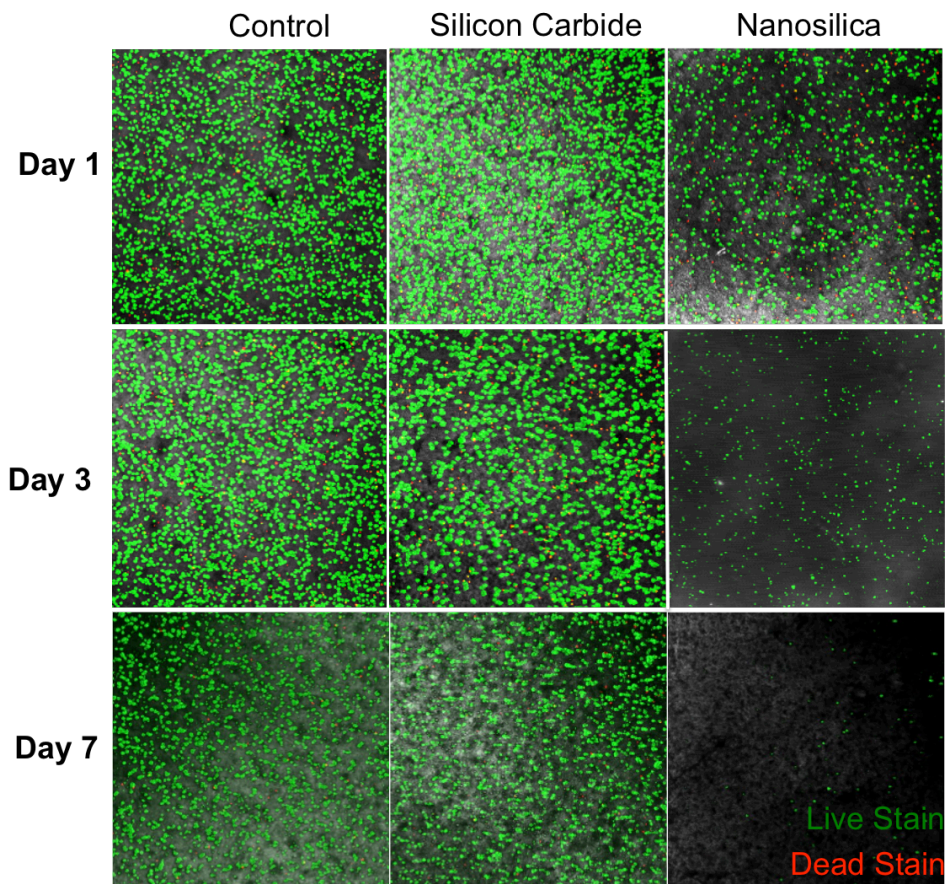


FIG. S4.5: Z-stack montages obtained using confocal microscopy, showing live and dead stain of cells embedded within media-based composite hydrogels post exposure to various adhesives. Samples were imaged on day 1, day 3, and day 7 for analysis and compared to a control with no adhesive exposure. Culture media for all samples was renewed every 48hrs. Silicon carbide samples showed good maintenance of cell viability, similarly to the control samples. Nanosilica samples experienced diminished live cell counts by day 3 despite showing promising results within the first 24hours.

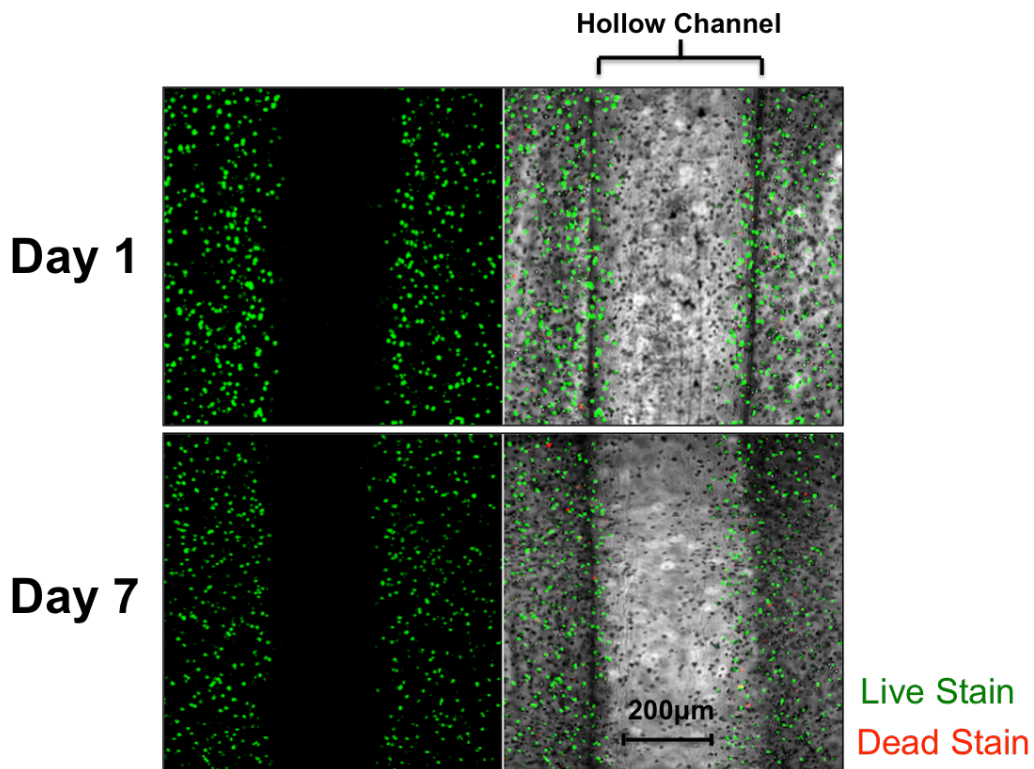


FIG. S4.6: Confocal microscopy used to obtain fluorescent images of cell-laden patterned hydrogel constructs adhered using silicon carbide. Images show live and dead stain of 3T3 cells embedded in gel surrounding a 400µm patterned hollow channel over a 7-day period.

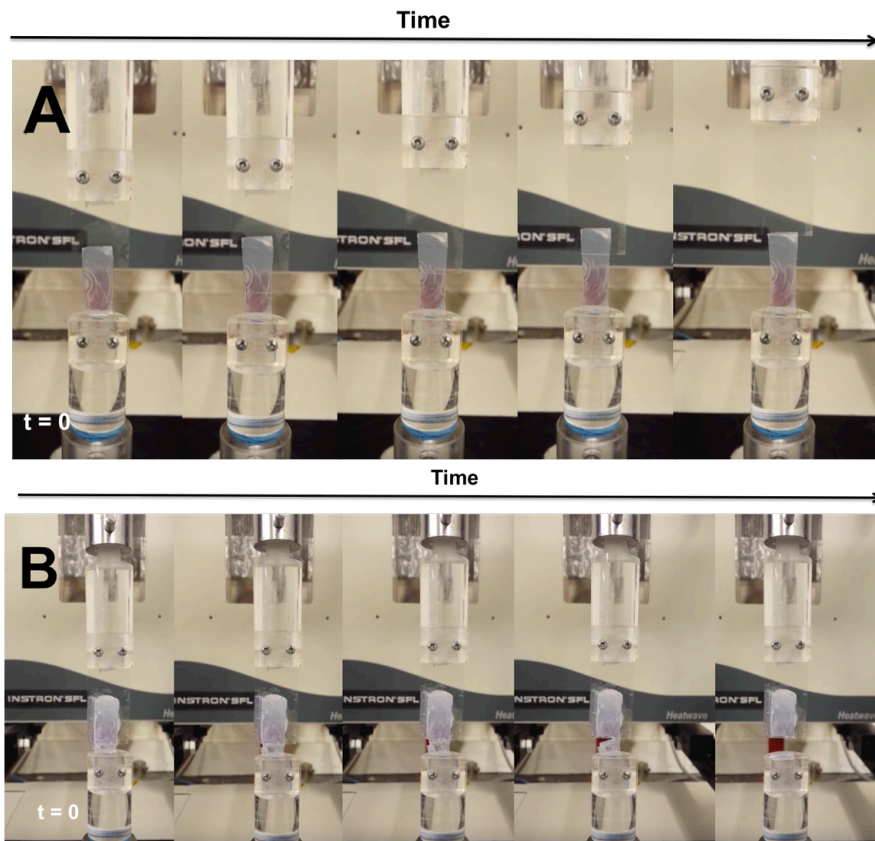


FIG. S4.7: A) Lap shear test of media-based composite gel and No.1 coverglass overlap junction. No adhesive was used, and failure occurred due to peeling at surfaces. B) Lap shear test of media-based composite gel adhered to No.1 coverglass using nanosilica solution. Sample undergoes failure due fracture of the gel outside of the lap junction (failure at by tearing).

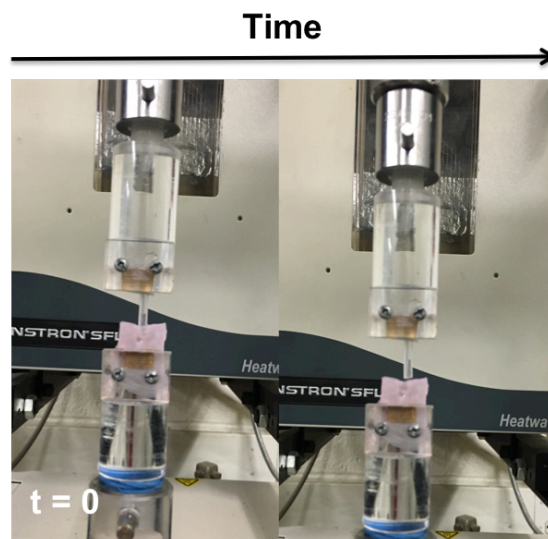


FIG. S4.8: Mechanical tests performed polyurethane/composite gel connection to determine the efficacy of the nanosilica in creating a strong bond at the overlapping junction.

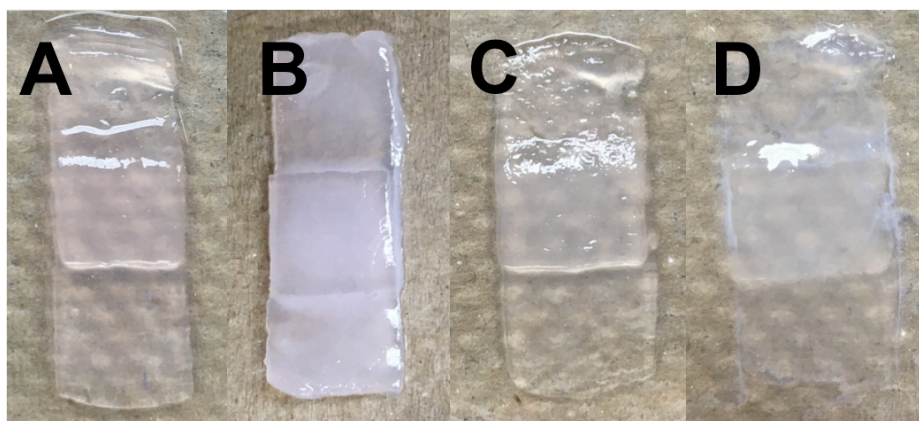


FIG. S4.9: Qualitative observation of alginate-collagen hybrid gel samples upon administration of various adhesives. Similar observations were seen for alginate samples in the absence of collagen. Images seen in A,B were fabricated using media-based solutions, while images in C,D were water-based. A) Administration of silicon carbide solution did not cause any observable physical change. The sample remained similar in appearance to a control sample with no adhesive administration. B) Sample with nanosilica solution deposition became opaque in appearance as the nanosilica solidified C) Similarly to media-samples, silicon carbide did not cause any observed physical change to the water-based sample seen here. Control samples also remained similar in appearance. D) Nanosilica administration to the water-based hybrid gel caused the sample to become opaque and cloudy.

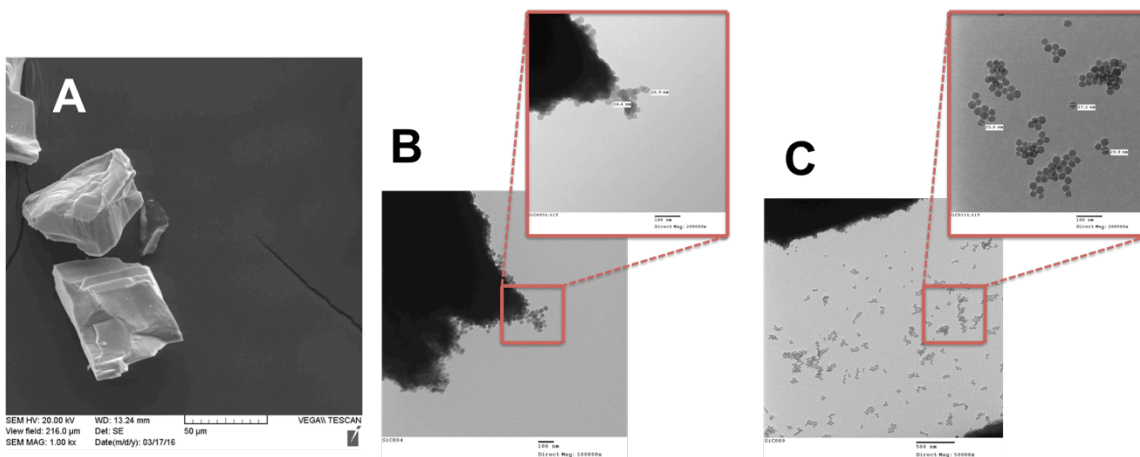


FIG. S4.10: Imaging of silicon carbide and silica nanoparticles. A) SEM of silicon carbide. Nanoparticles were found to form micron sized agglomerates. B) TEM of primary silicon carbide nanoparticles. C) TEM of nanosilica solution forms a solid layer, but nanoparticles could be observed in between cracks that formed within the layer.

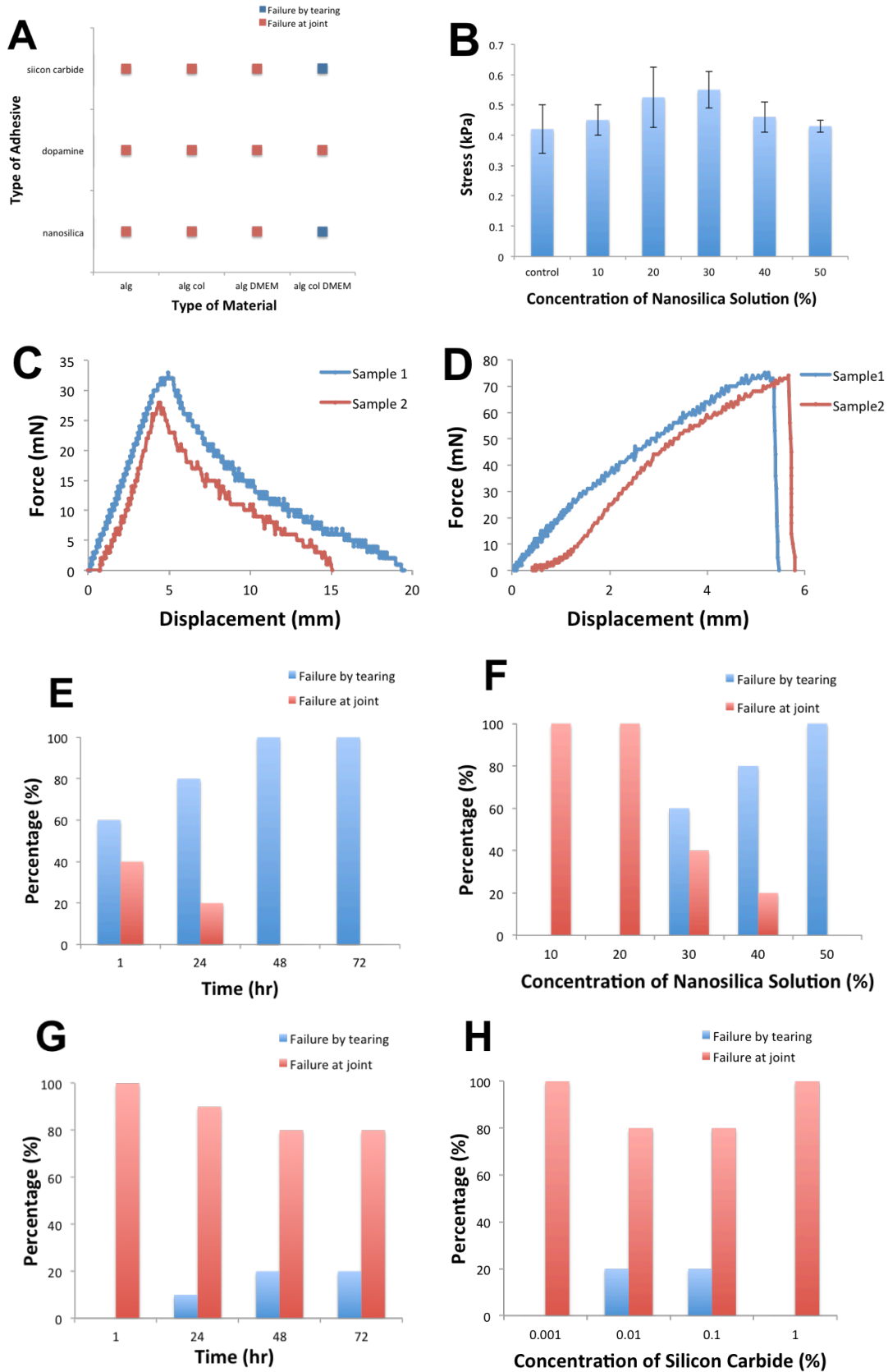


FIG. S4.11: A) Characterization of the type of bond failure occurring with each adhesive using various biomaterials: water-based alginate (Alg), water-based alginate/collagen composite (Alg-Col), media-based alginate (Alg-EBM), and media-nased alginate/collagen composite (Alg-Col-EBM). Bond strengths of nanosilica solution and silicon carbide on Alg-Col-EBM samples exceeded the strength of the gel itself, causing fracture by tearing. All other samples failed due to interfacial peeling (failure at joint). B) Tensile tests of Alg-Col-EBM samples coated with various concentrations of nanosilica solution. Coating appeared to reinforce the hydrogel samples. Peak strength occurred at 30% concentration, after which point increased brittleness and reduced elasticity caused samples to fracture at lower stresses. C) Sample force-displacement curve for Alg-EBM gel using nanosilica as an adhesive. All samples that underwent interfacial failure at the joint resulted in similar graphs. D) Sample force-displacement curve for Alg-Col-EBM gel using nanosilica solution as an adhesive. All samples that underwent fracture by tearing resulted in similar graphs. Effect of E) time and F) concentration on the type of failure occurring using nanosilica on Alg-Col-EBM. Frequency of fracture failure increased with time and concentration (80-100% tearing failure rate when >1hrs and $\geq 40\%$). Effect of G) time and H) concentration on the type of failure occurring using silicon carbide on Alg-Col-EBM. Frequency of fracture failure increased slightly when ≥ 24 hrs (10-20% tearing failure rate) and at concentrations of 0.01% and 0.1% (10-20% tearing failure rate).

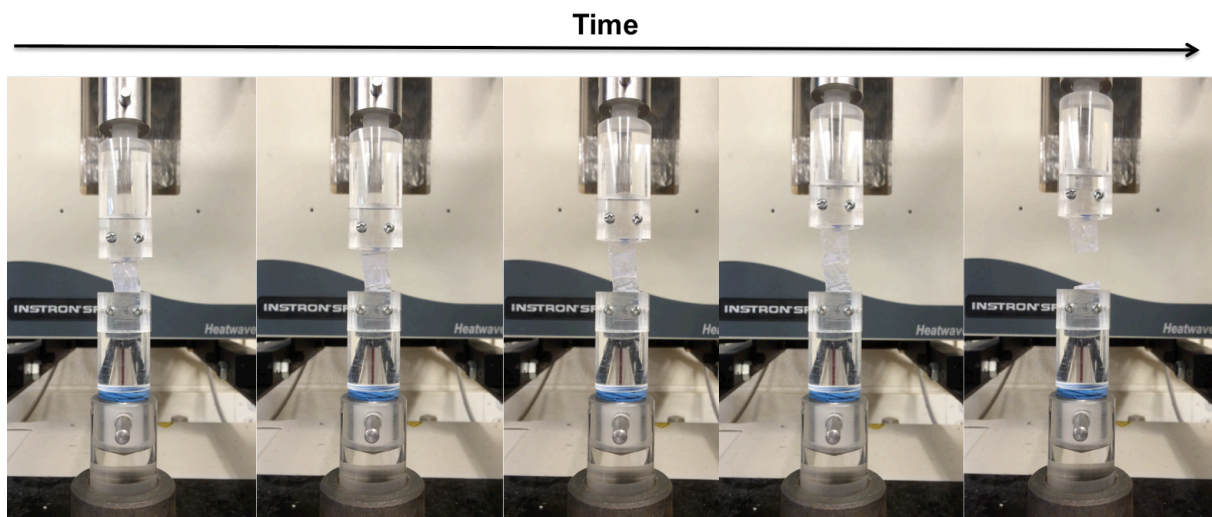


FIG. S4.12: Lap shear test of water-based composite gel adhered using silica. Sample undergoes failure due to interfacial peeling between the two surfaces (failure at joint).

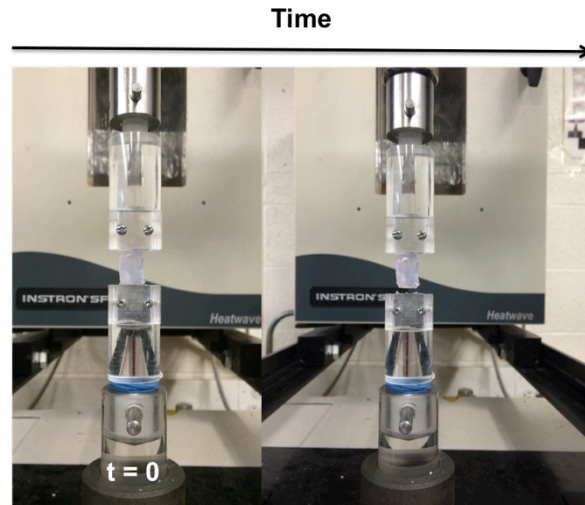


FIG. S4.13: Lap shear test of media-based composite gel adhered using nanosilica solution. Sample undergoes failure due fracture of the gel outside of the lap junction (failure at by tearing).

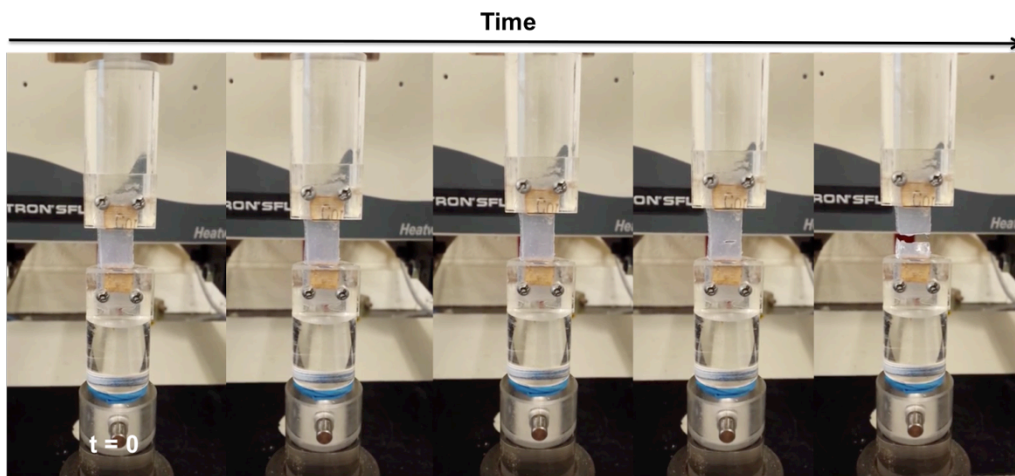


FIG. S4.14: Tensile tests performed on of media-based composite gels with and without outer coating of nanosilica solution.

References

- [1] R. Attalla, C. Ling, and P. Selvaganapathy, "Fabrication and characterization of gels with integrated channels using 3D printing with microfluidic nozzle for tissue engineering applications," *Biomedical microdevices*, vol. 18, no. 1, pp. 1-12, 2016.
- [2] L. E. Bertassoni *et al.*, "Hydrogel bioprinted microchannel networks for vascularization of tissue engineering constructs," *Lab on a Chip*, vol. 14, no. 13, pp. 2202-2211, 2014.
- [3] J. S. Miller *et al.*, "Rapid casting of patterned vascular networks for perfusable engineered three-dimensional tissues," *Nature materials*, vol. 11, no. 9, pp. 768-774, 2012.
- [4] A. P. Golden and J. Tien, "Fabrication of microfluidic hydrogels using molded gelatin as a sacrificial element," *Lab on a Chip*, vol. 7, no. 6, pp. 720-725, 2007.
- [5] S. V. Murphy and A. Atala, "3D bioprinting of tissues and organs," *Nature biotechnology*, vol. 32, no. 8, pp. 773-785, 2014.
- [6] K. H. Lee, S. J. Shin, Y. Park, and S. H. Lee, "Synthesis of cell-laden alginate hollow fibers using microfluidic chips and microvascularized tissue-engineering applications," *Small*, vol. 5, no. 11, pp. 1264-1268, 2009.
- [7] V. K. Lee, A. M. Lanzi, H. Ngo, S.-S. Yoo, P. A. Vincent, and G. Dai, "Generation of multi-scale vascular network system within 3D hydrogel using 3D bio-printing technology," *Cellular and molecular bioengineering*, vol. 7, no. 3, pp. 460-472, 2014.
- [8] W. Lee *et al.*, "On-demand three-dimensional freeform fabrication of multi-layered hydrogel scaffold with fluidic channels," *Biotechnology and bioengineering*, vol. 105, no. 6, pp. 1178-1186, 2010.
- [9] Z. Wang, R. Abdulla, B. Parker, R. Samanipour, S. Ghosh, and K. Kim, "A simple and high-resolution stereolithography-based 3D bioprinting system using visible light crosslinkable bioinks," *Biofabrication*, vol. 7, no. 4, p. 045009, 2015.
- [10] N. Annabi *et al.*, "Controlling the porosity and microarchitecture of hydrogels for tissue engineering," *Tissue Engineering Part B: Reviews*, vol. 16, no. 4, pp. 371-383, 2010.
- [11] S. N. Bhatia and D. E. Ingber, "Microfluidic organs-on-chips," *Nature biotechnology*, vol. 32, no. 8, pp. 760-772, 2014.
- [12] S. Muehleder, A. Ovsianikov, J. Zipperle, H. Redl, and W. Holthoner, "Connections matter: channeled hydrogels to improve vascularization," *Frontiers in bioengineering and biotechnology*, vol. 2, p. 52, 2014.
- [13] Y. Ling *et al.*, "A cell-laden microfluidic hydrogel," *Lab on a Chip*, vol. 7, no. 6, pp. 756-762, 2007.
- [14] J. P. Gleghorn, C. S. Lee, M. Cabodi, A. D. Stroock, and L. J. Bonassar, "Adhesive properties of laminated alginate gels for tissue engineering of layered structures," *Journal of biomedical materials research Part A*, vol. 85, no. 3, pp. 611-618, 2008.
- [15] M. Cabodi, N. W. Choi, J. P. Gleghorn, C. S. Lee, L. J. Bonassar, and A. D. Stroock, "A microfluidic biomaterial," *Journal of the American Chemical Society*, vol. 127, no. 40, pp. 13788-13789, 2005.

- [16] X. Mu, W. Zheng, L. Xiao, W. Zhang, and X. Jiang, "Engineering a 3D vascular network in hydrogel for mimicking a nephron," *Lab on a Chip*, vol. 13, no. 8, pp. 1612-1618, 2013.
- [17] B. Chevallay and D. Herbage, "Collagen-based biomaterials as 3D scaffold for cell cultures: applications for tissue engineering and gene therapy," *Medical and Biological Engineering and Computing*, vol. 38, no. 2, pp. 211-218, 2000.
- [18] K. Y. Lee and D. J. Mooney, "Alginate: properties and biomedical applications," *Progress in polymer science*, vol. 37, no. 1, pp. 106-126, 2012.
- [19] C. K. Kuo and P. X. Ma, "Ionically crosslinked alginate hydrogels as scaffolds for tissue engineering: part 1. Structure, gelation rate and mechanical properties," *Biomaterials*, vol. 22, no. 6, pp. 511-521, 2001.
- [20] K. Wang, P. Drayton, B. Frame, J. Dunwell, and J. Thompson, "Whisker-mediated plant transformation: an alternative technology," *In Vitro Cellular & Developmental Biology-Plant*, vol. 31, no. 2, pp. 101-104, 1995.
- [21] Y. Haj-Ahmad, "Nucleic acid purification and process," ed: Google Patents, 2001.
- [22] J. Fan, H. Li, J. Jiang, L. K. So, Y. W. Lam, and P. K. Chu, "3C-SiC nanocrystals as fluorescent biological labels," *Small*, vol. 4, no. 8, pp. 1058-1062, 2008.
- [23] S. Hoshika *et al.*, "Effect of application time of colloidal platinum nanoparticles on the microtensile bond strength to dentin," *Dental materials journal*, vol. 29, no. 6, pp. 682-689, 2010.
- [24] A. Naji and M.-F. Harmand, "Cytocompatibility of two coating materials, amorphous alumina and silicon carbide, using human differentiated cell cultures," *Biomaterials*, vol. 12, no. 7, pp. 690-694, 1991.
- [25] S. Rose, A. PrevotEAU, P. Elzière, D. Hourdet, A. Marcellan, and L. Leibler, "Nanoparticle solutions as adhesives for gels and biological tissues," *Nature*, vol. 505, no. 7483, pp. 382-385, 2014.
- [26] N. A. Peppas and P. A. Buri, "Surface, interfacial and molecular aspects of polymer bioadhesion on soft tissues," *Journal of Controlled Release*, vol. 2, pp. 257-275, 1985.
- [27] B. P. Singh, J. Jena, L. Besra, and S. Bhattacharjee, "Dispersion of nano-silicon carbide (SiC) powder in aqueous suspensions," *Journal of nanoparticle research*, vol. 9, no. 5, p. 797, 2007.
- [28] M. Schmidt, *Polyelectrolytes with defined molecular architecture I*. Springer Science & Business Media, 2004.
- [29] R. Pamies, R. R. Schmidt, M. d. C. L. Martínez, and J. G. de la Torre, "The influence of mono and divalent cations on dilute and non-dilute aqueous solutions of sodium alginates," *Carbohydrate Polymers*, vol. 80, no. 1, pp. 248-253, 2010.
- [30] T. Coradin, O. Durupthy, and J. Livage, "Interactions of amino-containing peptides with sodium silicate and colloidal silica: a biomimetic approach of silicification," *Langmuir*, vol. 18, no. 6, pp. 2331-2336, 2002.
- [31] Y. Chisti, "Hydrodynamic damage to animal cells," *Critical reviews in biotechnology*, vol. 21, no. 2, pp. 67-110, 2001.
- [32] S. Barillet *et al.*, "In vitro evaluation of SiC nanoparticles impact on A549 pulmonary cells: cyto-, genotoxicity and oxidative stress," *Toxicology letters*, vol. 198, no. 3, pp. 324-330, 2010.

- [33] J. Pourchez *et al.*, "In vitro cellular responses to silicon carbide nanoparticles: impact of physico-chemical features on pro-inflammatory and pro-oxidative effects," *Journal of Nanoparticle Research*, vol. 14, no. 10, p. 1143, 2012.
- [34] G. Wu *et al.*, "A novel route to control refractive index of sol-gel derived nanoporous silica films used as broadband antireflective coatings," *Materials Science and Engineering: B*, vol. 78, no. 2, pp. 135-139, 2000.
- [35] W. Li *et al.*, "Physical and optical properties of sol-gel nano-silver doped silica film on glass substrate as a function of heat-treatment temperature," *Journal of applied physics*, vol. 93, no. 12, pp. 9553-9561, 2003.
- [36] C. Su, J. Li, H. Geng, Q. Wang, and Q. Chen, "Fabrication of an optically transparent super-hydrophobic surface via embedding nano-silica," *Applied Surface Science*, vol. 253, no. 5, pp. 2633-2636, 2006.
- [37] A. Bleier and E. Matijević, "Heterocoagulation. Part 3.—Interactions of polyvinyl chloride latex with Ludox Hs silica," *Journal of the Chemical Society, Faraday Transactions 1: Physical Chemistry in Condensed Phases*, vol. 74, pp. 1346-1359, 1978.
- [38] S. Ulutan and D. Balköse, "Diffusivity, solubility and permeability of water vapor in flexible PVC/silica composite membranes," *Journal of membrane science*, vol. 115, no. 2, pp. 217-224, 1996.
- [39] S. Sun, C. Li, L. Zhang, H. Du, and J. Burnell-Gray, "Effects of surface modification of fumed silica on interfacial structures and mechanical properties of poly (vinyl chloride) composites," *European polymer journal*, vol. 42, no. 7, pp. 1643-1652, 2006.
- [40] A. Zhu, A. Cai, W. Zhou, and Z. Shi, "Effect of flexibility of grafted polymer on the morphology and property of nanosilica/PVC composites," *Applied surface science*, vol. 254, no. 13, pp. 3745-3752, 2008.
- [41] P. Bowen, C. Carry, D. Luxembourg, and H. Hofmann, "Colloidal processing and sintering of nanosized transition aluminas," *Powder Technology*, vol. 157, no. 1, pp. 100-107, 2005.

Chapter 5

CONCLUSIONS AND RECOMMENDATIONS

1. Conclusions

In this thesis, various 3D fabrication techniques were developed to address the challenges associated with vascular tissue engineering. These challenges include the inability to create 3D artificial tissue constructs with integrated multi-scale high-resolution perfusion channels in natural ECMs and gels, as well as the inability to fabricate hierarchal concentric layers of various cell types, similar to that found in biological vessel architecture. Without the incorporation of functional vascular-like networks into 3D engineered tissues, the cells cannot survive. The incorporation of perfusable hollow networks for nutrient and waste transport allows the creation of functional, sustainable artificial 3D tissue constructs. The techniques developed in this thesis allow the creation of thick multi-layered hydrogel scaffolds with embedded perfusable hollow channel networks as well as the formation distinct concentric layers containing multiple materials and cell types. This is done using simple, fast, and affordable methods.

A low-cost, commercial RepRap printer was used in combination with a custom-made coaxial nozzle in order to fabricate of gel layers with interspaced hollow tubes directly on dry substrates in precise geometries. A wide range of channel diameters (500 μ m – 2mm) were achieved in the multi-layered structures printed using a variety of flow rates and print speeds. Upon completion of printing, constructs maintained their structural integrity and were immediately ready for use. No additional handling was required such as bulk immersion or sacrificial-layer removal. Cell viability was also maintained (81.4 \pm 14% and 70.8 \pm 10.7% on day 1 and 3 respectively) in constructs

printed with HUVEC integration by media perfusion of hollow channels. This work illustrated a fast, simple, one-step method for fabrication of vascular channels with precise control of dimensions and patterning. This provides future researchers with an accessible 3D biofabrication technique that is significantly more affordable than the expensive bioprinters that are currently available.

This custom nozzle is highly scalable, which allowed it to be easily modified in order to achieve multi-axial extrusion. This modification was successfully used to create bi- and tri-layered hollow channel constructs embedded within 3D structures. In this thesis, it was demonstrated that these architectures were easily achievable this low-cost, set up. Multi-layered gel scaffolds were fabricated with embedded hollow channels surrounded by hierarchal gel layers in a simple and effective manner. It was shown that different cell types could be included in each respective layer, thereby facilitating a method for multi-cellular construct fabrication. Not only did this versatile approach allow for the incorporation of co-culture systems within a single structure, it also provided the ability to fabricate multi-material constructs by simultaneous printing of several soft materials with various mechanical properties. In doing so, the scaffolds' structural integrity and stability was preserved without compromising the necessary cell-friendly environment required to maintain cell viabilities. With this device design, heterogeneous, hierarchal structures were created with complex architectures using various biocompatible materials or different cell types within a single scaffolding structure. Increased control in the creation of these organized 3D biological structures brings the field one step closer to building large, full-scale functional tissues and organs.

In addition to the extrusion-based techniques, new lamination-based planar processing methods were also established in this thesis in order to create hollow channel constructs with significantly high feature resolutions. The use of this planar processing for tissue engineering application is contingent on the availability of an effective, inert and biocompatible adhesive. This work presents silicon carbide (SiC) nanoparticle solution as one such adhesive that is capable of bonding collagen-containing gel layers intimately, with substantial adhesive strength even at very low concentrations. This is the first demonstration of the use of SiC as a bioadhesive material. A composite material was developed, containing both alginate as a structural material and collagen as an extracellular

matrix for cell growth that is suitable for tissue engineering purposes. This composite provided the structural strength to fabricate complex microchannel features through simple casting based approaches. Using the combination of the composite gels, SiC adhesive solution and layer by layer fabrication, fabrication of thick (8mm) gel layers was achieved with integrated microchannels that can serve as perfusion networks. Channels as small as 150 μ m and spaced as close as 500 μ m were successfully created. Cells seeded in these constructs that are perfused showed good viability. This method creates gel scaffolds that are instantly perfusable. Furthermore, this casting approach allows for conservative use of cells and gels that may be expensive and valuable. This approach is also scalable and easy to use and is expected to find a wide variety of applications in tissue engineering. The ability to fabricate 3D artificial tissue constructs with integrated vascular-like networks is also of significant potential to be used in applications other than tissue replacement, such as drug discovery models and biological studies.

2. Research Contributions

2.1 Low-cost 3D bioprinting

i. Most available bioprinting systems are expensive and generally cost upwards of \$10K. In this work, a bioprinting system is developed simply using a low-cost 3D printer (\$600) that was modified to include a co-axial PDMS nozzle. PDMS is also a low-cost, readily available material and the needles used within the nozzle are commercial, meaning this device and entire system are easily attainable and affordable. This system is accessible for other researchers interested in implementing this method.

ii. Many researchers had previously explored gel fiber deposition in a bath for use as vascular scaffolds. However, those techniques do not allow patterning of these structures and therefore cannot create multi-layered 3D constructs with integrated perfusion channels. In this work, an interesting phenomenon was developed for simple, one-step

fabrication of solid 3D gel constructs with integrated hollow channel structures. Upon deposition, the inner side of the annular gel layer was crosslinked while the uncrosslinked gel on the outside spread laterally resulting in fusion between one parallel tube to the next thereby forming a continuous solid gel layer with embedded, hollow channels. Since the individual channels were extruded in a continuous fashion they were connected at the ends, which made perfusion of the entire 3D gel layer straightforward. Multi-layer hydrogel structures were also created in this way with a connection from channels in one layer to the next, provided that printing is continuous.

iii. With current 3D fabrication techniques for vascular tissue engineering, there exists a lack of characterization for determining the operational range suitable for producing constructs of varying sizes. In this work, it was found that printing accuracy was dependant on both flow rate and printhead motor speed, which caused limitations in the operational range. These factors were characterized and a map of the operational range was established. In this way, tubes of varying inner diameters were simultaneously printed within a single gel structure. Therefore, future operators or researchers can use this predetermined mapping of the operational range in order to create specific construct dimensions.

2.2 Multi-biomaterial printing

i. A major trait of vascular tissues is the hierarchal architecture. Most of the currently available approaches are only able to achieve this using manual coating techniques. This thesis demonstrated an alternative automated approach for creating hollow channel structures with concentric gel layers that are composed of distinctly different cell types of biomaterials. This was done using a fast and effective extrusion-based technique as opposed to the tedious and laborious methods that have been previously used.

ii. Most available strategies can only achieve bi-layer structure fabrication. In this work, a highly scalable multi-axial extrusion nozzle is used that can theoretically allow for any number of concentric layers to be created. Tri-layer construct fabrication was successfully demonstrated. Additionally, this nozzle allows for active control of concentric gel layer thickness, unlike currently available techniques. This was done by altering flow rates or printspeeds.

iii. Previous techniques have demonstrated difficulties in creating structures that are both structurally sound as well as promote cell adhesion. This is due to trade-offs that exist between using material cytocompatibility and mechanical properties. With this multi-axial extrusion nozzle, various biomaterials can be printed simultaneously in a single structure, thereby maintaining structural stability and integrity without compromising cell adhesion and growth.

iv. A full characterization of factors affecting printability was performed. These factors included flow rates, printspeeds, and material concentrations. This allowed the operational printing range and its boundaries to be successfully mapped.

2.2 Nanoparticle-based hydrogel adhesion

i. A common challenge for planar processing techniques is the availability of appropriate laminates. In this thesis and for the first time, silicon carbide (SiC) nanoparticle solution is demonstrated as an effective adhesive for achieving strong bonding between biologically relevant hydrogel layers such as collagen. This discovery allowed the fabrication of stacked, multi-layered 3D constructs with integrated multi-scale perfusable networks using a lamination based planar processing technique.

ii. Previous techniques used for 3D vascular tissue engineering have generally achieved hollow feature resolutions of 250 μ m – 1mm. In this work, significantly higher

feature resolutions of 150 μ m were fabricated. The SiC nanoparticles did not cause any blockage or obstruction of the intricate hollow channels.

iii. Nanosilica solutions have previously been demonstrated as strong, viable adhesives for biological tissue bonding. This thesis presents a thorough comparison between nanosilica and SiC as biological adhesives. It was found that SiC bond strengths were equivalent to nanosilica. However, nanosilica was found to have adverse effects on cell viability and caused channel blockage at higher resolutions, while SiC demonstrated good cytocompatibility and did not block channels.

iv. Although nanosilica was found to be unsuitable as an inter-layer adhesive, a new and alternative use was established. Nanosilica was found to enable attachment of the soft gel constructs to hard substrates (i.e. glass or PVC tubing), thereby creating single inlet and outlet junctions for easy and straightforward perfusion of the entire 3D construct.

3. Recommendations for Future Work

3.1 “All-in-one” bioprinter for multi-biomaterial extrusion

As previously discussed, current commercially available bioprinters are expensive. The 3D printing setup described in this thesis is low-cost, however it requires the use of several individually controlled syringe pumps in order to achieve multimaterial extrusion. Using some simple additional modifications, this use of multiple syringe pumps can be eliminated. The current setup can be further modified in order to create a central, automated pumping station that is controlled via a single, common software. To do so, additional stepper motors that are recognized by the control board can be integrated and used to facilitate extrusion of various biomaterials. Therefore, a commercially competitive “all-in-one” 3D bioprinting station can be realized in under \$1000. This method also demonstrates its potential to build a 3D-printing database for other tissue engineering applications. A user may select a specific set of variables from a variety of

available options (e.g. type of biopolymer, material concentration, cell type or density) and be able to easily create the required 3D construct under pre-set limitations.

3.2 Inducing angiogenesis

Inducing angiogenesis sprouting from the fabricated hollow channels in the 3D engineered constructs will increase the constructs permeability to perfused nutrients. Future work would be focused on the use of gels containing fibrin, which is known to induce angiogenesis. Tissue engineered vascular networks can also be further supported using multi-cellular systems, specifically with fibroblasts and mesenchymal stem cells (MSCs). Fibroblasts are often included in endothelial coculture systems due to their production of VEGF and subsequent angiogenic tendencies. MSCs are an attractive stem cell source for tissue regeneration applications because they are characterized as undifferentiated, self-renewing cells with a high proliferative capacity. Therefore, a tri-cellular culture system including HUVECs, fibroblasts, and MSCs would be ideal for inducing angiogenesis in a fibrin-based scaffold. This would additionally aid in creating a more realistic and functional tissue microenvironment that is useful in drug discovery applications as is discussed in the next section.

3.3. Drug discovery models

Currently used 2D culture models are not ideal for simulation of true 3D biological environments. The 3D fabrication techniques presented in this work for Human tissue architecture integrated with vascular networks can provide a platform for the study of a realistic model for drug discovery and biological studies. For example, this can be used for modeling varying aspects of tumorigenesis such as metastasis, drug resistance, and intercellular communication. The effect of fluid flow on cancer progression is currently not well understood and requires further research. Therefore, these perfusable tumor models could be used to study how tumor migration, growth, and

invasion are affected by fluid flow and the role of vascular barrier function. It is necessary to be able to observe the cell-cell interactions occurring in a 3D environment, which is critical in mimicking organ-level physiology, function or diseases.

3.4 Alternative tissue engineering applications

This work has the potential to be extended for a variety of tissue engineering applications involving tubular scaffolds such as nerve conduits or skeletal tissue engineering. For example, these hollow structures can be used to deliver a growth factor gradient that would control and promote axon generation in applications involving neuronal tissue replacement. This can potential be used in spinal cord injury cases where controlled axon generation is necessary for repair at the site of injury. These channels may also be utilized to alignment and orientation of muscle cells such as myoblasts in order to guide engineered muscle-like fibres and tissue architecture. Replicating these types of multi-scale, organized arrangements is crucial to building large pieces of functional tissue.

APPENDIX

1. Hollow Channel Fabrication

A) Sample code for 3D extrusion printing:

G21 ; set units to millimeters

M107 ; fan off

G28 X0

G28 Y0

G28 Z0; home x and y axis

G90 ; use absolute coordinates

G92 ; set position

G1 F2000.000 ; move to starting position at 2m/min

G92

G1 X54 Y70 F10000

G1 X54 Y150

G1 X57 Y150

G1 X57 Y50

G1 X60 Y50

G1 X60 Y150

G1 X63 Y150

G1 X63 Y50

G1 X66 Y50

G1 X66 Y150

G1 X69 Y150

G1 X69 Y50

G1 X72 Y50

G1 X72 Y150

G1 X75 Y150

G1 X75 Y50

G1 X78 Y50

G1 X78 Y150

G1 X81 Y150

G1 X81 Y50

G1 X84 Y50

G1 X84 Y150

G1 X87 Y150

G1 X87 Y50

G1 X90 Y50

G1 X90 Y150

G1 X110 Y150

G92

M84 ; disable motors

B) 3D printed mold for nozzles and planar processing:

1. 3D mold design is created using Inventor software and converted into STL file format.
2. 3D printer is used to print the STL file (Project HD 3000, 3D Systems) using plastic (VisiJet EX200).

C) PDMS casting for microfluidic nozzle:

1. PDMS is stirred in a 10:1 ration of base to curing reagent respectively (Sylgard 184, Dow Corning) and then poured onto the mold.
2. Mold is placed into a desiccator and degassed for 10minutes in order to remove bubbles.
3. PDMS-filled mold is placed onto a hot plate or oven at 80°C for 2hours until PDMS is cured
4. Cast PDMS is removed by cutting around the edges of the mold and carefully peeling in order to remove.

D) Hydrogel casting for planar processing:

1. Collagen dissolved in 0.2N acetic acid is pre-crosslinked by adding 0.1N sodium hydroxide and gently pipetting up and down in order to mix without causing bubbles.
2. Immediately after mixing, collagen is mixed with alginate solution in order to create a composite solution before collagen completes gelation (~30min).
3. Small pieces of filter paper (Whatman's) are soaked in calcium chloride solution.
4. The hybrid hydrogel mixture is pipetted onto the mold and crosslinked by gently placing the calcium-soaked filter paper gently on top in order to achieve a flat film. Additional calcium chloride solution in order to complete gelation.
5. The film is left to sit for 2 hours in order to ensure that gelation is complete, and then gently peeled from the mold.

2. Hollow Channel Imaging

A) Fluorescent imaging:

1. Samples are stained with calcein acetoxymethylester (calcein AM) (Life Technologies) added to EBM at a concentration of 0.5%v/v.
2. Samples are incubated for 30 minutes in the staining media. After incubation, the media is aspirated and the samples are washed twice with Dulbecco's phosphate buffered saline (DPBS) (Life Technologies) before imaging.
3. Confocal microscope (LSM510, Zeiss) image montages were automatically generated by microscope control software during image acquisition (ZEN, Zeiss). Detection gain, amplitude offset and laser intensity are kept constant within the imaging database in order to normalize fluorescence and allow equivalency between image comparisons.
4. Z-stack sample projections are formed using image slices taken along the Z-axis from the bottom of the sample to the surface at intervals of 10um or 20um.

B) Cross-sectional imaging:

1. Samples are fixed with glutaraldehyde (2% v/v) in 0.1M sodium cacodylate buffer pH 7.4 then rinsed twice in buffer solution, and then post-fixed in 1% osmium tetroxide in 0.1M sodium cacodylate buffer for 1 hour.
2. Samples are dehydrated through a graded ethanol series (50%, 70%, 70%, 95%, 95%, 100%, 100%). Infiltration with Spurr's resin was gradual (2:1 ethanol:resin, 1:1 ethanol:resin, 1:2 ethanol:resin, 100% resin, 100% resin, 100% resin).
3. Samples are transferred to embedding molds, which were then filled with fresh 100% Spurr's resin and polymerized overnight in a 60°C oven.
4. To obtain hollow channel cross-sections, 1um sections were cut using Leica UCT Ultramicrotome and stained with Toluidine Blue. Sections were dried on glass slides.
5. To obtain embedded cell images, thin sections (100nm) were cut on Ultramicrotome and post-stained with uranyl acetate and lead citrate, then viewed in a JEOL JEM 1200 EX TEMSCAN transmission electron microscope (JEOL, Peabody, MA, USA) operating at an accelerating voltage of 80kV. The images were acquired with an AMT 4 megapixel digital camera (Advanced Microscopy Techniques, Woburn, MA).